Trochoidal Milling

by

Murat Ötkür

A Thesis Submitted to the
Graduate School of Engineering
in Partial Fulfillment of the Requirements for
the Degree of

Master of Science
in
Mechanical Engineering

Koc University

October 2006

Koc University

Graduate School of Sciences and Engineering

This is to certify that I have examined this copy of a master's thesis by

Murat Ötkür

and have found that it is complete and satisfactory in all respects,
and that any and all revisions required by the final
examining committee have been made.

Committee Members:

İsmail Lazoğlu, Ph. D. (Advisor)

Murat Sözer, Ph. D.

Fethi Okyar, Ph. D.

Date: 20 / 10 / 2006

ABSTRACT

As more attention is attracted to the quality and productivity in manufacturing, innovative strategies such as modifying toolpaths or applying feedrate scheduling have been alternates to the conventional machining methods. In this thesis an approach to the modeling of trochoidal milling, a widely used application in hard part machining, is proposed. In trochoidal milling the cutter traces a trochoidal toolpath and the radial depth of cut always varies along the toolpath. An analytical model for the engagement of simple surface machining is derived. Moreover, a numerical model is developed for defining the engagement for complex surfaces containing hole or bosses on it. Lastly a force model employing the engagement results is carried on for prediction of the cutting forces. In order to maximize the efficiency in the trochoidal milling operation, different toolpath strategies are examined where the back half part of the planetary revolution motion is shortened with a linear motion or completely eliminated with double trochoidal milling. Moreover, a forced based feedrate scheduling strategy is applied for double trochoidal milling for further maximization of machining efficiency. Physical experiments are performed in a three axis vertical machining center and the predicted forces are compared to the measured forces in three orthogonal directions. It is observed that the predicted forces and the measured forces are in good agreement in all the applications of the thesis. Finally an experimental study investigating the wear comparison of trochoidal and linear milling with cutting forces and surface roughness aspects is performed.

ACKNOWLEGMENTS

I would like to express my sincere gratitude and appreciation to my advisor, Dr. İsmail Lazoğlu for his expert guidance and mentorship and I would also like to thank Dr. Murat Sözer and Dr. Fethi Okyar for reading this thesis and offering constructive criticism.

I am very grateful to Kübra Kosali, for her love, support and patience during this period.

I would also like to thank all of my friends in the office, Cenk Dinç, Emre Dikmen, Emrah Ahi and Ali Alagöz, Onur Demir and Mehmet Emre Sargın.

And finally, I would like to thank to my sister Banu Ötkür, especially to my mother Olcay Türkan Ötkür and my father İsmail Ünal Ötkür for their life-long love, for the kind of encouragement and support they have provided me throughout my entire education life, and for their absolute confidence in me.

TABLE OF CONTENTS

LIST OF TABLES

LIST OF FIGURES

NOMENCLATURE

a	Axial depth of cut
A_s	Shear plane area
b	Chip width
b_1, b_2	Dimensions of the workpiece
c	Stepover between the planetary revolutions
D	Diameter of the cutter
dA_c	Differential chip load
dF_t, dF_r, dF_z	Differential cutting forces in tangential, radial and axial directions
dF_x, dF_y, dF_z	Differential cutting forces in x, y, and z directions
dz	Height of axial disc elements
$d\phi$	Discrete cutting element rotation angle
F_f	Feed direction cutting force in turning
$F_{lim,i}$	Limiting constant resultant force threshold value
F_t, F_r, F_a	Cutting forces in tangential, radial and axial directions in milling
F_s	Shearing force
F_t	Tangential direction cutting force in turning
F_x, F_y, F_z	Cutting forces in x, y and z directions in milling
$\bar{F}_x, \bar{F}_y, \bar{F}_z$	Average milling forces per tooth period in X, Y, Z directions
$\bar{F}_{xc}, \bar{F}_{yc}, \bar{F}_{zc}$	Average milling edge forces per tooth period in X, Y, Z directions
$\bar{F}_{xe}, \bar{F}_{ye}, \bar{F}_{ze}$	Average milling cutting forces per tooth period in X, Y, Z directions
F_1	Maximum resultant force value for the f_1 feedrate value
F_2	Maximum resultant force value for the f_2 feedrate value
f	Feedrate of the cutter in mm per minute

$f_{lim,i}$	Scheduled feedrate value in mm/min for the i^{th} CL point
f_s	Data sampling frequency
f_1	Original constant feedrate for the toolpath in mm/min
f_2	Twice of f_1 feedrate in mm/min
h	Uncut chip thickness
h_c	Cut chip thickness
j	Tooth number in the cut
K_t	Tangential cutting force coefficient
K_{tc}, K_{rc}, K_{ac}	Tangential, radial and axial cutting force coefficients in milling
K_{te}, K_{re}, K_{ae}	Tangential, radial and axial edge force coefficients in milling
K_r	Radial cutting force ratio
L_{entc}	Length of the line segment $\|P_{ent}\ P_c\|$
L_{extc}	Length of the line segment $\|P_{ext}\ P_c\|$
L_{1c}	Length of the line segment $\|P_1\ P_c\|$
L_{1ent}	Length of the line segment $\|P_1\ P_{ent}\|$
L_{1ext}	Length of the line segment $\|P_1\ P_{ext}\|$
L_{12}	Length of the line segment $\|P_1\ P_2\|$
L_{2c}	Length of the line segment $\|P_2\ P_c\|$
N	Number of flutes in the cutter
n	Spindle speed in revolution per minute
$P_c\ (X_c, Y_c)$	Position of the cutter center
$P_{c0}\ (X_{c0}, Y_{c0})$	Position of the planetary revolutions center
$P_1\ (X_1, Y_1)$	Position of the farthest point on the cutter periphery from the planetary revolutions center
$P_2\ (X_2, Y_2)$	Position of the point with the lowest y coordinate on the periphery of the cutter intersecting with the previously machined surface

P_{en}, P_{ex}	Position of the points on the previously machined geometry with the minimum distance value in feed direction
P_{ent}, P_{ext}	Position of the entrance and exit points
R_c	Radius of the cutter
r_c	Chip compression ratio
R_p	Radius of the planetary revolutions
t_c	Instantaneous chip thickness
t_x	Feed per tooth per revolution
X, Y, Z	Global coordinate system for the cutting process
z	Axial positions of the disc elements of the cutter
α_r	Rake angle of the tool
β	Helix angle of the cutter
β_a	Friction angle
ϕ	Angular position of the cutting tooth in the cut
ϕ_p	Cutter pitch angle
ϕ_{st} , ϕ_{ex}	Start and exit angles for the immersion
θ	Angle defining position of the cutter
θ_{en}, θ_{ex}	Angle defining the points P_{en}, P_{ex}
φ	Shear angle
τ_s	Shearing stress
ψ	Lag angle

Chapter 1

INTRODUCTION

With in the days of the beginning of the new millennium, all types of productions are getting more complicated and automated. The fundamental requirement for the competitive behavior of the production world is mainly due to reduction of the life cycle times of the goods exposed in the world marketing. Considering the electronics and automotive industry, the life cycle times of many products such as cars and electronic devices have decreased two to three folds in the last decade [1]. As the world marketing competition gets harder and harder, the manufacturers are obliged to update their products much faster. As a result this situation creates the demand for the automation and the increase in the efficiency of the production systems for the die and mold making industry.

Among all the other production techniques, metal machining is probably the most used one for the die and mold industry [2]. It has various advantages and disadvantages compared with other techniques used in the industry such as electrical discharge machining (EDM), forming and casting. First of all metal machining is applicable to all cutting materials and provides a more accurate surface, reducing and completely eliminating the additional cost and times for finishing operations. Unlike EDM or casting operations, the machining tool is not unique for the application; it is a simple and standard product. On the other hand metal machining is not suitable for quantity production, and the final part geometry is limited with depth and radius.

The metal cutting technology can be classified into many subdivisions according to the geometry of cutting tool, workpiece and their relative motion towards each other such

as turning, drilling, milling, boring, broaching and grinding. The metal cutting operation is formed between the clamped material on the machine tool and the cutting tool. By removing the excessive material from the blank, the final geometry of the part is achieved. Computer numerically controlled (CNC) machine tools allow the production of complex geometries with the help of the computer-aided design / computer-aided manufacturing (CAD/CAM) systems. The metal machining technology continues to advance in parallel with the developments in the machine tools, programs, materials and cutters. Several researches are trying their bests to achieve more rigid, accurate and automated machine tools.

The machining of hardened steel is becoming widespread throughout the machining world. The hardened materials are more durable against wear and load but on the contrast machining of hardened materials is much more difficult. One alternate for achieving hard final parts is to harden the materials after the final geometry is achieved, but the loss of accuracy due to the expansion of the materials is a major problem. Even the heat treated materials should be hard machining in order to achieve the final part accuracy. Therefore machining of hardened materials is an inevitable process which should be carefully issued and performed. High speed machining (HSM) is a solution to the machining of hardened metals especially taking into consideration the milling operation.

The milling operation is an intermittent cutting process using a cutter mounted on the rotating spindle turning around its axis and a workpiece material fixed on the table of the machine tool moving toward the cutter. HSM is a new approach in which instead of conventional milling process with slow and heavy cuts, a new process consisting of more lighter and faster cuts is used. The chips produced are much smaller but considering the total volume machined the process is highly efficient.

The primary reason HSM works is that less heat is generated. A smaller axial and radial of cut is the main way to generate less heat in the cut. With the cutting edge spending

less time “in the cut” per revolution of the tool, there is less heat generated in the cut, and the spindle speed can be increased. With keeping the chip load per tooth the same, or even increase it slightly, a much higher feed rate can be achieved parallel with the increased spindle speed.

In this study an approach to the modeling of trochoidal milling, a widely used application in hard part machining, is proposed. Trochoidal toolpath is embedded in many CAM programs and strongly advised for hard milling applications. In trochoidal milling, the cutter traces a trochoidal path along the end milling operation and the radial depth of cut is limited and always varies along the toolpath. It helps cooling of the cutter teeth as they spend less time in cutting and have much time to cool.

Chapter 2 contains the necessary background and literature review on end milling operation. The fundamentals of metal cutting analysis, cutting mechanics and previous models for prediction of cutting forces in end milling are reviewed. Moreover, the literature concerning applying different toolpath strategies in order to increase the machining efficiency is analyzed.

In chapter 3 mechanistic cutting force model is represented. The mechanistic cutting force model consists of end milling cutting force model and engagement defining algorithms. Two engagement defining algorithms was developed for trochoidal milling: An analytic model for filled surfaces and a numerical one capable of defining the engagement for complex surfaces containing hole or bosses on it.

Calibration process details are given in chapter 4, where the methodology that is employed to determine the cutting constants for the force model is described. In addition to that an experimental study on influence of radial depth of cut in mechanistic identification of milling constants is carried.

Chapter 5 presents the modification algorithms for trochoidal milling method. Different toolpath strategies such as trochoidal toolpath with straight linear motion at the

back half planetary revolution and double trochoidal milling mechanisms are investigated. Moreover force based feedrate scheduling algorithm with NURBS is introduced to trochoidal milling method.

Validation tests under various conditions are described and their results are given in chapter 6. Validation tests include simple trochoidal milling of filled surfaces and complex trochoidal milling of a cover of a cylinder head block of a diesel engine. Moreover, modified trochoidal milling toolpaths and force based feedrate scheduling applied trochoidal milling validation tests are performed.

Chapter 7 presents an experimental study investigating the comparison of trochoidal milling with linear milling methods from wear, force and surface roughness aspects. Two set of experiments (linear and trochoidal) are carried with two different cutter and workpiece material pairs. Tool wear on rake and clearance surfaces, force profiles and surface roughness values are experimentally measured between the samples of the milling periods and analyzed.

The thesis is concluded with a short summary of the performed study and the future research.

Chapter 2

LITERATURE REVIEW

2.1 Introduction

Metal cutting process has wide application areas in production industry. Among the several machining operations, milling has taken an important role as it is an excessively used process in the automotive, aerospace, die and mold industries. End milling is a special and rather simple case of milling operation employing a helical end mill for slot milling, edge milling and face milling operations. End milling is probably the most used type of milling processes as it is capable of both rough and finish machining thus allowing the engineers to produce the final part from the bulk material. The process is a versatile one and has many application areas such as very simple face milling of flat surfaces or complex machining of 3D free from surfaces.

A review of the literature pertaining to trochoidal milling can be divided into two sections, cutting force model development of end milling process and applying different toolpath strategies in order to increase the machining efficiency.

2.2 Cutting Force Model

One of the most important parameters that affect the machining quality is the cutting forces excessive of which results in cutter deflection causing shape errors on the machined part or more dramatically breakage of the cutter causing complete failure of the machined part or even the machine tool system. Therefore for the monitoring and optimization of the

machining processes a reliable quantitative and qualitative prediction of the cutting forces is inevitably required.

The force prediction studies rely on early definitive work on the geometry of the milling process by Martellotti [3, 4]. Martellotti stated that the united translational and rotational (around cutter axis) motions of the cutter turns out the fact the true path of the tooth of the milling cutter is trochoidal rather that circular. For light feed per tooth values (compared with the radius of the cutter), in practice the necessary condition is usually satisfied, the tooth path is almost circular and the circular tooth path approximation is valid.

Koenigsberger and Sabberwal developed mechanistic models [5]. These models relied on the experimentally measured forces during cutting tests and they developed an empirical coefficient that relate the instantaneous cutting forces to chip load which is chip thickness times cut length (axial depth of cut in vertical milling, horizontal width of cut in slab milling) (Equation 2.1). After analyzing of the tangential cutting forces the following model is proposed:

$$F_t = K_t.(b.t_c) \tag{2.1}$$

where K_t is the called tangential cutting force coefficient, b is the chip width and t_c undeformed chip thickness. In this approach cutting force coefficient which relates the cutting forces to the chip load was established from experimental milling force tests for a given cutter geometry and tool workpiece material combination using an empirical approach.

Tlusty and MacNeil further developed the model in which in addition to tangential cutting forces radial cutting forces are predicted (Equation 2.2). Tangential cutting forces are the same with the previous model; on the other hand radial cutting forces are the multiplication of tangential cutting force with an empirical constant [6].

$$F_t = K_t.(b.t_c)$$
$$F_r = K_r.F_t \quad (2.2)$$

where F_r is the radial cutting force and K_r is the radial cutting force ratio.

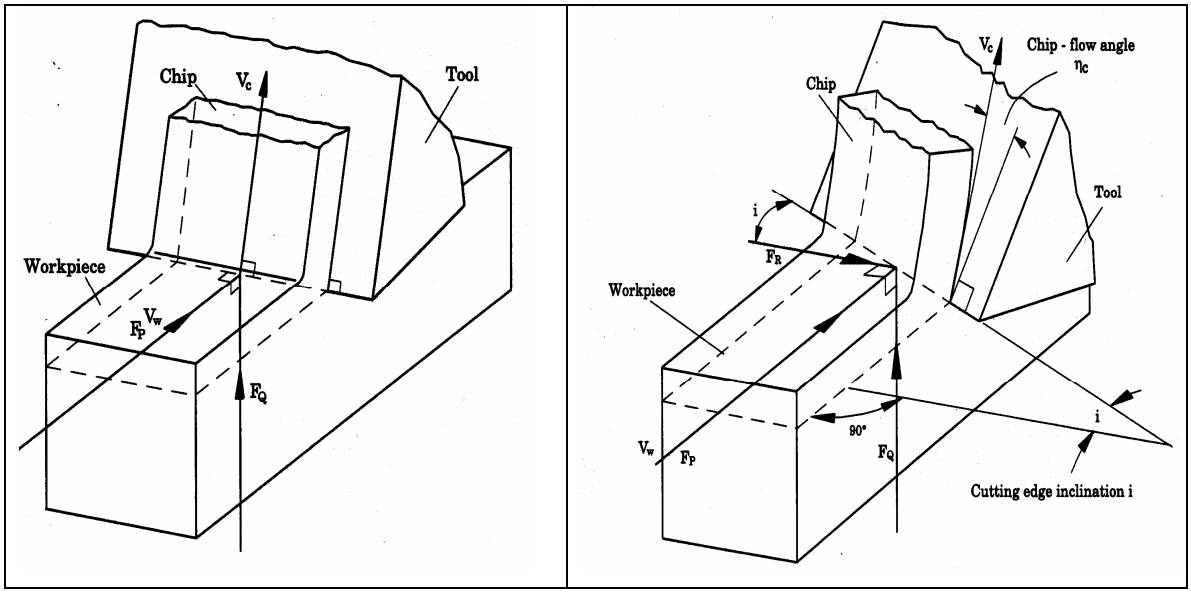

Figure 2.1: Geometries of orthogonal and oblique cutting processes, orthogonal cutting shown on the left, oblique on the right side of the figure [2].

Gygax simulated the cutting forces for multi-tooth face milling from the single tooth model. After determination of the cutting forces in tangential and radial directions the cutting coefficients are calculated by dividing the magnitude of tangential cutting force with the undeformed chip area [7, 8]. Kline et al. presented an improved model containing cutter and workpiece deflection [9, 10] and a model with the capability of handling applications to cornering cuts [11]. Sutherland and DeVor improved Kline's studies by presenting an advanced model for flexible end milling systems which takes into account the effects of system deflections of the chip load and solves the chip load that balances the cutting forces

and resulting system deflections [12]. Montgomery and Altintas presented a method for a comprehensive simulation model for dynamic milling [13]. Armarego and Deshpande et al. developed an improved model in predicting the milling force coefficients for cylindrical helical end mills by introducing an edge force components (Equation 2.3) [14].

$$\begin{aligned} F_t &= \left[K_{tc}\, t_c + K_{te}\right] b \\ F_r &= \left[K_{rc}\, t_c + K_{re}\right] b \end{aligned} \tag{2.3}$$

where K_{tc}, K_{rc}, K_{te} and K_{re} are the tangential and radial cutting force and edge coefficients respectively.

As an alternative to the mechanistic approach, mechanics of milling has been studied to make use of the orthogonal cutting parameters for cutters with well defined geometries. Armarego [14, 15] was among the few researchers to apply the orthogonal to oblique transformations on milling force predictions. The basic idea is to represent the milling geometry by segments of oblique cutting processes. Budak, Altintas and Armarego developed a unified mechanics of cutting approach for prediction of the cutting forces in milling [16]. In this approach milling force coefficients for all cutter geometrical designs can be predicted from orthogonal cutting data base (i.e., shear angle, friction coefficient and shear stress) and the generic oblique cutting analysis for use in the predictive mechanistic milling models. This approach eliminated the need for the experimental calibration of each milling cutter geometry and can be applied to more complex cutter designs thus allowing optimization of the cutter design before manufacturing.

2.3 Applying Different Toolpath Strategies and Efficiency Maximization

The intermittent geometry of milling operation results in varying force profiles along the toolpath for machining complex geometries if the cutter is moved with linear paths.

Varying force profiles not only cause different machining tolerances and accuracies but also lead to loss of efficiency due to long machining times at constant cutter travel speeds. Several researchers have worked on optimization of the milling process including toolpath planning for precision machining [17]. Erdim investigated the influence of different toolpath alternatives on cutting forces and surface errors [18].

Especially for hard material machining avoiding large radial depth of cut which directly increases the cutting temperatures due to lack of time for the cutter teeth to cool is strongly advised [19]. In circular milling method, analyzed by Kardes and Altintas [20], the cutters traces a circular path enabling the slicing of the workpiece gentle by having small engagement conditions. Due to the small engagement domain the cutting forces are restricted therefore the feedrate can be raised in order to increase the machining efficiency. Elger et al. proposed MATHSM: medial axis transform toward high speed machining for pocketing in which the cutter following circular paths with varying diameter [21]. However, in real CAM application the cutter trails a trochoidal path rather than a circular one for the handling of discontinuities [22]. Tang studied on optimization strategy for high speed machining for steel discussing trochoidal toolpath pattern in slot end milling in order to avoid over-heat [23].

Within the new developments in informatics sector, CAD systems have provided tools for defining parametric curves for solid modeling. On the contrary conventional CNC systems could only support motion along straight lines and circular paths. Linear and circular interpolation algorithms are used in conventional CNC machines but they are not adequate enough for achieving the desired precision machining of free-form geometries. Due to the free-form shapes required for aerodynamic, ergonomic or purely aesthetic reasons, the machining of complex shapes needs a better toolpath verification rather than linear segmentation of cutter location points. Therefore Zhang develop and implemented a parametric representation of the toolpath with NURBS curves [24]. Cheng et al. proposed a real-time NURBS motion command generator for CNC machines to achieve the goal of high-speed and high accurate machining [25]. Tsai et al. presents a novel NURBS surface

interpolator that is capable of real-time generation of cutter location (CL) motion command for end milling of NURBS surfaces and maintaining a constant cutter contact velocity along the CL path [26]. Liu et al. developed a comprehensive and generalized parametric interpolator for NURBS curves, with features achieving a uniform feedrate at most of the time, confining chord error under the prescribed tolerance at every point and respecting the machine dynamics in the interpolation stage [27]. In the trajectory planning method a look-ahead module was developed to detect sharp corners on the NURBS curve and feedrate was modified at these corners to meet the chord error requirements and satisfy the machine acceleration and deceleration capacity.

Feedrate scheduling algorithms has attracted great attention for maximization of machining efficiency. Several researchers employed material removal rate (MRR) based feedrate scheduling algorithms depending on volumetric analysis of the material removal rate [28-30]. Ko and Kim et al. presented a NURBS interpolator considering a MRR algorithm [31]. Besides the MRR models, some researchers have performed off-line feedrate scheduling based on the mechanistic cutting force models. Guzel and Lazoglu represented an off-line feedrate scheduling system for sculpture surface machining based on the cutting force model [32]. Erdim, Lazoglu and Ozturk defined an advanced force based feedrate scheduling algorithm capable of 3-D ball end milling of free form surfaces [33].

Although trochoidal milling method is used in many CAD/CAM programs it has not gained enough attention in the academic research studies. Mechanics of similar toolpath patterns such as circular milling has been studied; however mechanics of the trochoidal milling method has never been studied before with the best knowledge of the author. The main motivation in this thesis is to perform a detailed analysis of trochoidal milling with a reliable quantitative force model and a comparison of trochoidal milling with linear milling methods from wear, force and surface roughness aspects.

Chapter 3

MECHANISTIC CUTTING FORCE MODEL

3.1 Introduction

Milling is one of the most important and complex machining processes and is being extensively used in the manufacturing world. It takes place with the rotating cutting tool around its axis and the stationary workpiece material. Raw material is converted into final product by cutting extra material away. Milling operation is an intermittent cutting process using a cutter with one or more teeth and the cutting action of the many teeth around the milling cutter provides a fast method of machining.

Depending on the geometry of the cutting tool and the relative motion of the cutting tool and the workpiece various milling operations are named (Figure 3.1). Each type has specific application areas such as simple face milling of large workpiece materials or advanced ball-end milling for sculptured surfaces.

The performance of machining operations depends on macro (helical-end, ball-end (Figure 3.2), bull-nose, tapered mills, etc.) and micro geometry of the cutting tool (helix, rake, clearance angles), the tool material (cemented carbide, PCD and HSS), the coating tool material (TiN and TiALN), the area of usage (rough, semi-finish and finish milling) and the workpiece material (e.g. steel, Ti, and AL). Macro geometric properties of the cutting tools determine the usage area of them. Due to the intermitted cutting process geometry, periodic loading causes cyclic mechanical and thermal stresses on the tool leading to a shorter tool life. In order to soften the mechanic and thermal load at the entry of the cutter helical end mill are produced with helical flutes (Figure 3.2). The helix on the cutter provides a gradually

increasing chip load along the helical flutes of the end mill. The helical end mill has a constant radius and helix angle along the depth of cut. As opposed to the straight-end mill, the cutting edge geometry of ball-end mill varies locally in the ball part.

Micro geometric properties are explained as follows. A positive rake angle improves the shearing and cutting actions and decreases the forces, however weakens the cutting edge and makes it more susceptible to chipping and breakage. Presence of clearance angle reduces the rubbing on the machine surface thus improves the surface finish. However at, the expense of weakening the cutting edge and more importantly it reduces process damping and increases the likelihood of chatter vibrations.

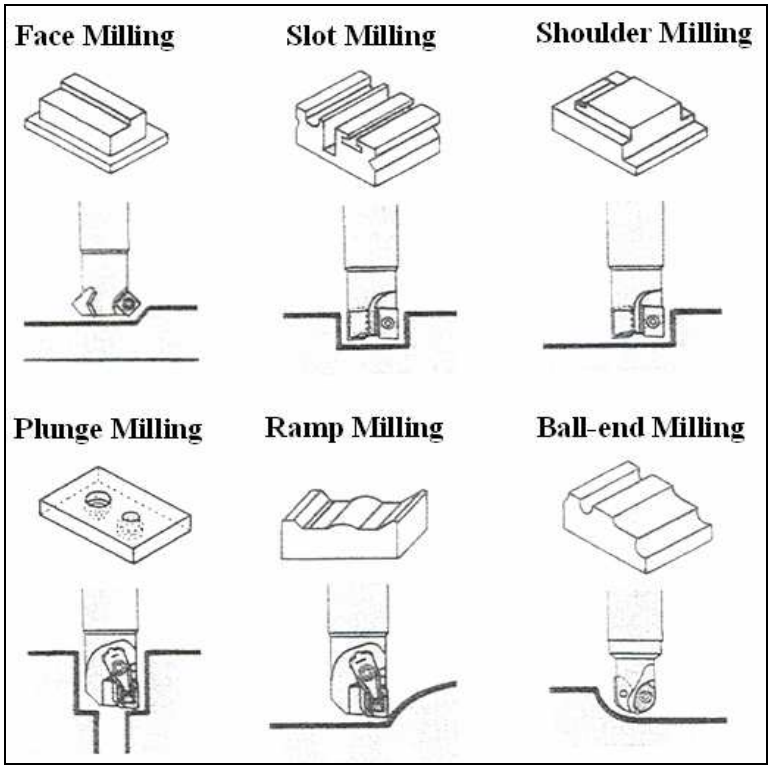

Figure 3.1: Various milling operations from Altintas [2].

The quality of the final product manufactured is directly related to the cutting forces excessive of which result in cutter deflection causing shape errors on the machined part or more dramatically breakage of the cutter causing complete failure of the machined part or even the machine tool system. Therefore for the monitoring and optimization of the machining processes a reliable quantitative and qualitative prediction of the cutting forces is inevitably required. The force prediction algorithm which will be explained in this chapter is adapted from works of Altintas [2] and employs the novel engagement defining algorithms for trochoidal milling situation.

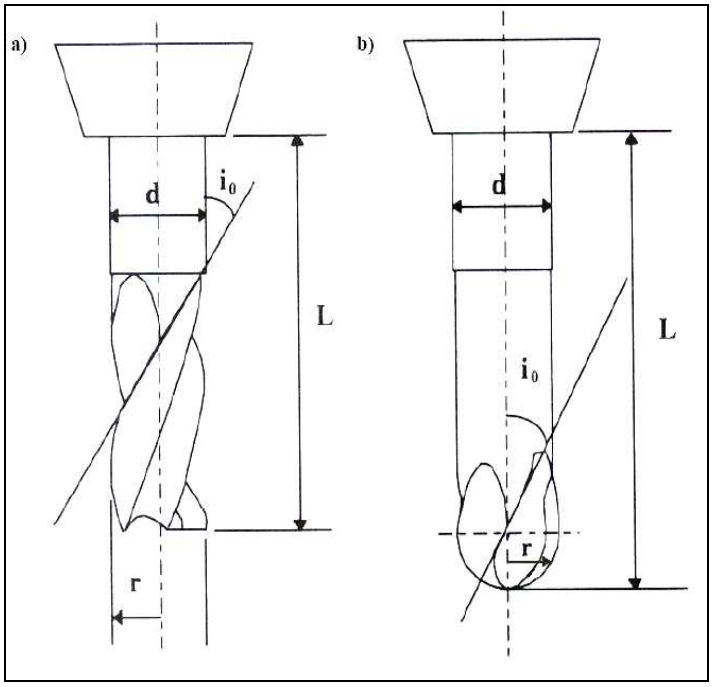

Figure 3.2: Macro geometries of a) End mill, b) Ball end mill from Guzel [34].

In trochoidal milling the cutter traces a trochoidal path along the end milling operation and the engagement conditions always vary along the toolpath. The engagement defining procedures which will be explained in this chapter consist of two different algorithms: An analytical engagement model for simple surfaces and a numerical

engagement model for more complex part geometries. With the numerical model any surface with holes, bosses etc can be handled.

3.2 Mechanistic Cutting Force Model

3.2.1 Introduction

Prior knowledge of cutting forces can assist monitoring and optimization of process taking into consideration the situations: minimizing cutter deflection thus surface errors and eliminating chatter phenomena by selecting the appropriate cutting conditions such as spindle speed, feedrate and depth of cuts. For instance, if the chip load is selected to be too high, the forces cause chipping of the cutting edge or even tool breakage, while a small chip load will decrease productivity.

Due to the importance of cutting forces during milling, research subjected cutting force predictions have been the hottest topic for many year. Among the many milling models a mechanistic approach is preferred since accurate prediction for the cutting forces is aimed.

This section outlines the mechanistic end mill cutting force model used in this thesis. The mechanistic model can be outlined in two main subsections: chip load geometry and cutting force model for helical end mills.

3.2.2 Chip Load Geometry

A significant element in the prediction of the cutting forces is the chip load on the cutter. The chip load for a cutter tooth rotation is the amount of material removed at an infinitesimal time interval. Martellotti presented a detailed early analysis of the geometry of milling process and the chip load calculations used in this thesis is based on this analysis. He stated that the combined translational and rotational (around cutter axis) motions of the cutter

produces a trochoidal path of the milling cutter teeth rather than circular. For light feed per tooth values (compared with the radius of the cutter), in practice the necessary condition is satisfied. The tooth path is almost circular and the circular tooth path approximation is valid. The geometry of end milling and chip formation is shown in Figure 3.3.

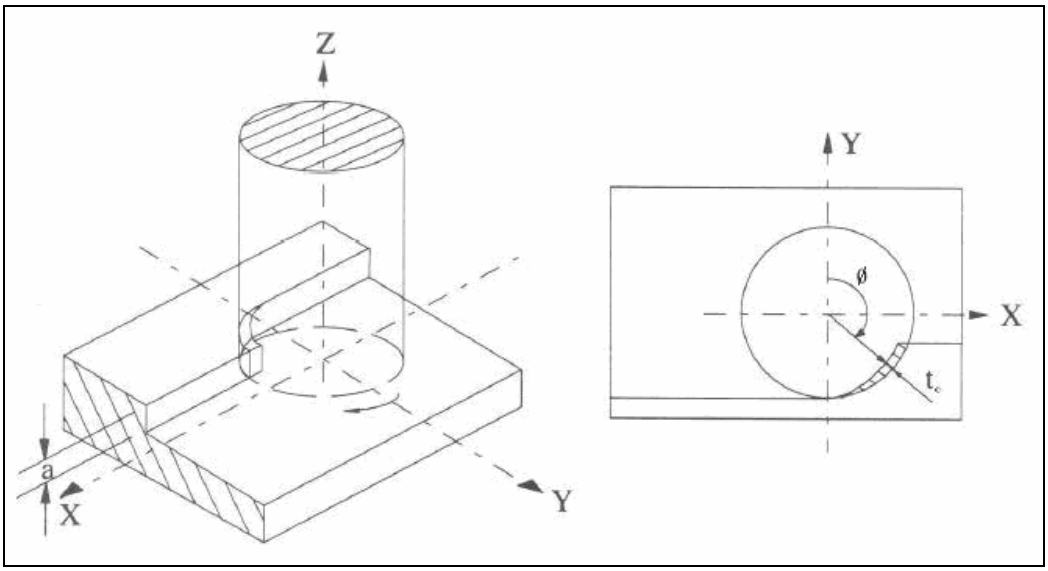

Figure 3.3: End milling geometry and chip formation from Guzel [34].

Chip load is equal to the instantaneous chip thickness times the axial depth of cut (a) in end milling. The instantaneous chip thickness of the cutter tooth for a specific angular position ϕ taking into consideration Martellotti's circular tooth path assumption can be stated as follows:

$$t_c = t_x \cdot \sin(\phi) \tag{3.1}$$

where t_c is the instantaneous chip thickness, t_x is the feed per revolution per tooth and ϕ is the angular position of cutter tooth in the cut.

3.2.3 Cutting Force Model for Helical End Mills

In order to simulate a cutting force model for helical end mills, the helical end mill is divided into several separate discs along the cutter axis (Figure 3.4). The angular position of the first cutter tooth measured clockwise from the cross-feed (y) axis at the lowest axial position is taken as reference angle (ϕ) for the calculations.

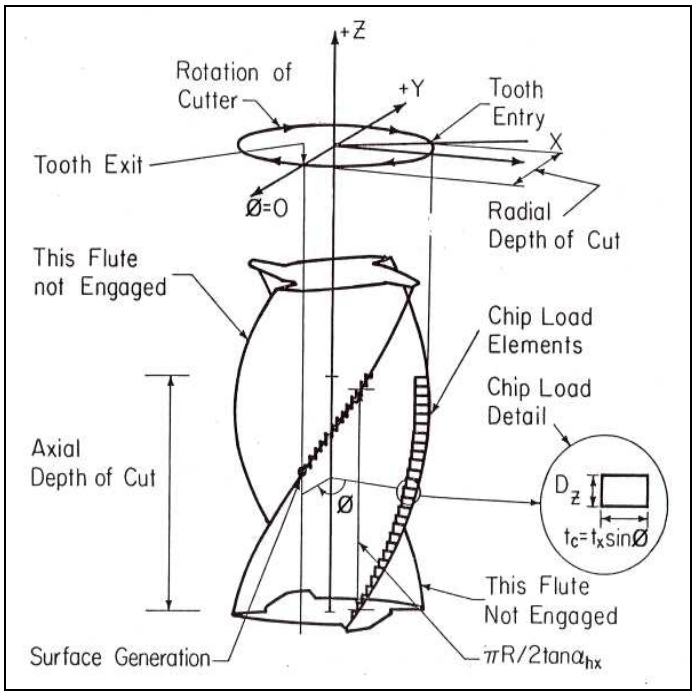

Figure 3.4: End mill with chip load elements from Kline [9].

Due to the helix angle of the cutter, a point on the upper axial disc elements will be lagging behind the reference angle (Figure 3.5). The lag angle (ψ) at the axial position (z) is as bellow:

$$\psi = \frac{2 \,.\, z \,.\, \tan \beta}{D} \tag{3.2}$$

where β is the helix angle and D is the diameter of the cutter. The start and exit angles (ϕ_{st}, ϕ_{ex}) are the angles defining the position of the workpiece. The cutting forces are valid in the presence of the end mill tooth being in the contact zone ($\phi_{st} \leq \phi \leq \phi_{ex}$). If the radial and axial depth of cut large enough, more than one tooth may be cutting simultaneously. The cutter pitch angle is as follows:

$$\phi_p = \frac{2\pi}{N} \tag{3.3}$$

where N is the number of teeth on the cutter. If the bottom end of one cutter tooth is designated as the reference immersion angle (ϕ), the remaining teeth position angles are as follows:

$$\phi_j(z) = \phi + j\phi_p ; \; j = 0, 1, 2, \ldots, (N\text{-}1) \tag{3.4}$$

So the immersion angle for the j^{th} tooth at the axial position (z) is:

$$\phi_j(z) = \phi + j\phi_p - \frac{2 \,.\, z \,.\, \tan\beta}{D} \tag{3.5}$$

For each disc element taking into consideration the lag and pitch angles, the chip thickness ($\phi_j(z)$) is determined and differential cutting forces are calculated. The tangential ($dF_{t,j}$), radial ($dF_{r,j}$) and axial ($dF_{a,j}$) differential cutting forces acting on each axial disc element with the height dz is as follows in the following page:

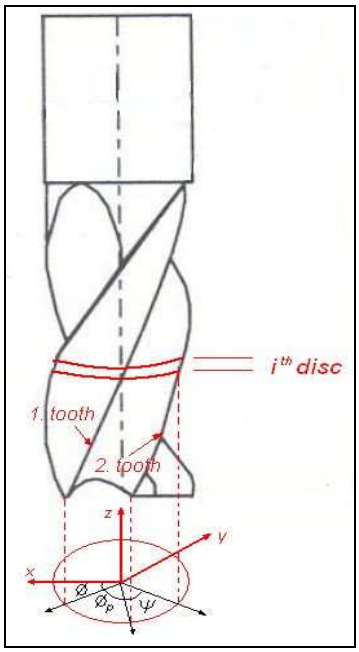

Figure 3.5: End mill with pitch and lag angles.

$$
\begin{aligned}
dF_{t,j}(\phi,z) &= \left[K_{tc}\, t_c\, (\phi_j(z)) + K_{te}\right]dz \\
dF_{r,j}(\phi,z) &= \left[K_{rc}\, t_c\, (\phi_j(z)) + K_{re}\right]dz \\
dF_{a,j}(\phi,z) &= \left[K_{ac}\, t_c\, (\phi_j(z)) + K_{ae}\right]dz
\end{aligned}
\tag{3.6}
$$

where K_{tc}, K_{rc} and K_{ac}, are the cutting force coefficients contributed by the shearing action in tangential, radial and axial directions, respectively, and K_{te}, K_{re} and K_{ae} are the edge coefficients. These coefficients depend upon the cutter workpiece material combination, the cutter geometry such as rake and clearance angles and the cutting conditions such as cutting velocity. In order to evaluate these coefficients calibration tests are performed with constant radial and axial depth of cut and cutting velocity at varying feedrates. Details of the calibration process will be given in Chapter 4.

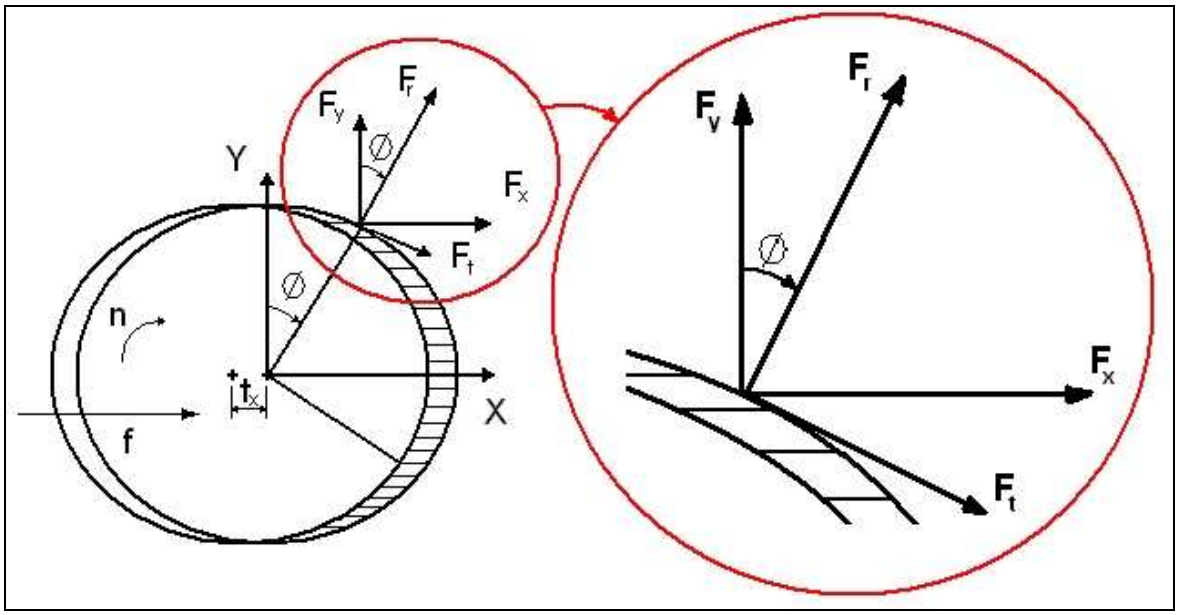

Figure 3.6: End milling differential cutting forces.

The differential tangential, radial and axial direction forces are transformed into feed (x), cross-feed (y) and axial (z) directions using the transformation:

$$\begin{aligned} dF_{x,j}(\phi_j(z)) &= dF_{t,j}\cos\phi_j(z) + dF_{r,j}\sin\phi_j(z) \\ dF_{y,j}(\phi_j(z)) &= -dF_{t,j}\sin\phi_j(z) + dF_{r,j}\cos\phi_j(z) \\ dF_{z,j}(\phi_j(z)) &= dF_{a,j} \end{aligned} \tag{3.7}$$

Integration of the differential cutting forces for each axial height gives the total cutting forces for an angular position of the cutter within the boundary conditions start and exit angles.

$$F_x(\phi) = \sum_{j=1}^{N} dF_{x,j}(\phi_j(z))$$
$$F_y(\phi) = \sum_{j=1}^{N} dF_{y,j}(\phi_j(z)) \quad (3.8)$$
$$F_z(\phi) = \sum_{j=1}^{N} dF_{z,j}(\phi_j(z))$$

In Figure 3.7 the summary of the flow chart for the proposed mechanistic milling approach is represented. The mechanistic cutting force model consists of three basic modules: calibration, engagement defining procedure and force calculation. The cutting force and edge coefficients (K_{tc}, K_{rc}, K_{ac}, K_{te}, K_{re} and K_{ae}) are determined from the calibration process and used as an input for the force model section with engagement region determined from the engagement defining procedure for each cutter location (CL) point. Using the coefficients; tangential, radial and axial direction differential cutting forces are calculated and thereafter these forces are transformed into three orthogonal directions (X, Y, Z). Integration of these forces within the engagement limit conditions results in with the total cutting forces for an instantaneous angular position of the cutter which can be compared with the experiments.

Figure 3.8 represents a pseudocode for end milling force simulation algorithm. Matlab software is employed for the simulation process of the mechanistic cutting force model. The input variables for the simulation algorithm are the cutting parameters such as spindle speed (n), feedrate (f), axial depth of cut (a), start and exit angles for each cutter location point determined from the engagement defining procedure (ϕ_{st}, ϕ_{ex}), cutting coefficients, cutting tool geometric parameters such as diameter (D), helix angle (β) and number of teeth (N) and simulation parameter such as integration angle ($d\phi$) and integration height (dz). The output of the simulation algorithm is the cutting force history for each cutter rotation angle along every cutter location point.

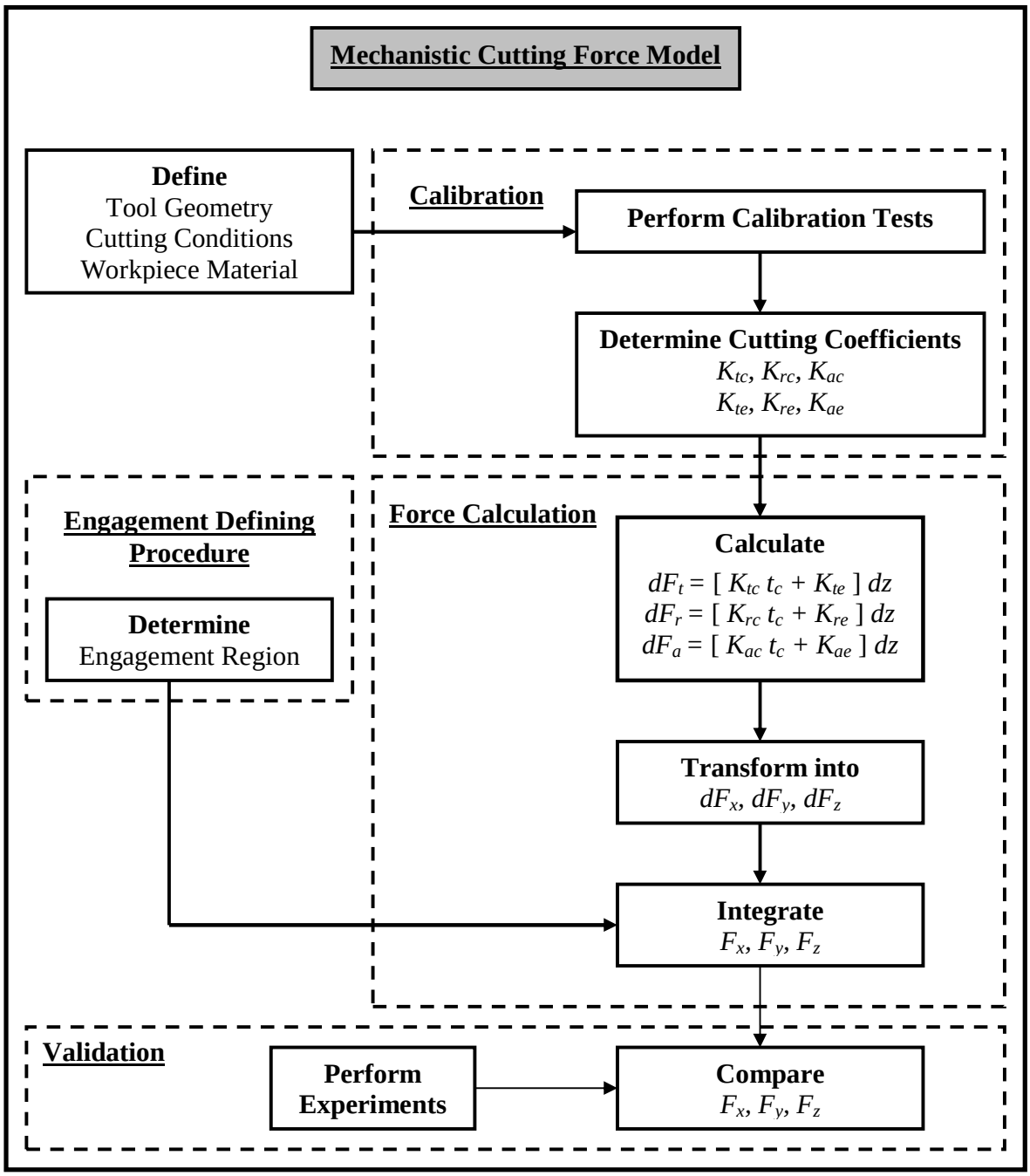

Figure 3.7: A summary flow chart for the proposed mechanistic approach.

Inputs:

Cutting conditions : n (spindle speed), f (feedrate), a (axial depth of cut), $\emptyset_{st}$ & $\emptyset_{ex}$ (start and exit angles)

Tool geometry : D (diameter), β (helix angle), N (number of teeth)

Cutting coefficients : K_{tc}, K_{rc}, K_{ac}, K_{te}, K_{re}, K_{ae},

Integration angle : $d\emptyset$

Integration height : dz

Outputs:

Cutting force history : $F_x(\emptyset)$, $F_y(\emptyset)$, $F_z(\emptyset)$

Variables:

$\phi_p = \frac{2\pi}{N}$: Cutter pitch angle

$K = \frac{2\pi}{d\phi}$: Number of angular integration steps

$L = \frac{D}{2 \cdot dz}$: Number of axial integration steps

i= 1 to K : Angular integration loop

$F_x(i) = F_y(i) = F_z(i) = 0$: Initialize the force integration registers

j=1 to N : Calculate the force contributions of all teeth

k=1 to L : Integrate along the axial depth of cut

$z(k) = k \cdot dz$: Axial position

$\phi_{i,j,k} = i \cdot d\phi + (j-1)\phi_p - \frac{2\tan\beta}{D} z(k)$: Immersion angle of tooth j at the i^{th} angular and k^{th} axial position

if $\emptyset_{st} < \emptyset_{i,j,k} < \emptyset_{ex}$: Force calculation criteria

$t_c = t_x \cdot \sin(\theta_{i,j,k})$: Chip thickness

$dF_t = [K_{tc}\, t_c + K_{te}]dz$

$dF_r = [K_{rc}\, t_c + K_{re}]dz$: Differential forces in tangential, radial, axial directions

$dF_a = [K_{ac}\, t_c + K_{ae}]dz$

$dF_x = dF_t \cos\phi_{i,j,k} + dF_r \sin\phi_{i,j,k}$

$dF_y = -dF_t \sin\phi_{i,j,k} + dF_r \cos\phi_{i,j,k}$: Differential forces in orthogonal directions

$dF_z = dF_a$

$F_x(i) = F_x(i) + dF_x$

$F_y(i) = F_y(i) + dF_y$: Sum the cutting forces

$F_z(i) = F_z(i) + dF_z$

end

end

end

Figure 3.8: Pseudocode for end milling force simulation algorithm.

3.3 Engagement Defining Procedure

In trochoidal milling the cutter traces a trochoidal trajectory thus resulting in extreme variations in engagement conditions. Although mechanics of milling with fixed cutting conditions have been extensively studied in the literature [5-13], there are very few models in the literature published about the mechanics of such processes. Kardes and Altintas investigated the mechanics of circular milling method [20]. However in real CAM applications trochoidal milling is used instead of circular milling method and the modeling of the mechanics of the trochoidal milling method has never been the concern of study before with the best knowledge of the author. The engagement defining procedure has significant importance in the force prediction algorithm as it supplies the boundary conditions for the integration process of the cutting forces. The main intention in employing such a procedure is the determination of angular portion of the cutter which is engaged with the workpiece for a specific cutter location.

The engagement defining procedure proposed in this section consists of two approaches. The first one is the analytical engagement defining procedure which defines the engagement angles for simple trochoidal milling operation with filled surface. The second approach is the numerical engagement defining algorithm capable of defining the engagement for complex surface containing holes or bosses in it.

3.3.1 Analytical Engagement Defining Algorithm

The toolpath of the cutter along the machining operation is shown in Figure 3.9 indicating the necessary parameters. The parameters used in the analytical engagement model are as follows:

R_p: Radius of the planetary revolution,

R_c: Radius of the cutter,

c: stepover value between each planetary revolution,

θ: Angle defining the position of the cutter

b_1, b_2: Dimensions of the workpiece which are defined as the vertical distance from the center of the planetary motion to the upper and lower part of the workpiece respectively.

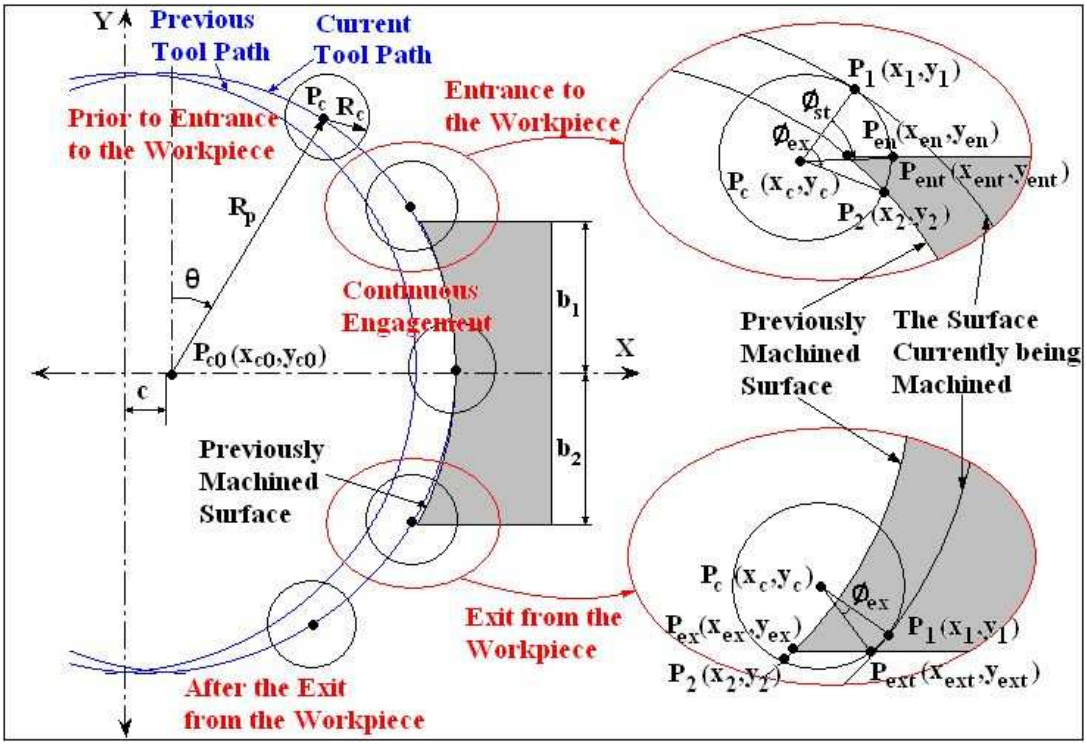

Figure 3.9: Cutter locations for two adjacent planetary revolutions.

The cutter traces a trochoidal path and the location of the cutter center (point P_c) is determined with the parametric equations:

$$x_c = R_p \sin\theta + (c\theta)/2\pi$$
$$y_c = R_p \cos\theta \qquad (3.9)$$

In the current planetary revolution, the periphery equation of the cutter is:

$$(x - x_c)^2 + (y - y_c)^2 = R_c^{\,2} \tag{3.10}$$

where x_c and y_c are determined from Equation 3.9. The equation of the workpiece geometry produced by the previous planetary revolution point P_1 is defined parametrically as follows:

$$\left.\begin{aligned} x_1 &= (R_p + R_c)\sin\theta + \frac{c\theta}{2\pi}, \\ y_1 &= (R_p + R_c)\cos\theta, \\ \left(x_1 - \frac{c\theta}{2\pi}\right)^2 &+ y_1^{\,2} = (R_p + R_c)^2 \end{aligned}\right\} \tag{3.11}$$

It should be noted that the points P_c, P_1 are valid for both previous and the current planetary revolutions with a 2π increment in θ angle for the current one. The points P_{en} and P_{ex} are defined as the points on the previously machined geometry with the minimum value in feed direction at the upper and lower parts of the workpiece respectively. Using the Equation 3.11, plugging $y_{en} = b_1$ and $y_{ex} = -b_2$ the x coordinates of the points P_{en} and P_{ex} are found.

$$\left.\begin{aligned} y_{en} &= b_1 = (R_p + R_c)\cos\theta_{en}, \\ \theta_{en} &= \arccos\left(\frac{b_1}{R_p + R_c}\right) \end{aligned}\right\} \tag{3.12}$$

$$x_{en} = \sqrt{(R_p + R_c)^2 - b_1^{\,2}} + \frac{c\arccos\left(\dfrac{b_1}{R_p + R_c}\right)}{2\pi} \tag{3.13}$$

$$\left.\begin{aligned} y_{ex} &= -b_2 = (R_p + R_c)\cos\theta_{ex}, \\ \theta_{ex} &= \arccos\left(\frac{-b_2}{R_p + R_c}\right) \end{aligned}\right\} \tag{3.14}$$

$$x_{ex} = \sqrt{(R_p + R_c)^2 - {b_2}^2} + \frac{c\arccos\left(\frac{-b_2}{R_p + R_c}\right)}{2\pi} \tag{3.15}$$

In order to find the coordinates of the entrance and exit points P_{ent} and P_{ext}, $y_{ent} = b_1$ and $y_{ext} = -b_2$ are plugged in the current planetary revolution motion cutter periphery equation respectively (Equation 3.10). Two quadratic equations are obtained and from the solution of these equations the points with the greatest values that are the preceding points at the feed direction are selected.

$$x^2 - 2x_c x + {x_c}^2 + {b_1}^2 + {y_c}^2 - 2b_1 y_c - {R_c}^2 = 0 \tag{3.16}$$

$$x_{ent} = \frac{-c_1 + \sqrt{{c_1}^2 - 4c_2 c_0}}{2c_2} \tag{3.17}$$

where $c_2=1$, $c_1= -2\,x_c$, $c_0 = {x_c}^2+{b_1}^2+{y_c}^2+2b_1y_c-{R_c}^2$.

$$x^2 - 2x_c x + {x_c}^2 + {b_2}^2 + {y_c}^2 - 2b_2 y_c - {R_c}^2 = 0, \tag{3.18}$$

$$x_{ext} = \frac{-c_1 + \sqrt{{c_1}^2 - 4c_2 c_0}}{2c_2} \tag{3.19}$$

where c_2=1, c_1= -2 x_c, $c_0 = x_c^2+b_2^2+y_c^2+2b_2y_c-R_c^2$.

The point P_2 (the point with the lowest y coordinate on the periphery of the cutter intersecting with the previously machined surface) is achieved solving the current planetary revolution motion cutter periphery equation (Equation 3.10) and the previous planetary revolution motion workpiece equation (Equation 3.11) simultaneously.

$$\left.\begin{aligned} &\left(\left(R_p+R_c\right)\sin\theta-x_c\right)^2+\left(\left(R_p+R_c\right)\cos\theta-y_c\right)^2=R_c^{\,2}\\ &\theta^2\left(\frac{c^2}{4\pi^2}\right)+\theta\left(\frac{-x_c c}{\pi}\right)+\theta\sin\theta\left(\frac{\left(R_p+R_c\right)c}{\pi}\right)+\sin\theta\left(-2\left(R_p+R_c\right)x_c\right)\\ &+\cos\theta\left(-2\left(R_p+R_c\right)y_c\right)+\left(R_p+R_c\right)^2+x_c^{\,2}+y_c^{\,2}-R_c^{\,2}=0 \end{aligned}\right\} \quad (3.20)$$

This equation is solved with numerical methods with the initial guess such as θ angle in the current revolution and the solution θ is plugged into Equation 3.11 in order to achieve point $P_2(x_2, y_2)$.

All the necessary points are derived for calculation of the engagement. The engagement of the cutter is defined as follows in five different regions:

- **Prior to entrance to the workpiece ($y_c - R_c \geq b_1$, $y_c + R_c \geq b_1$ and $x_{ent} \leq x_{en}$)**

  The cutter tracing a trochoidal path has not yet engaged with the workpiece, therefore the start and exit angles defining the engagement of the cutter with the workpiece are all zero.

  $\phi_{st} = 0$, $\phi_{ex} = 0$.

- **Entrance to the workpiece ($y_c + R_c \geq b_1$ and $x_{ent} > x_{en}$)**

The cutter has just engaged with the workpiece. The start angle of the engagement is defined with the angle $\widehat{P_1P_cP_{ent}}$ shown in Figure 1 and the exit angle of the engagement is defined with the angle $\widehat{P_1P_cP_2}$.

The lengths of the line segments $|P_1P_c|$, $|P_{ent}P_c|$, $|P_2P_c|$, $|P_1P_{ent}|$ and $|P_1P_2|$ are calculated as given in the following equations below, respectively:

$$\left.\begin{aligned} L_{1c} &= L_{entc} = L_{2c} = R_c, \\ L_{1ent} &= \sqrt{(x_1 - x_{ent})^2 + (y_1 - y_{ent})^2}, \\ L_{12} &= \sqrt{(x_1 - x_2)^2 + (y_1 - y_2)^2} \end{aligned}\right\} \tag{3.21}$$

The start and exit angles are defined as follows:

$$\left.\begin{aligned} \phi_{st} &= \arccos\left(\frac{{L_{entc}}^2 + {L_{1c}}^2 - {L_{1ent}}^2}{2L_{1c}L_{entc}}\right), \\ \phi_{ex} &= \arccos\left(\frac{{L_{1c}}^2 + {L_{2c}}^2 - {L_{12}}^2}{2L_{1c}L_{2c}}\right) \end{aligned}\right\} \tag{3.22}$$

- **Continuous engagement ($y_1 \leq b_1$ and $y_2 \geq -b_2$)**

In this region the cutter performs a continuous machining operation with zero start angle. The exit angle of the engagement is defined similar to the previous region.

$$\phi_{st} = 0, \;\; \phi_{ex} = \arccos\left(\frac{{L_{1c}}^2 + {L_{2c}}^2 - {L_{12}}^2}{2L_{1c}L_{2c}} \right)$$

- **Exit from the workpiece ($y_2 \leq -b_2$ and $y_1 \geq -b_2$)**

The cutter has just finished the continuous engagement region and slowly retracts from the workpiece. The start angle of the engagement is zero as it is in the previous sections and the exit angle defined with angle $\widehat{P_1 P_c P_{ext}}$ is approaching to zero as the cutter completely exits from the workpiece. The lengths of the line segments $|P_{ext}P_c|$ and $|P_1 P_{ext}|$ are calculated as given in the following equation below:

$$\left.\begin{aligned} L_{extc} &= \sqrt{(x_{ext} - x_c)^2 + (y_{ext} - y_c)^2}\,, \\ L_{1ext} &= \sqrt{(x_1 - x_{ext})^2 + (y_1 - y_{ext})^2} \end{aligned}\right\} \qquad (3.23)$$

The exit angle is defined as follows:

$$\phi_{ex} = \arccos\left(\frac{{L_{extc}}^2 + {L_{1c}}^2 - {L_{1ext}}^2}{2L_{1c}L_{extc}} \right) \qquad (3.24)$$

- **After the exit from the workpiece ($y_1 \leq -b_2$)**

The cutter has just retracted from the workpiece therefore the start and exit angles defining the engagement of the cutter with the workpiece is all zero until the next planetary revolution.

$\phi_{st} = 0,\ \phi_{ex} = 0.$

3.3.2 Numerical Engagement Defining Algorithm

In this section a new algorithm capable of predicting the engagement for any given surface will be introduced. The analytical model explained in the previous section can only perform the engagement predictions for basic surfaces which do not contain any holes or bosses in it. However, most of the mechanical parts being machined have complex geometries and the prediction of the engagement and therefore cutting forces is of great value for the automation and the optimization of the process. The algorithm that will be explained in this section can utilize the prediction of the engagement for any given flat surfaces.

The algorithm uses the Unigraphics software as a source for the surface that will be machined. The STL (Standard Triangulation Language) output of the desired surface is exported and used as a source for the point cloud representation. Meanwhile, NURBS based G-code created by the Unigraphics software is employed for the precision representation of the CL points.

Due to the free-form shapes required for aerodynamic, ergonomic or purely aesthetic reasons, the machining of complex shapes needs a better toolpath verification rather than linear segmentation of cutter location points. Linear and circular interpolation algorithms are used in many CNC machines but they are not adequate enough for achieving the desired precision machining of free-form geometries. Recent research enabled the machining of complex geometries with NURBS applications. A NURBS, abbreviation for Non-Uniform Rational B-Spline, curve is defined as follows [25]:

$$P(t) = \frac{\sum_{i=0}^{n} N_{i,m}(t) w_i P_i}{\sum_{i=0}^{n} N_{i,m}(t) w_i} (x_{m-1} \le t \le x_{n+1}) \tag{3.25}$$

where $N_{i,m}(t)$ are the blending function defined by the recursive formula:

$$N_{i,1}(t) = \begin{cases} 1(x_i \le t \le x_{i+1}) \\ 0(t < x_i, x_{i+1} < t) \end{cases} \tag{3.26}$$

$$N_{i,k}(t) = \frac{(t - x_i) N_{i,k-1}(t)}{x_{i+k-1} - x_i} + \frac{(x_{i+k-t}) N_{i+1,k-1}(t)}{x_{i+k} - x_{i+1}}$$

where "P_i" and "w_i" denote respectively a control and the weight on the control point, "m" denotes the rank, and the NURBS curve of rank "m" is a curve of the $(m\text{-}1)^{th}$ order, "x_i" denotes a knot ($x_i \le x_{i+1}$), and an array of knots [$x_0\ x_1\ x_2 \ldots x_{n+m}$] is referred to as the knot vector.

However the CL points file will not be sufficient enough to define the engagement. The point $P_1(x_1, y_1)$ is obtained using center and radius of curvature (R_p). The center of the planetary revolutions $P_{c0}(x_{c0}, y_{c0})$ is defined (Figure 3.8) as below:

$$\left.\begin{array}{l} x_1 = x_{c0} + (R_p + R_c)\cos\theta,\ \ y_1 = y_{c0} + (R_p + R_c)\sin\theta \\ x_c = f(t),\ y_c = g(t) \end{array}\right\} \tag{3.26}$$

$$R_p = \frac{\left(f'^2 + g'^2\right)^{3/2}}{|f'g'' - f''g'|},\quad x_{c0} = f - \frac{\left(f'^2 + g'^2\right)g'}{f'g'' - f''g'},\quad y_{c0} = g + \frac{\left(f'^2 + g'^2\right)f'}{f'g'' - f''g'} \tag{3.27}$$

where $f' = x_c' = \frac{dx_c}{dt}$, $f'' = x_c'' = \frac{d^2x_c}{dt^2}$, $g' = y_c' = \frac{dy_c}{dt}$, $g'' = y_c'' = \frac{d^2y_c}{dt^2}$, and R_p is the radius of curvature. The time difference between each cutter location is achieved by dividing the distance traveled by the feedrate.

Afterwards the engagement defining procedure is employed. The procedure is rather simple but versatile as it is capable of dealing with all types of discontinuities within the surface. The algorithm uses the following logic.

- For each CL point obtained by using the NURBS interpolator, the algorithm defines the points within the surface enveloped by the perimeter of the cutter.
- Employing these points the engagement of the cutter with the workpiece is calculated. The closest point to the point P_1 (which is farthest point form the center of the planetary revolution) is used in calculating the start angle and the farthest point from the point P_1 is used in calculating the exit angle of the engagement.
- After calculation of the engagement for a CL point, the points enveloped by the cutter are deleted and the same procedure is applied for the next CL point.

3.4 Conclusions

This chapter presents the mechanistic cutting force model used for the force validations in this thesis and the engagement defining algorithms employed in the force model. The mechanistic cutting force model is taken from the previous studies of Altintas [2], and the engagement defining algorithms for trochoidal milling operation where the cutter traces a trochoidal toolpath are recently developed. Two different approaches are used for the engagement defining procedures: an analytical model capable of the defining the engagement for simple, filled surfaces and a numerical model for complex surfaces containing holes or bosses on themselves.

Chapter 4

CALIBRATION

4.1 Introduction

The accuracy and reliability of the force prediction algorithms rely on the calibration process. Once the calibration process of the cutting tool workpiece couple is carried out for specific cutting conditions and the cutting coefficients are determined, the force prediction algorithm becomes useable for every engagement condition within those specific cutting conditions.

The cutting coefficients for the cutting tool and material couple can be determined in the presence of knowing the cutting tool geometric parameters (diameter, rake and clearance angles), material parameters of the cutting tool and workpiece material (density, specific heat capacity and conductivity) and some coupled parameters (shear angle, friction angle and shear stress) obtained from the orthogonal cutting test. The superiority of this method is that the cutting coefficients of cutting tool workpiece pair can be determined even before manufacturing of the tool. Thereafter optimization of the tool parameters such as helix and clearance angles can be carried out in order to maximize the efficiency of the cutting tool. However, due to the complex geometry of some cutting edges of the tools, the evaluation of the cutting constants with orthogonal cutting data base may not give appropriate results or even shut the door on determination of the oblique milling constants. In such cases the mechanistic identification of the cutting constants is a good approach for simple determination of the cutting constants for the tool workpiece couple.

4.2 Mechanistic Identification of Cutting Constants

The proposed algorithm for the mechanistic identification of cutting constants is based on Altintas's approach [2]. In this method a set of milling experiments are performed with constant cutting velocity at varying feedrates keeping the radial and axial depth of cut constant and the average forces per tooth period is measured. In order to avoid the influence of the disturbances such as runout the average forces per spindle revolution are measured. Equating the analytically derived average cutting force expressions to the experimentally measured average cutting forces, the mechanistic identification of cutting constants in milling is carried out.

If we plug the tangential, radial and axial directions differential cutting force expressions (Equation 3.6) in the three orthogonal directions differential cutting force equations (Equation 3.7), with the necessary trigonometric operations and simplifications the three orthogonal directions differential cutting force can be expressed in terms of cutting coefficients K_{tc}, K_{rc}, K_{ac} ,K_{te}, K_{re} and K_{ae}), feed per tooth per revolution (t_x) , immersion angle (ϕ) and integration height as follows:

$$\begin{aligned}
dF_{x,j}(\phi_j(z)) &= \left\{ \begin{array}{l} \frac{t_x}{2}\left[K_{tc}\sin 2\phi_j(z) + K_{rc}(1-\cos 2\phi_j(z))\right] \\ +\left[K_{te}\cos\phi_j(z) + K_{re}\sin\phi_j(z)\right] \end{array} \right\} dz \\
dF_{y,j}(\phi_j(z)) &= \left\{ \begin{array}{l} \frac{t_x}{2}\left[-K_{tc}(1-\cos 2\phi_j(z)) + K_{rc}\sin 2\phi_j(z)\right] \\ +\left[-K_{te}\sin\phi_j(z) + K_{re}\cos\phi_j(z)\right] \end{array} \right\} dz \\
dF_{z,j}(\phi_j(z)) &= \left[K_{ac}t_x\sin\phi_j(z) + K_{ae}\right] dz
\end{aligned} \tag{4.1}$$

The presence of the helix angle in end mills softens the entrance of the cutter tooth to the workpiece but on the other hand it has no influence on the total amount of material removed per tooth period. Due to this fact the average cutting force are independent of helix

angle. Replacing integration height with radial depth of cut ($dz = a$), eliminating the lag angle and multiple tooth influence on the immersion angle ($\phi_j(z) = \phi$) in Equation (4.1) and integrating them over one revolution and dividing by the pitch angle (ϕ_p) outcomes with the average milling forces per tooth period as follows:

$$\begin{aligned}
\overline{F}_x &= \frac{1}{\phi_p}\int_{\phi_{st}}^{\phi_{ex}} F_x(\phi)d\phi \\
\overline{F}_y &= \frac{1}{\phi_p}\int_{\phi_{st}}^{\phi_{ex}} F_y(\phi)d\phi \\
\overline{F}_z &= \frac{1}{\phi_p}\int_{\phi_{st}}^{\phi_{ex}} F_z(\phi)d\phi
\end{aligned} \tag{4.2}$$

The integration limits are set as ϕ_{st} and ϕ_{ex} since the tooth cuts in the engagement region. Integrating the average milling cutting forces yields the following average cutting force expression in three orthogonal directions.

$$\begin{aligned}
\overline{F_x} &= \left\{\frac{Nat_x}{8\pi}\left[-K_{tc}\cos 2\phi + K_{rc}(2\phi - \sin 2\phi)\right] + \frac{Na}{2\pi}\left[K_{te}\sin\phi - K_{re}\cos\phi\right]\right\}_{\phi_{st}}^{\phi_{ex}} \\
\overline{F_y} &= \left\{\frac{Nat_x}{8\pi}\left[-K_{tc}(2\phi - \sin 2\phi) - K_{rc}\cos 2\phi\right] + \frac{Na}{2\pi}\left[K_{te}\sin\phi + K_{re}\cos\phi\right]\right\}_{\phi_{st}}^{\phi_{ex}} \\
\overline{F_z} &= \frac{Na}{2\pi}\left[-K_{ac}t_x\cos\phi - K_{ae}\phi\right]_{\phi_{st}}^{\phi_{ex}}
\end{aligned} \tag{4.3}$$

A simple analysis on this equation yields out the fact that the average milling cutting forces can be expressed in terms of a linear function of the feed per revolution term contributed by the cutting forces and an offset contributed by the edge forces. A set of milling experiments are performed with constant cutting velocity at varying feedrates keeping the radial and axial depth of cut constant and the average forces per tooth period is

measured at each feedrate, and the average cutting and edge components ($\overline{F}_{qc}, \overline{F}_{qe}$; $q=x,y,z$) are estimated by a linear regression of the cutting data.

$$\begin{aligned}\overline{F}_x &= \overline{F}_{xc} + \overline{F}_{xe} \\ \overline{F}_y &= \overline{F}_{yc} + \overline{F}_{ye} \\ \overline{F}_z &= \overline{F}_{zc} + \overline{F}_{ze}\end{aligned} \tag{4.4}$$

Equalizing the analytical cutting force expression (Equation 4.3) to the experimentally measured average cutting and edge components; tangential, radial and axial direction cutting end edge coefficient are obtained.

Mechanistic identification of cutting constants is most convenient with full slot cutting milling experiment (ϕ_{st} = 0 and ϕ_{ex} = π). These integration limits simplifies the average cutting force expressions as follows:

$$\begin{aligned}\overline{F_x} &= \frac{Na}{4} K_{rc} f_t + \frac{Na}{\pi} K_{re} \\ \overline{F_y} &= -\frac{Na}{4} K_{tc} f_t + \frac{Na}{\pi} K_{te} \\ \overline{F_z} &= \frac{Na}{4} K_{ac} f_t + \frac{Na}{\pi} K_{ae}\end{aligned} \tag{4.5}$$

The cutting force and edge coefficients are evaluated as below:

$$\begin{aligned}K_{tc} &= -\frac{4\overline{F}_{yc}}{Na}\ ,\ K_{te} = -\frac{\pi\overline{F}_{ye}}{Na} \\ K_{rc} &= -\frac{4\overline{F}_{yc}}{Na},\ K_{te} = -\frac{\pi\overline{F}_{ye}}{Na} \\ K_{ac} &= \frac{\pi\overline{F}_{zc}}{Na},\ K_{te} = \frac{2\overline{F}_{ze}}{Na}\end{aligned} \tag{4.6}$$

The experiments for calibration were performed on Mazak FJV-200 UHS Vertical Machining Center (VMC) with 25000 rpm spindle motor, ± 2.5 micron sensitivity and, ± 0.7 micron repeatability. A Carbide high performance ISO N end mill cutter from CoroMill Plura series of Sandvik with 2 flutes, 12 mm diameter, 100 mm total length, 38 mm flute length, 25° helix angle used for the calibration tests.. The workpiece material was aluminum (Al7039) block of size 250 x 170 x 40 mm. Kistler 3-component dynamometer (Model 9257B), a Kistler charge amplifier (Model 5019) and a National instruments I/O box (Model BNC-2110) have been used to measure cutting forces. The 3-component dynamometer has been fixed to the machine table using fixtures and the workpiece blocks were attached to the dynamometer using two M8 screws as seen in Figure 4.1.

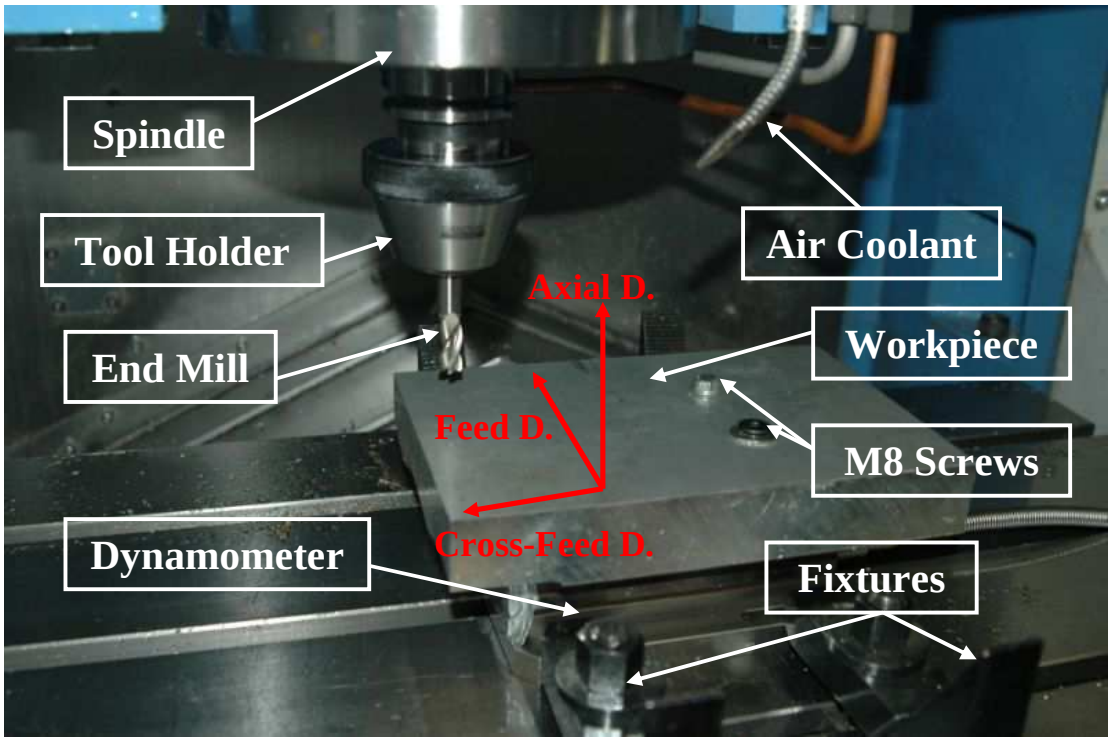

Figure 4.1: Workpiece and 3-component dynamometer fixed on top of each other to vertical machining center machine table for cutting tests.

The cutting forces are sensed by the piezoelectric transducers in the dynamometer and an electric charge output is the outcome of this process. This electric charge is later taken by the charge amplifier and converted into voltage output. The sensitivity values for the three channels (x, y and z) in the amplifier were -7.87, -7.90, and -3.69 pC/N respectively. Amplifier gain for the device was set to 100 N/V for X and Y channels and 50 N/V for Z channel. Subsequently, through use of a proper data acquisition card with 200 kS/s sampling rate, ± 5 V analog input and software, the voltage output is displayed and recorded as cutting forces in Newton. Displaying and recording of the measured data was realized with a data acquisition program, MALDAQ module of CutPro 6. (See Figure 4.2 for a sample output screen of CutPro). The complete actual testing environment can be seen in Figure 4.3.

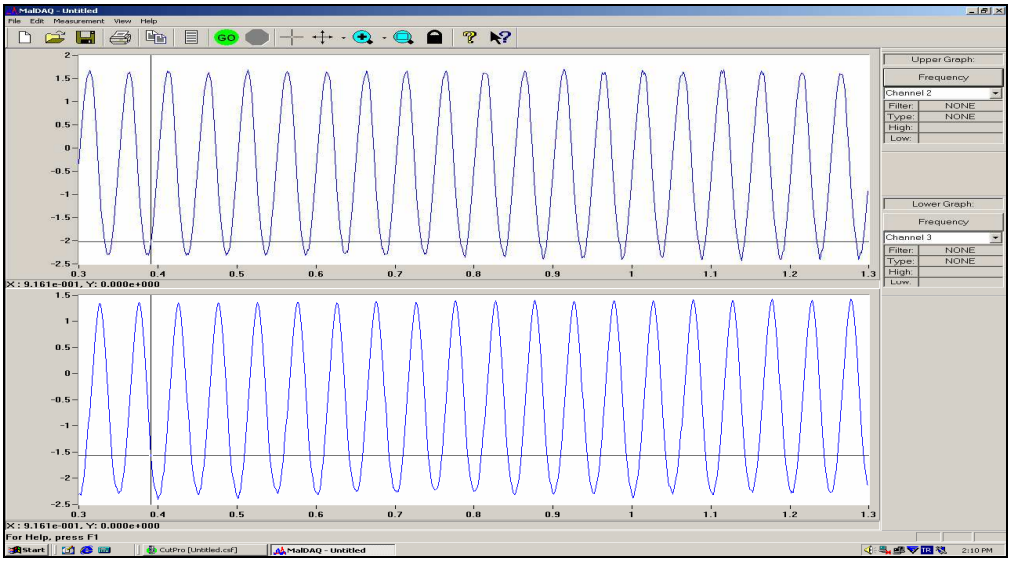

Figure 4.2: Sample output screen in MalDAQ module of CutPro 6 for cutting forces.

a

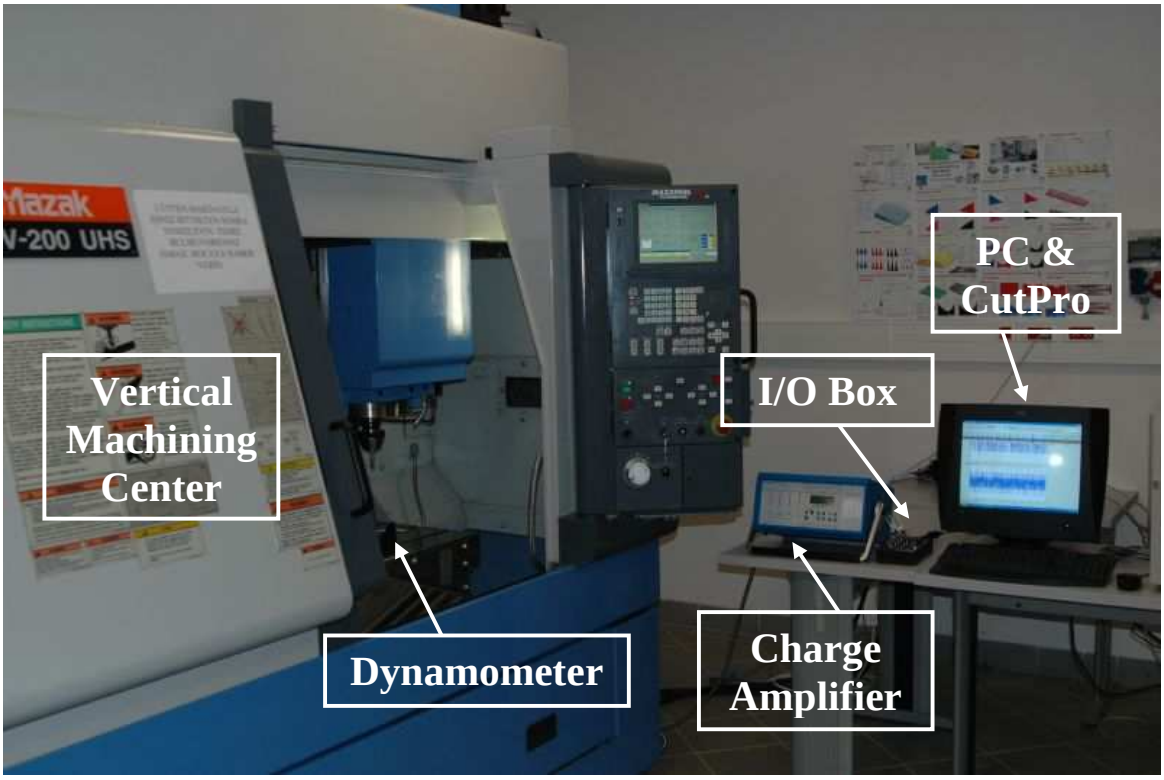

b

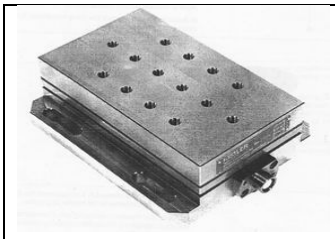		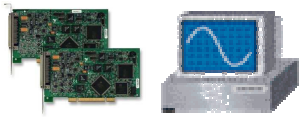
Cutting forces forms an electric charge output from the piezoelectric sensors on the dynamometer	Charge output is amplified and send to the DAQ card via I/O Box	Cutting forces are recorded via digital signal achieved from the DAQ card

Figure 4.3: The experimental setup for measurement of cutting forces a) Actual testing environment, b) Detailed illustration of the components.

4.2.1 Sandvik 12 mm End Mill Calibration

As explained in the previous section a set of milling experiments at constant cutting velocity, axial and radial depth of cut with varying feedrates is carried out and the average cutting forces per spindle revolution are determined. The 60-150 mm/min feedrate interval with 30 mm/min increments at 600 rpm spindle speed (n) has been tested for Sandvik 12 mm end mill – aluminum 7039 material pair. Specifications and visualization of the Sandvik cutter are given in Table 4.1 and Figure 4.4 respectively. Force measurements are carried out at 1000 Hz sampling frequency rate (f_s), constituting 3.6 ° sampling rotation angle ($\Delta\phi$) for the cutting conditions under investigation. In order to minimize the effects of local disturbances, average forces per 100 spindle revolution periods were collected. Moreover two sets of experiments were performed to increase the reliability of the results.

$$\Delta\phi = \frac{2\pi \frac{n}{60}}{f_s} \tag{4.7}$$

Table 4.1: Cutter specifications.

Cutter	CoroMill Plura High Performance ISO N End Mill
Number of flutes	2
Diameter	12 mm
Total length	100 mm
Flute length	38 mm
Helix angle	25º

Figures 4.5, 4.6 and 4.7 indicate the feed, cross-feed and axial directions cutting forces per spindle revolution period for the feedrate interval 90-150 mm/min at test 1 sampled at every 3.6 ° spindle revolution.

Figure 4.4: Sandvik 12 mm CoroMill Plura end mill.

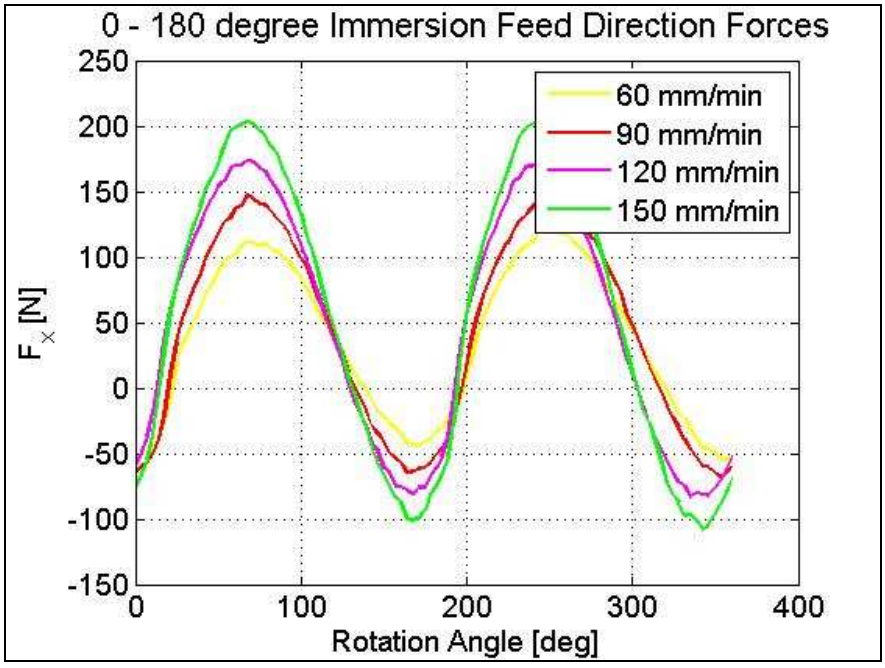

Figure 4.5: 0 - 180 ° immersion feed direction cutting forces.

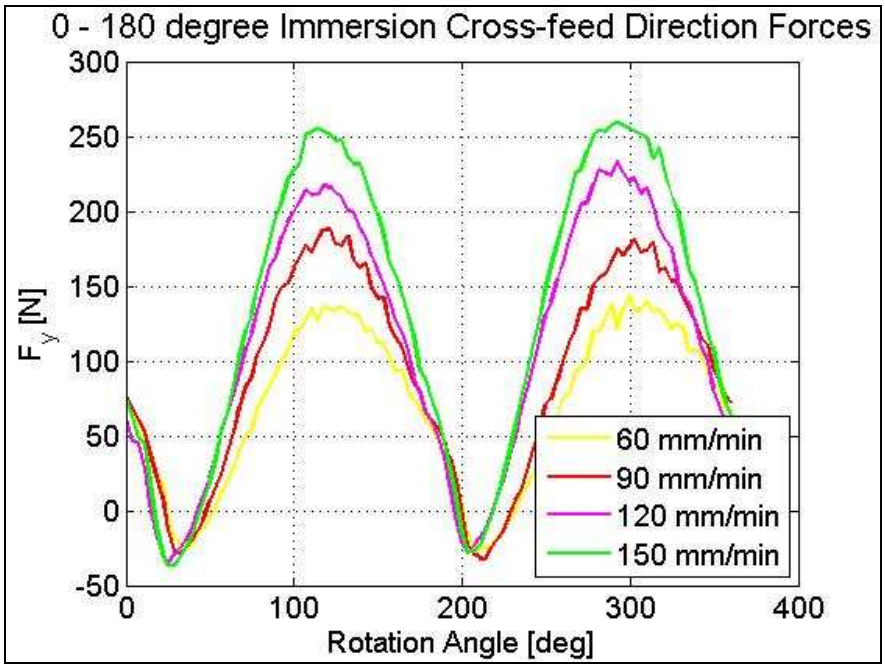

Figure 4.6: 0 - 180 ° immersion cross-feed direction cutting forces.

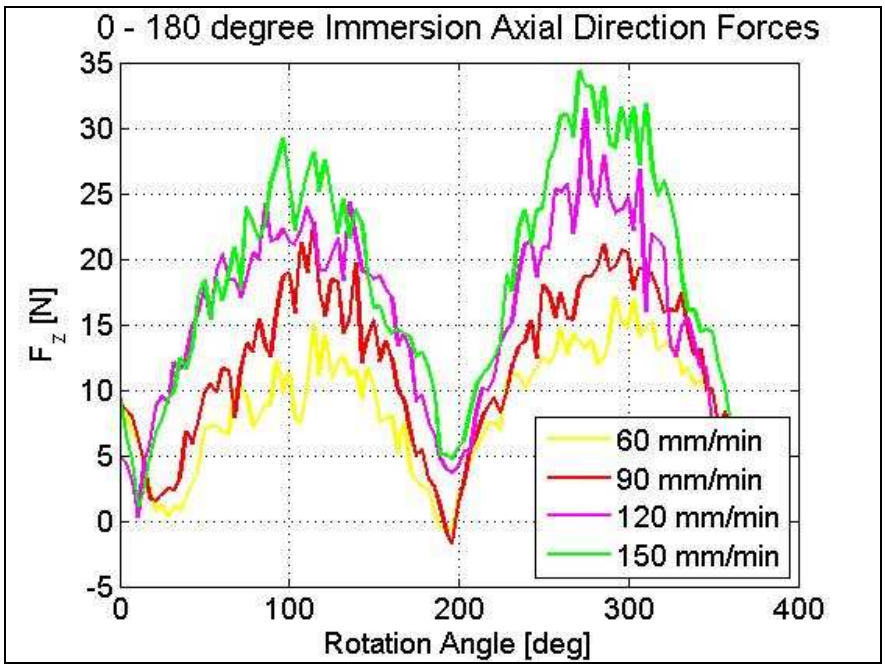

Figure 4.7: 0 - 180 ° immersion axial direction cutting forces.

Tables 4.2 and 4.3 indicates the feed, cross-feed and axial directions average cutting and edge forces; and tangential, radial and axial directions cutting and edge coefficients respectively for Sandvik 12 mm end mill and aluminum 7039 workpiece material pair. In Figure 4.8 average cutting forces versus feedrate value in X, Y, Z directions is given.

Table 4.2: Feed, cross-feed and axial directions average cutting and edge forces.

Feed Direction		**Cross-feed Direction**		**Axial Direction**	
Average Cutting Force $\overline{F}_{xc}$ [N/mm]	**Average Edge Force** $\overline{F}_{xe}$ [N]	**Average Cutting Force** $\overline{F}_{yc}$ [N/mm]	**Average Edge Force** $\overline{F}_{ye}$ [N]	**Average Cutting Force** $\overline{F}_{zc}$ [N/mm]	**Average Edge Force** $\overline{F}_{ze}$ [N]
253.9	24.6	845.9	26.6	132.8	1.9

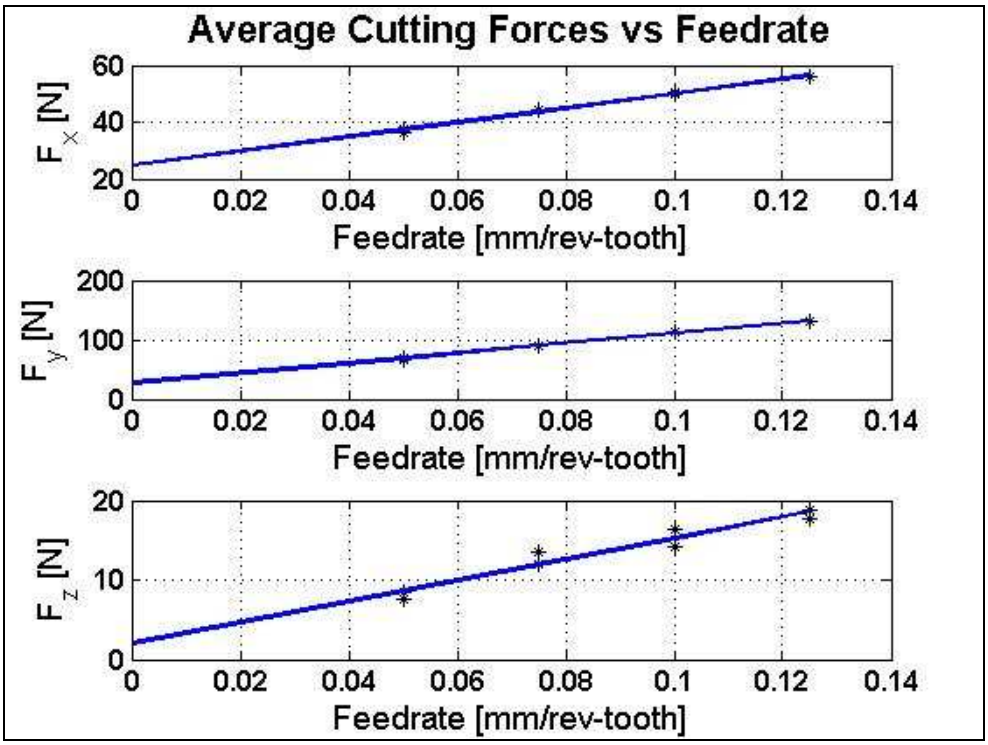

Figure 4.8: Sandvik 12 mm end mill – Al 7039 average X, Y, Z directions cutting forces versus feedrate.

Table 4.3: Cutting and edge coefficients for Sandvik 12 mm end mill and Al 7039 workpiece pair.

Tangential Cutting Coefficient K_{tc} [N/mm^2]	**Tangential Edge Coefficient** K_{te} [N/mm]	**Radial Cutting Coefficient** K_{rc} [N/mm^2]	**Radial Edge Coefficient** K_{re} [N/mm]	**Axial Cutting Coefficient** K_{ac} [N/mm^2]	**Axial Edge Coefficient** K_{ae} [N/mm]
874	14	218	13	118	1.3

Using these coefficients force model explained in the previous section was employed for slot cutting conditions with 2 mm radial depth of cut at 120 mm/min feedrate and 600 rpm spindle speed. Figures 4.9, 4.10 and 4.11 indicate the feed, cross-feed and axial direction measured and simulation cutting forces. The experimental and simulation cutting forces are in good correspondence with each other.

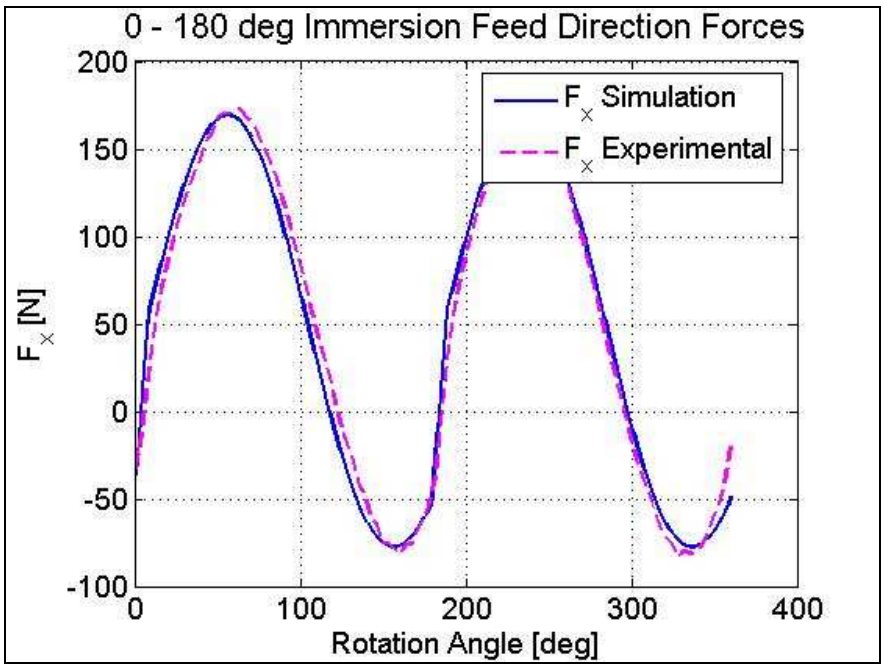

Figure 4.9: Feed direction experimental and simulation cutting forces at 120 mm/min.

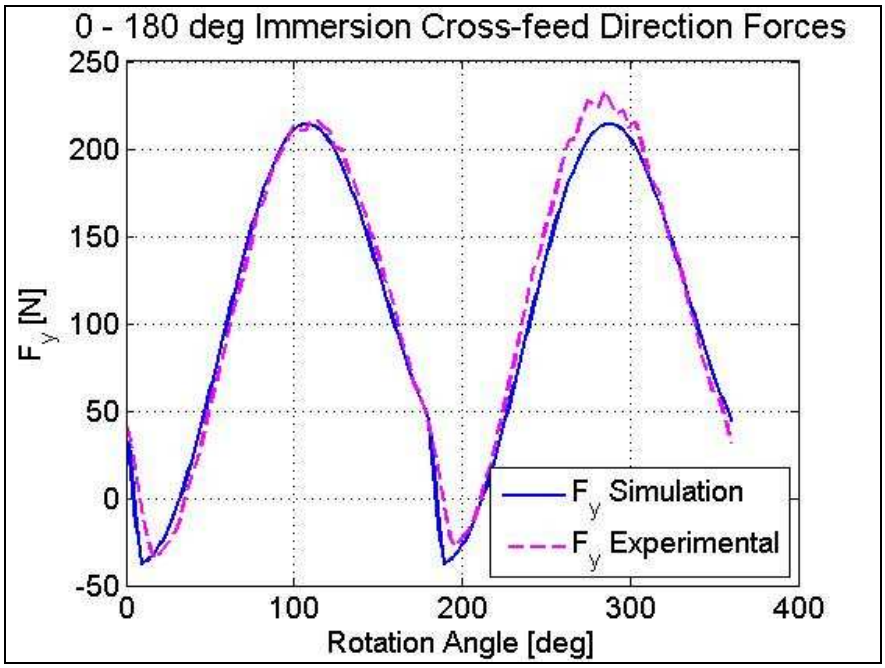

Figure 4.10: Cross-feed direction experimental & simulation cutting forces at 120 mm/min.

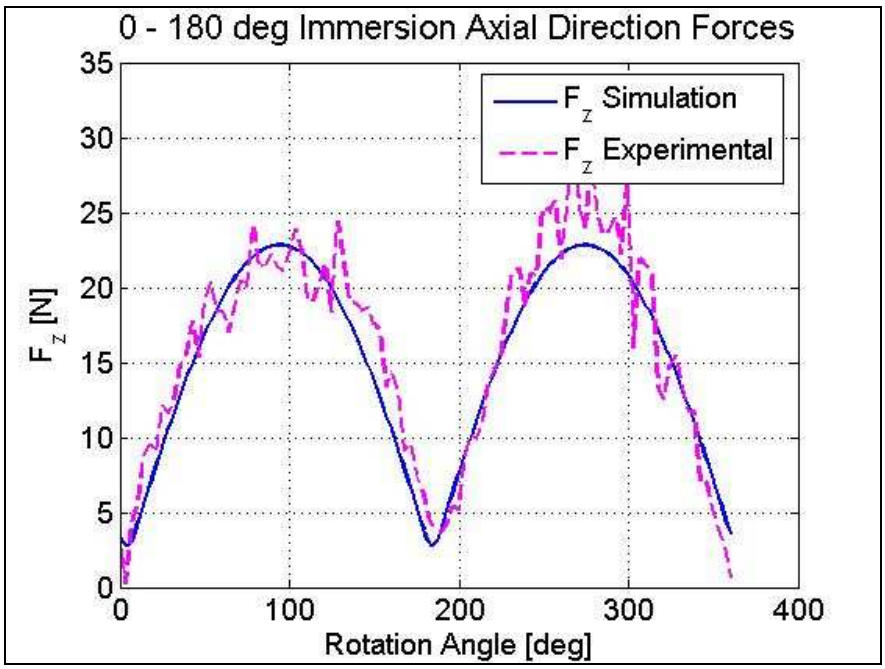

Figure 4.11: Axial direction experimental and simulation cutting forces at 120 mm/min.

The determination of the cutting constants can also be performed using the tangential, radial and axial cutting forces. First of all the angular phase differences were detected for all the collected data and by accounting these differences all experimental force data have been equally aligned. Thereafter, using the inverse of the transformation matrix given in Equation 3.7; collected force components (F_x, F_y, F_z) were transformed into tangential, radial and axial components (F_t, F_r, F_a) (Figures 4.12, 4.13). Assuming the axial depth of cut is small enough resulting to very small lag angle the transformation can be performed easily ignoring the lag angle. The experimental measurements were carried out at a 3.6 ° sampling rotation angle ($\Delta\phi$) thus causing the precision of the transformation was ± 3.6 º. Average tangential, radial and axial direction cutting forces per spindle revolution period were plotted versus average chip thickness in order to obtain the cutting coefficients (4.14). Determination of the cutting constants from experimental data is summarized in Figure (4.15). Tables 4.4 and 4.5 indicates the tangential, radial and axial directions average cutting and edge forces; and tangential, radial and axial directions cutting and edge coefficients obtained from tangential, radial and axial direction cutting forces respectively.

Table 4.4: Tangential, radial and axial directions average cutting and edge forces.

Tangential Direction		**Radial Direction**		**Axial Direction**	
Average Cutting Force $\overline{F}_{tc}$ [N/mm]	**Average Edge Force** $\overline{F}_{te}$ [N]	**Average Cutting Force** $\overline{F}_{rc}$ [N/mm]	**Average Edge Force** $\overline{F}_{re}$ [N]	**Average Cutting Force** $\overline{F}_{zc}$ [N/mm]	**Average Edge Force** $\overline{F}_{ze}$ [N]
1635.6	40.6	508.6	38.6	132.8	1.9

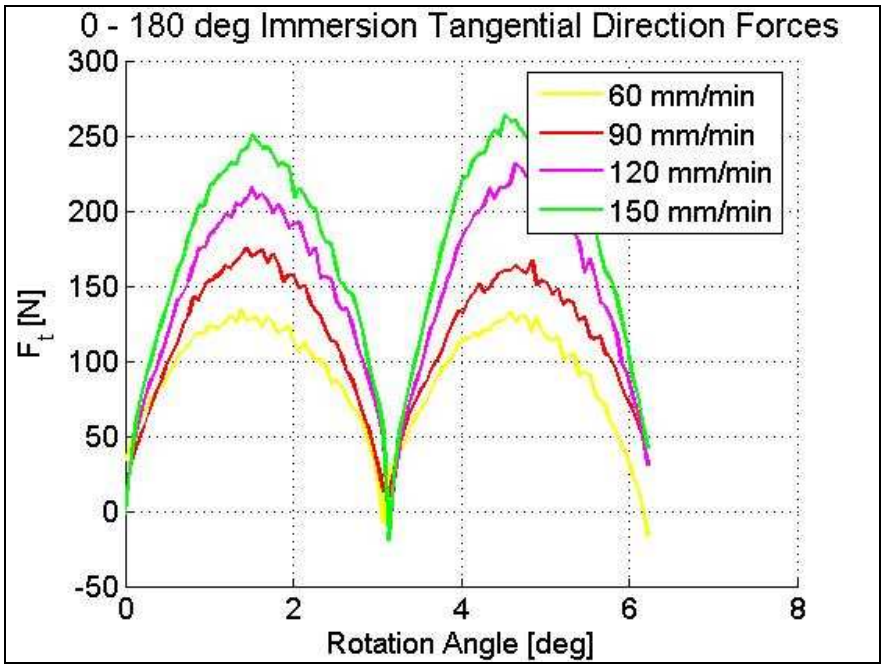

Figure 4.12: 0 - 180 ° immersion tangential direction cutting forces.

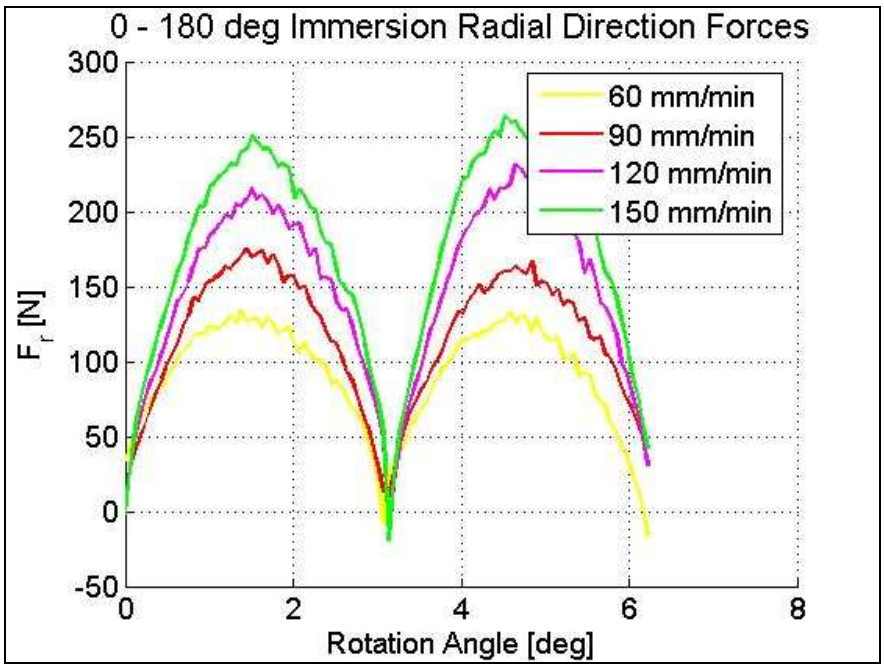

Figure 4.13: 0 - 180 ° immersion radial direction cutting forces.

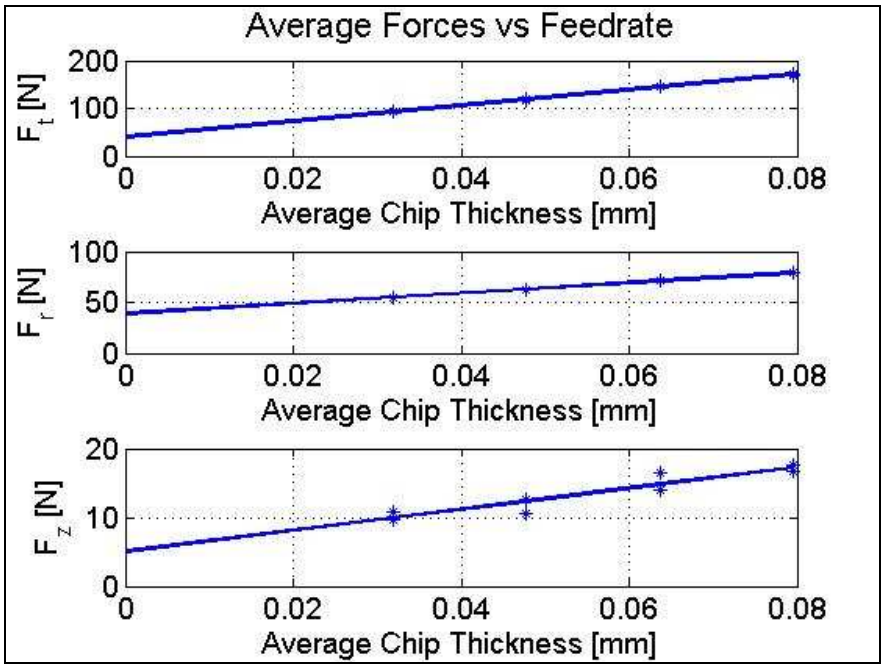

Figure 4.14: Sandvik 12 mm end mill – Al 7039 average tangential, radial and axial directions cutting forces versus average chip thickness.

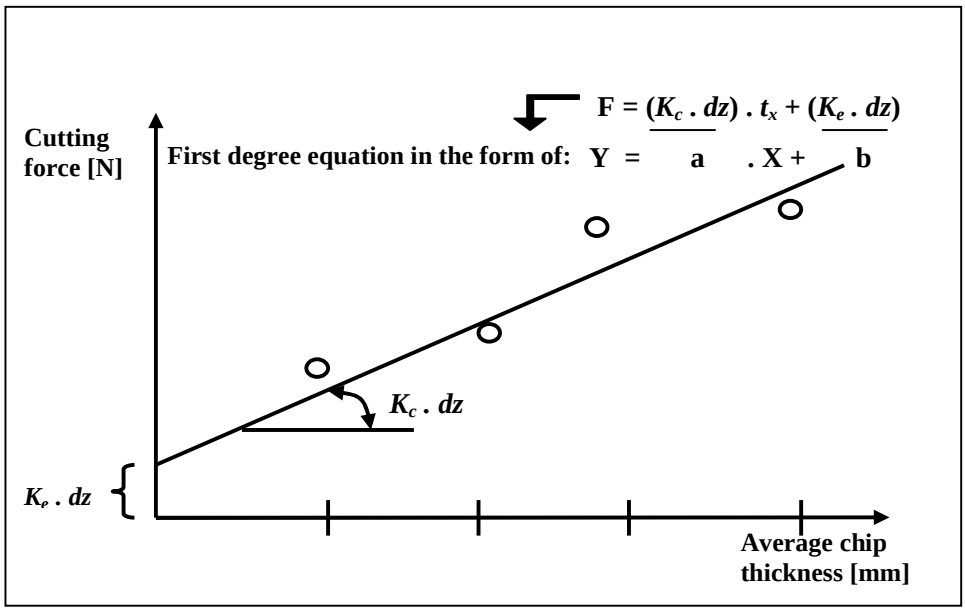

Figure 4.15: Determination of the cutting coefficients from experimental data from Guzel [34].

Table 4.5: Cutting and edge coefficients for Sandvik 12 mm end mill and Al 7039 workpiece pair obtained from tangential, radial and axial average cutting forces.

Tangential Cutting Coefficient K_{tc} [N/mm^2]	**Tangential Edge Coefficient** K_{te} [N/mm]	**Radial Cutting Coefficient** K_{rc} [N/mm^2]	**Radial Edge Coefficient** K_{re} [N/mm]	**Axial Cutting Coefficient** K_{ac} [N/mm^2]	**Axial Edge Coefficient** K_{ae} [N/mm]
818	20	254	19	118	1.3

Using these coefficients force model explained in the previous section was employed for slot cutting conditions with 2 mm radial depth of cut at 120 mm/min feedrate and 600 rpm spindle speed. Figures 4.16 and 4.17 indicate the feed, cross-feed and axial direction measured and simulation cutting forces. The experimental and simulation cutting forces are in good correspondence with each other.

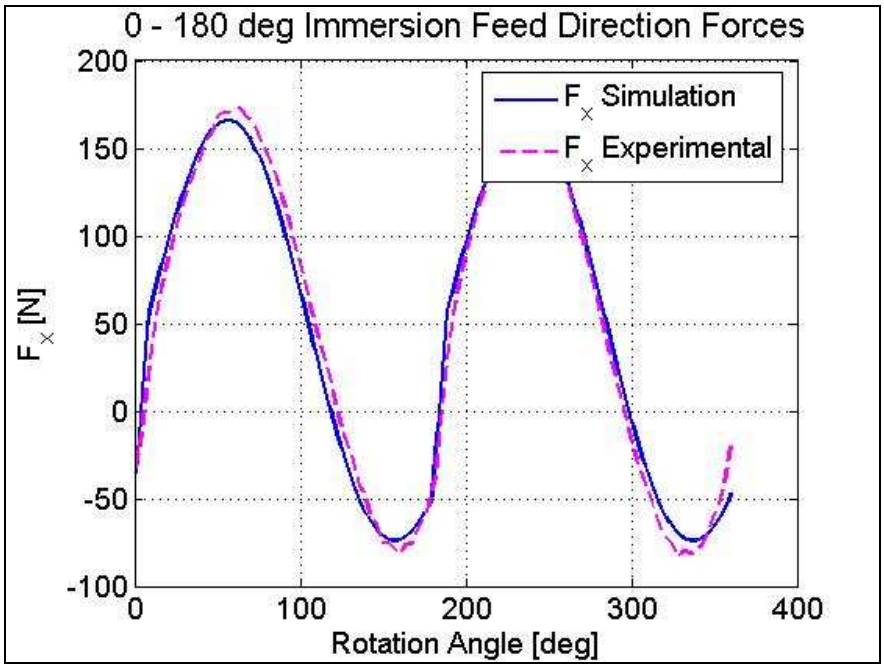

Figure 4.16: Feed direction experimental and simulation cutting forces at 120 mm/min.

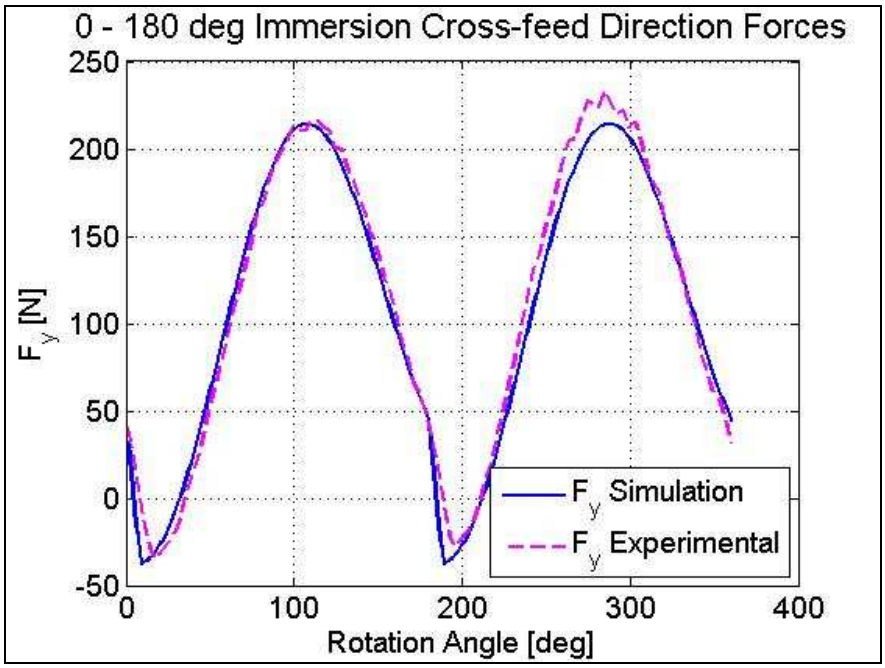

Figure 4.17: Cross-feed direction experimental and simulation cutting forces at 120 mm/min.

4.3 Influence of Radial Depth of Cut in Mechanistic Identification of Milling Constants

Mechanistic identification of milling constants experiments are conducted at different feedrates but at constant immersion and axial depth of cut. Although full immersion milling experiments are most convenient any immersion condition can be employed. By equalizing Equation 4.3 and 4.4 the following expressions for the cutting constants is obtained.

$$\begin{bmatrix} K_{tc} \\ K_{rc} \end{bmatrix} = A^{-1} \begin{bmatrix} \overline{F}_{xc} \\ \overline{F}_{yc} \end{bmatrix}, \begin{bmatrix} K_{te} \\ K_{re} \end{bmatrix} = B^{-1} \begin{bmatrix} \overline{F}_{xe} \\ \overline{F}_{ye} \end{bmatrix}, \begin{bmatrix} K_{ac} \\ K_{ae} \end{bmatrix} = \begin{bmatrix} \dfrac{2\pi}{Na\cos(\phi)} \\ \dfrac{2\pi}{Na\phi} \end{bmatrix}_{\phi_{st}}^{\phi_{ex}} \begin{bmatrix} \overline{F}_{zc} \\ \overline{F}_{ze} \end{bmatrix} \tag{4.7}$$

where

$$A=\left[\begin{array}{cc} \frac{-Na}{8\pi}\cos(2\phi) & \frac{Na}{8\pi}2\phi-\sin(2\phi) \\ \frac{-Na}{8\pi}2\phi-\sin(2\phi) & \frac{-Na}{8\pi}\cos(2\phi) \end{array}\right]_{\phi_{st}}^{\phi_{ex}},\ B=\left[\begin{array}{cc} \frac{Na}{2\pi}\sin(\phi) & \frac{-Na}{2\pi}\cos(\phi) \\ \frac{Na}{2\pi}\cos(\phi) & \frac{Na}{2\pi}\sin(\phi) \end{array}\right]_{\phi_{st}}^{\phi_{ex}} \quad (4.8)$$

En experimental study was carried on in order to emphasize the influence of immersion conditions on the cutting force and edge coefficients. Two sets of calibration tests were done for 7 different immersion conditions (0 – 180° slot cutting, 0 – 120° up milling, 60 – 180° down milling, 0 – 90° up milling, 90 – 180° down milling, 0 – 60° up milling, 60 – 180° down milling) with TaeguTec 8 mm end mill cutter and DIN 1.2842 steel at 50 HRc couple. Specifications and visualization of the TaeguTec cutter are given in Table 4.6 and Figure 4.18 respectively. The 15-60 mm/min feedrate interval with 15 mm/min increments at 1200 rpm spindle speed (n) has been tested for TaeguTec 8 mm end mill – steel 2842 material pair. Charge amplifier parameters are set as follows: The sensitivity values for the three channels (x, y and z) in the amplifier were -7.89, -7.93, and -3.69 pC/N respectively. Amplifier gain for the device was set to 200 N/V for X and Y channels and 10 N/V for Z channel. Force measurements are carried out at 2000 Hz sampling frequency rate (f_s), constituting 3.6 ° sampling rotation angle ($\Delta\phi$) for the cutting conditions under investigation. The tangential, radial and axial directions cutting and edge coefficients for the 7 immersion condition is given in Table 4.7 (Slot cutting 0° - 180°, 0° - 120°, 60° - 180°, 0° - 90°, 90° - 180°, 0° - 60°, 120° - 180°).

Table 4.6: Cutter specifications.

Cutter	TaeguTec HES 2080T TT9030
Number of flutes	2
Diameter	8 mm
Total length	60
Flute length	20
Helix angle	30

Figure 4.18: TaeguTec 8 mm end mill.

Calibration results show that cutting force coefficients are in strong correlation with the immersion conditions. Tangential and axial direction cutting coefficients are higher for down milling rather than up milling condition. On the contrary radial cutting coefficients are higher for up milling rather than down milling condition. Similarly radial and axial direction edge coefficients are higher for down milling rather than up milling condition. However, there is no constant correlation for tangential edge coefficients.

Table 4.7: Cutting and edge coefficients for TaeguTec 8 mm end mill and DIN 1.2842 steel workpiece pair obtained for various immersion conditions.

Cutting Coefficients	**0 – 180° Slot Cutting**	**0 – 120° Up Milling**	**60 – 180° Down Milling**	**0 – 90° Up Milling**	**90 – 180° Down Milling**	**0 – 60° Up Milling**	**120 – 180° Down Milling**
K_{tc} [N/mm^2]	4339	3936	4879	4699	5430	5305	7141
K_{te} [N/mm]	88	92	82	97	82	75	79
K_{rc} [N/mm^2]	4764	6586	4668	7562	4760	8398	5843
K_{re} [N/mm]	117	94	115	107	114	83	108
K_{ac} [N/mm^2]	1127	605	1084	1049	1389	1368	1752
K_{ae} [N/mm]	67	33	71	61	80	47	97

These obtained coefficients are used in the mechanistic force model algorithm for the 7 immersion conditions. At every discrete angular rotation the root mean square (RMS) of the difference between experimental and simulated force values are determined. The results

are shown in Table 4.8. Interpretation of the results indicate that 0 - 180° immersion slot cutting tests gives the best calibration coefficients for all the immersion conditions. Using coefficients obtained from 0 - 180° immersion slot cutting tests, the errors between the results of the force simulation program and experimental data are lower than 20 % on the average in feed, cross-feed and axial directions. Figure 4.19 shows the average of the RMS of the error between the experimental and simulation values for coefficients obtained from 7 different immersion conditions.

Table 4.8: RMS of the error between the experimental and simulation values for all the 7 immersion conditions indicating the immersion condition from which the coefficients are obtained.

Error RMS %			Situation Used						
			0 – 180 Slot Cutting	0 – 120 Up Milling	60 – 180 Down Milling	0 – 90 Up Milling	90 – 180 Down Milling	0 – 60 Up Milling	120 – 180 Down Milling
Coefficients Used	x	0 – 180 Slot Cutting	18,2	18,1	17,6	27,9	17,7	14,6	13,4
	y		23,9	20,4	23,1	20,3	23,9	14,3	17,3
	z		15,1	18,7	14,7	15,2	15,9	9,8	18,1
	x	0 – 120 Up Milling	22,7	14,1	24,4	23,0	23,5	14,7	15,8
	y		28,5	19,0	24,7	15,1	24,5	10,1	19,1
	z		37,8	39,3	37,6	35,4	26,9	30,4	17,8
	x	60 – 180 Down Milling	17,1	18,7	17,0	27,8	16,8	13,9	13,0
	y		23,8	21,7	23,1	21,5	23,7	14,7	17,5
	z		40,3	41,3	39,5	37,3	28,5	32,0	18,7
	x	0 – 90 Up Milling	48,1	32,4	41,9	22,8	33,7	21,0	18,8
	y		38,3	25,5	34,7	21,0	32,5	14,0	23,8
	z		31,2	46,2	32,2	30,9	22,8	26,7	15,6
	x	90 – 180 Down Milling	18,2	16,3	18,3	26,2	16,8	13,8	12,4
	y		27,2	25,7	25,8	24,8	24,8	15,9	17,9
	z		54,4	66,2	51,2	46,5	37,7	39,3	24,6
	x	0 – 60 Up Milling	44,6	28,0	39,9	16,3	33,3	15,2	19,9
	y		31,9	22,9	30,2	16,4	28,4	10,4	22,0
	z		24,6	40,0	27,4	24,8	19,2	21,1	14,9
	x	120 – 180 Down Milling	31,2	22,0	26,6	21,0	19,9	18,4	13,6
	y		46,2	42,8	43,4	34,8	36,7	18,4	23,3
	z		76,4	84,8	69,4	61,5	52,5	50,9	35,1

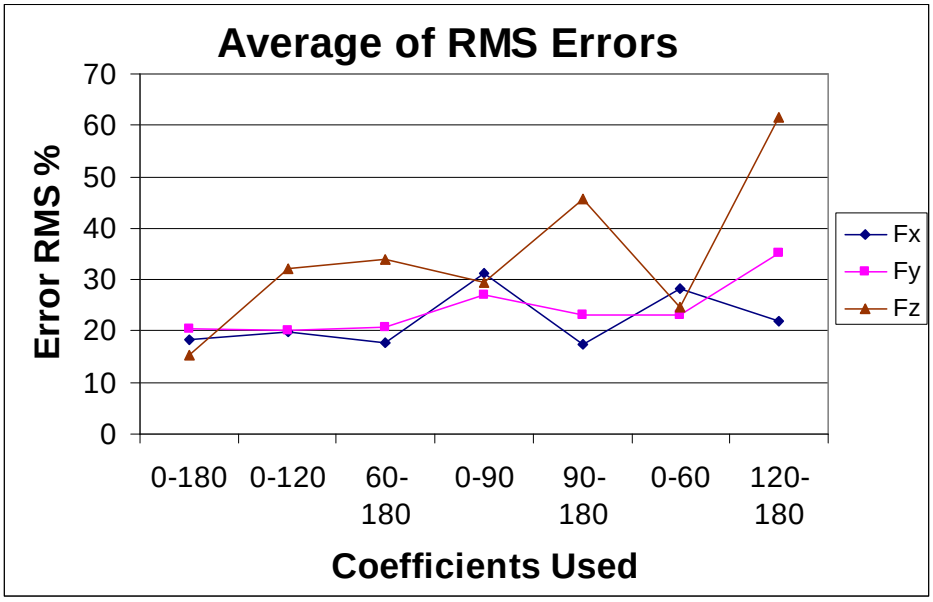

Figure 4.19: The average RMS of the error between the experimental and simulation values for coefficients obtained from 7 different immersion conditions.

4.4 Conclusion

This chapter presents the determination of the cutting coefficients with the mechanistic approach. After performing a set of milling experiments with constant cutting velocity at varying feedrates keeping the radial and axial depth of cut constant, the average forces per tooth period is measured. Equating the analytically derived average cutting force expressions to the experimentally measured average cutting forces, the mechanistic identification of cutting constants in milling is carried out.

Sandvik 12 mm end mill is calibrated using the mechanistic approach. Moreover an experimental study on influence of radial depth of cut in mechanistic identification of milling constants is carried

Chapter 5

MODIFICATION OF TROCHOIDAL MILLING TOOLPATH

5.1 Introduction

Trochoidal milling is used in many commercial CAD/CAM programs especially for hard milling applications due to the restricted engagement conditions that both lowers the cutting forces and heat generation on the cutter chip contact face. However, due to the trochoidal toolpath of the cutter machining cycle times increase in a considerable amount depending on the radius of the planetary revolution and the stepover value between the planetary revolutions. Due to the nature of the trochoidal toolpath, after completing half of the planetary revolution where the cutter performs cutting operation, there is another half planetary revolution where the cutter does not perform cutting. The main motivation in this section is to optimize trochoidal toolpath in order to reduce the machining cycle time.

Feedrate scheduling has attracted great attention in the recent years for the improvement procedure of the machining efficiency. Researchers employed different strategies for the feedrate scheduling algorithms such as material removal rate (MRR) based and force based feedrate scheduling (FFS). MRR based feedrate scheduling algorithm relies on only the volumetric analysis and the feedrate is optimized using an inverse proportion to the average or instantaneous volumetric material removal rate. On the other hand FFS relies on the physics of the cutting mechanism and the algorithm ensures a smoother maximum force profile. As we already have a reliable quantitative force model, FFS is applicable to trochoidal milling easily in order to reduce cycle times without sacrificing the machining quality.

5.2 Toolpath Modification for Trochoidal Milling

As the cutter traces a trochoidal path along the end milling operation engagement of the cutter with the workpiece shows an inconsistent behavior. During the back half of the planetary revolution in the feed direction contact of the cutter with the workpiece is no more valid. Therefore half of the production cycle is uncutting. In order to avoid this situation, two toolpath modification algorithms are considered: Trochoidal toolpath with straight linear motion at the back half of planetary revolution in feed direction, double trochoidal milling mechanism.

The first one is trochoidal toolpath with straight linear motion at the back half of planetary revolution in feed direction. With the help of this toolpath not only the machining time is shortened but also the generated forces during trochoidal milling are kept unchanged as the toolpath modification algorithm is employed during the interval that the cutter does not perform cutting. The toolpath for the cutter center (P_c) for trochoidal milling operation is given in Equation 3.9 considering small increments in angle defining the position of the cutter teeth θ. Figure 5.1 indicates the toolpath for trochoidal milling with the parameters 20 mm planetary revolution radius (R_p) and 5 mm stepover between each planetary revolution. In the modified algorithm the toolpath of the cutter center is given as follows:

$$x_c = \begin{cases} R_p \sin\theta + \dfrac{c\theta}{2\pi} & if \quad 0 < \theta \le \pi \\ R_p \sin(\kappa + \pi) + \dfrac{c\theta}{2\pi} & if \quad \pi < \theta \le 2\pi \end{cases} \qquad (5.1)$$

$$y_c = R_p \cos\theta$$

where κ is $\left\lfloor \dfrac{\theta}{2\pi} \right\rfloor$. In Figure 5.2 the cutter center toolpath for modified trochoidal milling algorithm with straight linear motion for back half planetary revolution is shown.

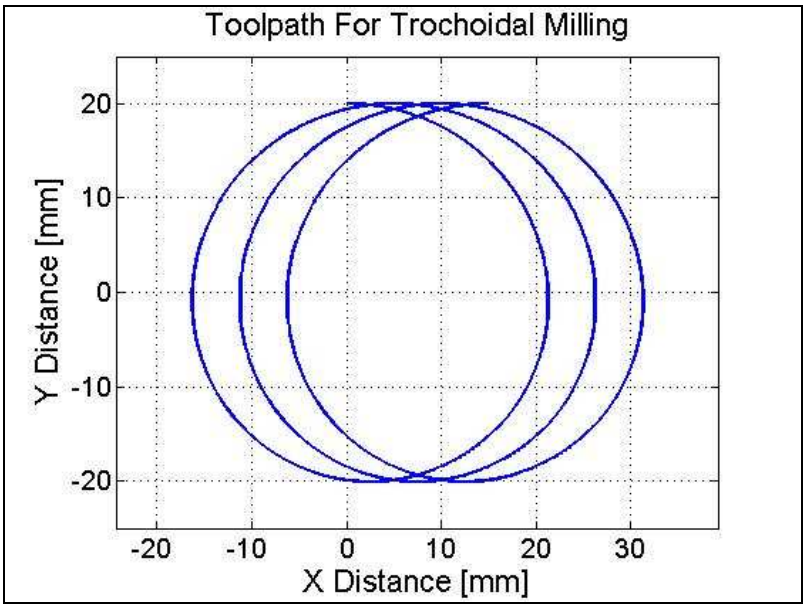

Figure 5.1: Sample trochoidal milling toolpath.

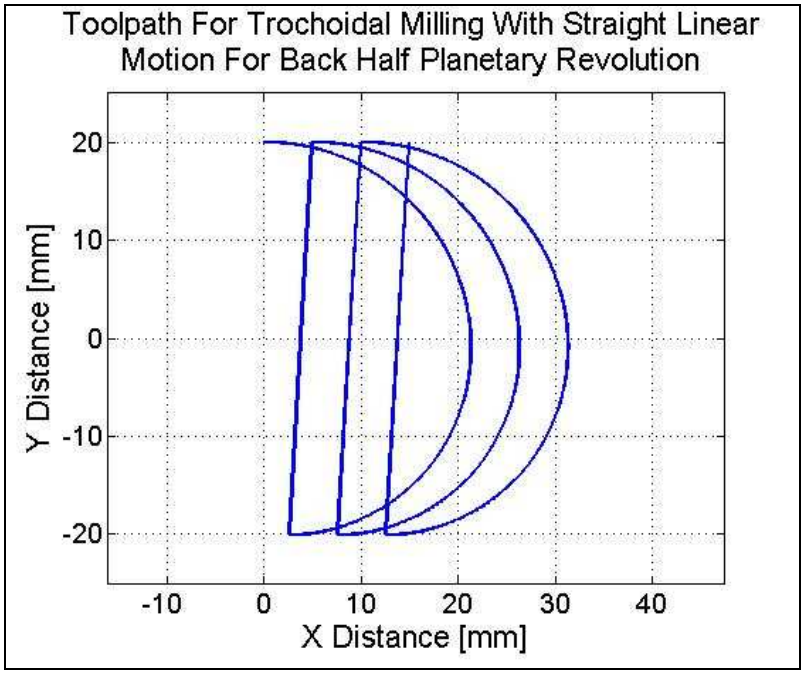

Figure 5.2: Sample trochoidal milling with straight linear motion for back half planetary revolution toolpath.

The other toolpath modification is double trochoidal milling. In double trochoidal milling, after completion of downwards half of the planetary revolution, the cutter performs an upwards planetary revolution motion. Therefore, the production cycle time of the trochoidal face milling operations is halved. The toolpath of the cutter center for double trochoidal milling is given as follows:

$$x_c = \begin{cases} R_p \sin\theta + \dfrac{c\theta}{2\pi} & if \quad 0 < \theta \le \pi \\ R_p \sin(-\theta) + \dfrac{c\theta}{2\pi} & if \quad \pi < \theta \le 2\pi \end{cases} \tag{5.2}$$

$$y_c = R_p \cos\theta$$

Figure 5.1 indicates the toolpath for double trochoidal milling with the parameters 20 mm planetary revolution radius (R_p) and 5 mm stepover between each planetary revolution.

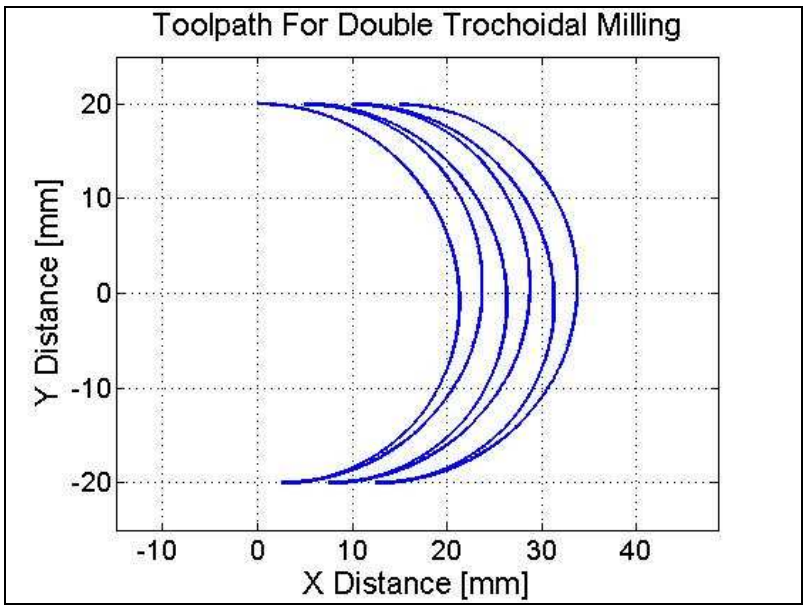

Figure 5.3: Sample double trochoidal milling toolpath.

However due to the change of direction between the half planetary revolutions and milling orientation, problems can be generated on the machined part considering tolerance errors and surface roughness. The possible problems generated by this mechanism were not examined in this study.

5.3 Force Based Feedrate Scheduling for Trochoidal Milling

Due to the competitive behavior of the production world, machining efficiency has gained a lot of importance. In commercial CAD/CAM programs, conservative constant feedrate values have been mostly used which directly restricts the machining efficiency since the generated for profile is not constant all along the toolpath and some parts of the toolpath can be machined with higher feedrates. Feedrate scheduling is an optimization process that adjusts the feedrates of the NC code of the machined part in order to cut with varying feedrates at an altered performance and efficiency. Two different strategies are used for the feedrate scheduling: material removal rate (MRR) based and force based feedrate scheduling (FFS). Previous studies result out the fact that force based one is more productive and reliable considering the generated force profiles [18].

FFS regulates the original constant feedrate according to the reference cutting force all along the toolpath. Calibration tests for TaeguTec 8 mm end mill and DIN 1.2842 steel pair yields out the fact that the average cutting forces can be expressed in terms of a linear function of the feedrate term contributed by the cutting forces and an offset contributed by the edge forces (Figures 5.4, 5.5). The average cutting forces are measured for seven different immersion conditions (Slot cutting 0° - 180°, 0° - 120°, 60° - 180°, 0° - 90°, 90° - 180°, 0° - 60°, 120° - 180°). The relation between the cutting forces and feedrate is used in force based feedrate scheduling algorithm.

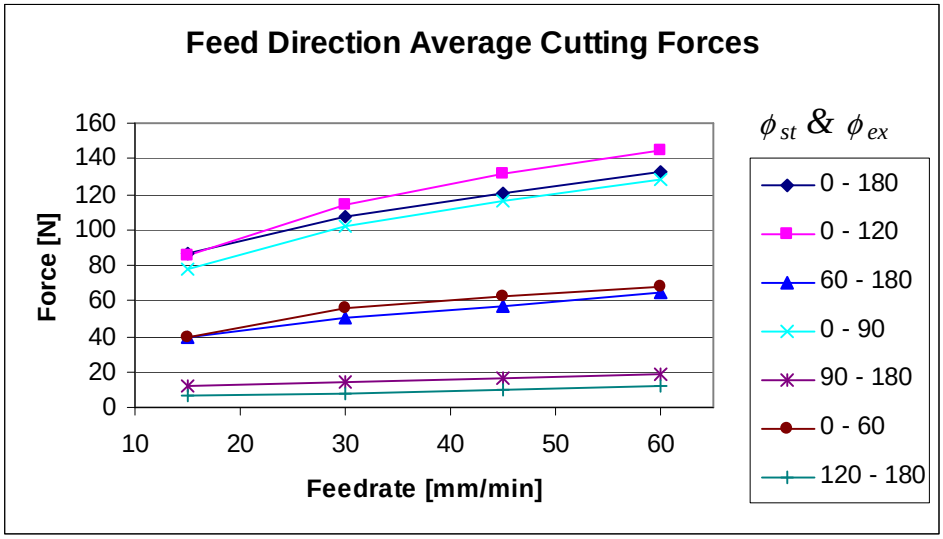

Figure 5.4: Feed direction average cutting forces for TaeguTec 8 mm end mill DIN 1.2842 steel pair.

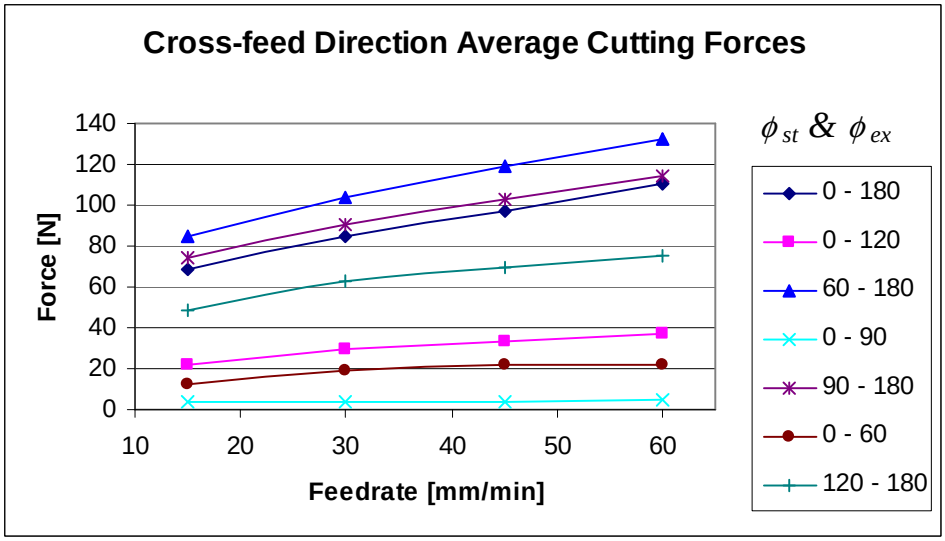

Figure 5.5: Cross-feed direction average cutting forces for TaeguTec 8 mm end mill DIN 1.2842 steel pair.

The force model introduced in chapter 3, relates the differential cutting forces in tangential, radial and axial directions to cutting coefficients times chip load plus edge coefficients times cut length (Equation 3.6). This provides to derive a linear relation depending on feedrate.

$$dF_i = A \cdot f + B \tag{5.3}$$

The model is processed to keep the resultant force at the desired constant limit level along the toolpath for the CL points; the model uses the contact region defined for each CL point. The limiting feedrate formula for the i^{th} CL point is given as follows;

$$f_{\lim,i} = (F_{\lim,i} - F_{1,i}) \cdot \frac{f_2 - f_1}{F_{2,i} - F_{1,i}} + f_1 \tag{5.4}$$

where i = 1, 2, 3,…., C and C is the total number of CL points in the toolpath, f_1 (mm/min) is the original constant feedrate for the toolpath; f_2 (mm/min) is two, three or any number times f_1 in order to obtain the linear relation for the i^{th} CL point. F_1(Newton) is the maximum resultant force value for the i^{th} CL point for f_1 feedrate value, F_2 (Newton) is the maximum resultant force value for i^{th} CL point for f_2 feedrate value, $F_{lim,i}$ is the limiting constant resultant force threshold value which the cutting forces will be under this threshold value and $f_{lim,i}$ is obtained as scheduled in (mm/min) for the i^{th} CL point.

Chapter 6

FORCE VALIDATION TESTS

6.1 Introduction

In order to validate the proposed force and engagement models, various trochoidal milling tests including the optimized ones were performed. The NURBS based toolpaths for trochoidal milling algorithms was obtained with Unigraphics NX 2.0 CAM module with a special postprocessor code generated for Koc University. Face milling area operation from the manufacturing module was used. The same experimental setup used in the calibration tests was used for the validation tests (Figures 4.1 and 4.3). The cutting conditions and results of the performed cutting tests were described in the following sections of this chapter.

The validation tests were performed for analytical and numerical engagement models and the modification algorithms for trochoidal milling.

6.2 Analytical Engagement Model Validation Test

The analytical engagement model developed for trochoidal milling is only capable of predicting the engagement for simple filled surfaces without containing any holes or bosses in it. The validations of the proposed model was carried out with simple 2 ½ axis trochoidal milling situation. For Sandvik 12 mm CoroMill Plura ISO N mill and aluminum 7039 workpiece pair, the feedrate and the spindle speed have been chosen as 240 mm/min and 600 rpm respectively corresponding to 0.2 mm/rev/tooth. The axial depth of cut was 2 mm. The radius of the planetary revolution was 14 mm and the stepover between the planetary

revolutions is 1 mm. The process was slot cutting and the dimensions of the workpiece were $b_1 = b_2 = 20$ mm. Sampling frequency was taken as 1000 Hz which corresponds to 3.6° rotation angle for the cutting conditions. The tool and cutting parameters are summarized in Table 6.1.

Table 6.1: Trochoidal milling validation tests cutting conditions.

Cutter	Sandvik 12 mm
Workpiece Material	Al 7039
Spindle Speed	600 rpm
Feedrate	240 mm/min
Axial Depth of Cut	2 mm
Radius of Planetary Revolution	14 mm
Stepover	1 mm
Workpiece Dimensions (b_1/b_2)	20/20 mm
Sampling Frequency	1000 Hz

Figure 6.1 indicates the engagement results for trochoidal milling with 12 mm end mill, 14 mm planetary revolution radius and 1 mm stepover. The start and the exit angles both start from approximately 4°. The start angle converges to 0° as the cutter retracts from the workpiece. The exit angle increases with a decreasing slope at first, reaches the maximum value approximately 40° and converges to 0° as the cutter retracts from the workpiece.

Figures 6.2 and 6.3 point out the feed, cross-feed and axial directions simulation and experimental cutting forces for a spindle and planetary revolution respectively. The simulated and the measured forces are in good correspondence with each other for both revolution periods. As the cutter has two flutes, two peaks of the cutting forces in each direction are observed in a single rotation of the cutter corresponding to 360°. Due to the small engagement regions almost 2/3 of the cutter rotation the cutter teeth do not perform cutting which help further cooling of themselves.

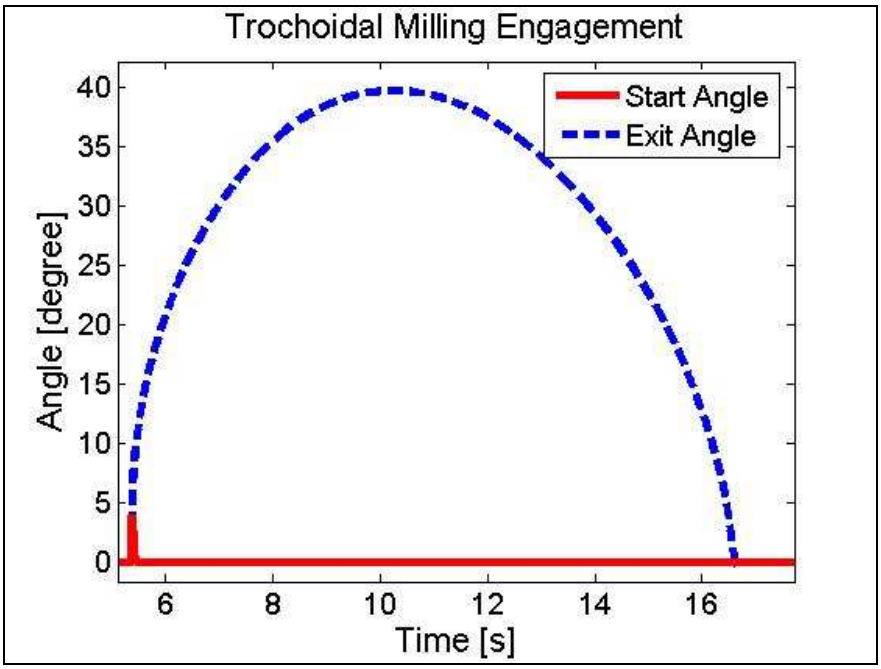

Figure 6.1: Engagement conditions.

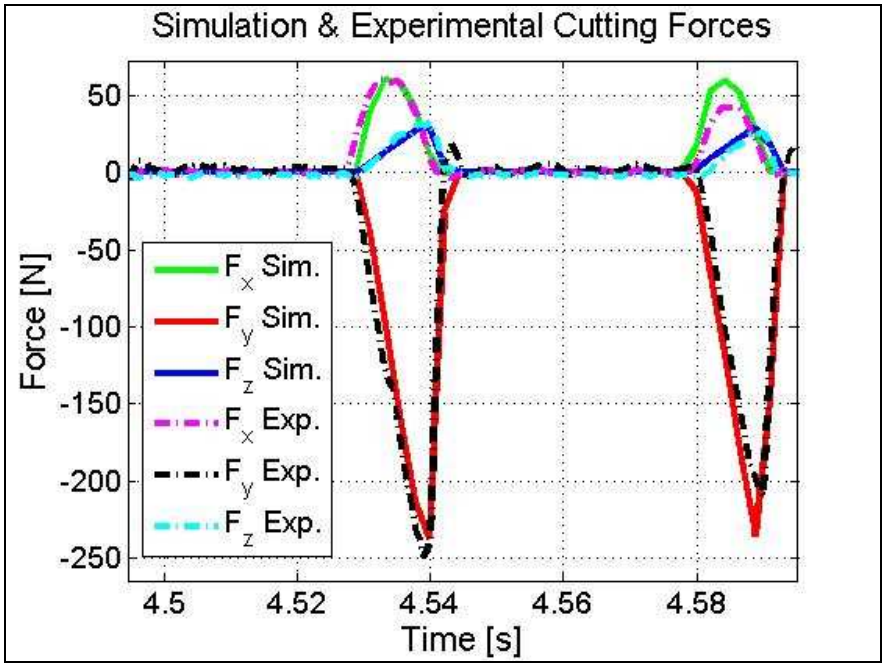

Figure 6.2: Comparison of the experimental and simulation forces for one spindle period.

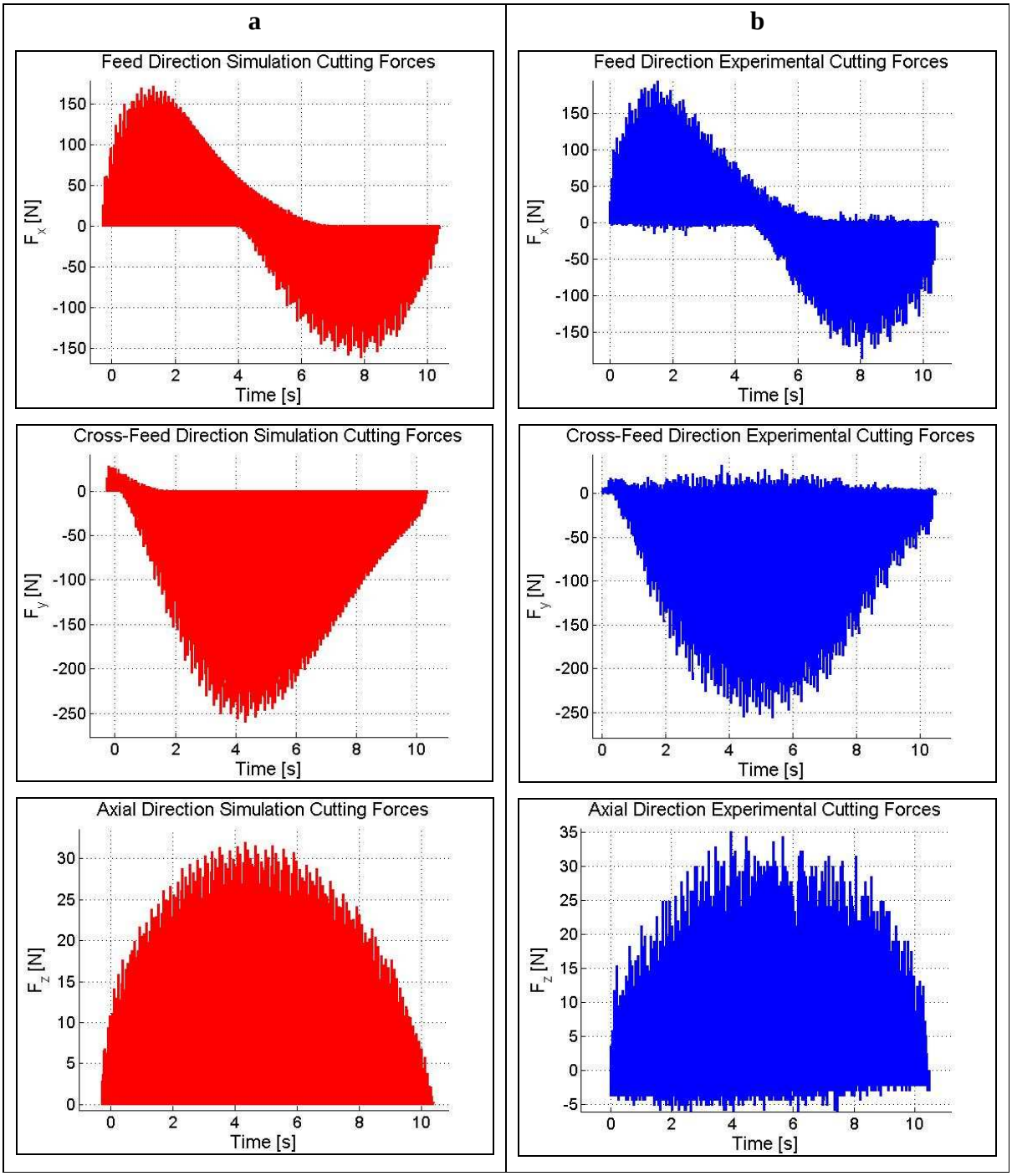

Figure 6.3: Comparison of the simulation and experimental cutting forces for one planetary revolution.

6.3 Numerical Engagement Model Validation Test

The numerical engagement model developed for trochoidal milling is capable of predicting the engagement for complex surfaces containing holes or bosses in it. The validations of the proposed model was carried out with simple 2 ½ axis trochoidal milling situation. The same cutter and workpiece material pair used in the numerical engagement model validation test were used. The cutting parameters such as spindle speed and feedrate were kept constant with the previous test. The axial depth of cut was 1 mm. The radius of the planetary revolution was 22 mm and the stepover between the planetary revolutions is 1 mm. Sampling frequency was taken as 1000 Hz which corresponds to 3.6° rotation angle for the cutting conditions. The workpiece used was the ½ scaled model of the cover of a cylinder block of Motosan one cylinder diesel engine. Figure 4-a shows the Unigraphics 3D CAD drawing of the machined workpiece with the necessary dimensions. The toolpath was created via UG NX 2.0 face milling area operation. The generated toolpath starts with smaller planetary revolution radius and it continuously increases until the steady state value. A section of the NURBS g-code file and point cloud representation of the cylinder block with the toolpath are given in Figure 4-b,c.

In Figure 6.5 complete force profile along the toolpath is shown for both simulation and experiments. The simulated and the measured forces are in good correspondence with each other. The main reason for the increase in force amplitudes at the beginning of the trochoidal milling operation is larger engagement regions due to the small planetary revolution radius. In order to emphasize the capabilities of numerical engagement model such a complex workpiece was chosen for the validation test. The holes and the cavities in the milled surface cause gaps in the generated force profiles with respect to full surface milling. Three regions consisting of half planetary revolutions were investigated with details with aim of emphasizing the quantitative and qualitative properties of numerical engagement model. Figures 6.6, 6.7 and 6.8 indicate the simulation and experimental cutting forces for

the regions I, II and III respectively. The simulated and the measured forces are in good correspondence with each other.

a

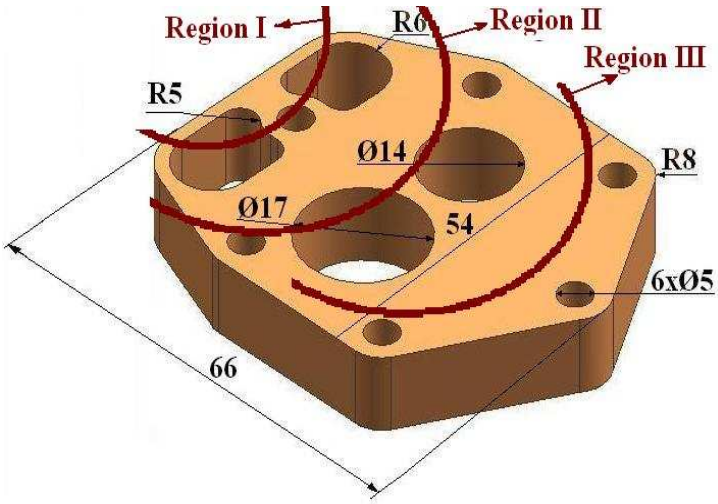

b

```
G6.2 P04 X23.374 Y35.675 Z-2. K0.0
X25.561 Y30.867 K0.0
X26.093 Y21.26 K0.0
X18.608 Y9.662 K0.0
X6.761 Y4.325 K.119
X-6.012 Y6.673 K.208
X-15.397 Y15.511 K.306
X-18.522 Y28.157 K.404
X-13.658 Y41.021 K.493
X-2.719 Y48.549 K.592
X11.373 Y48.975 K.691
X19.468 Y43.46 K.791
X22.434 Y39.104 K.88
K1.
K1.
K1.
K1.
```

c

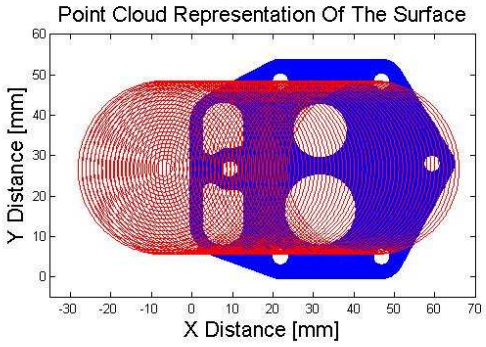

d

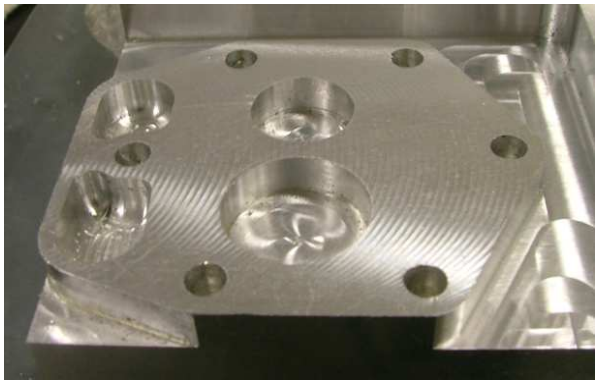

Figure 6.4: a) CAD drawing, b) A section of the NURBS g-code file, c) Point cloud representation of the cover of a cylinder block with the toolpath, d) Photograph of the machined workpiece.

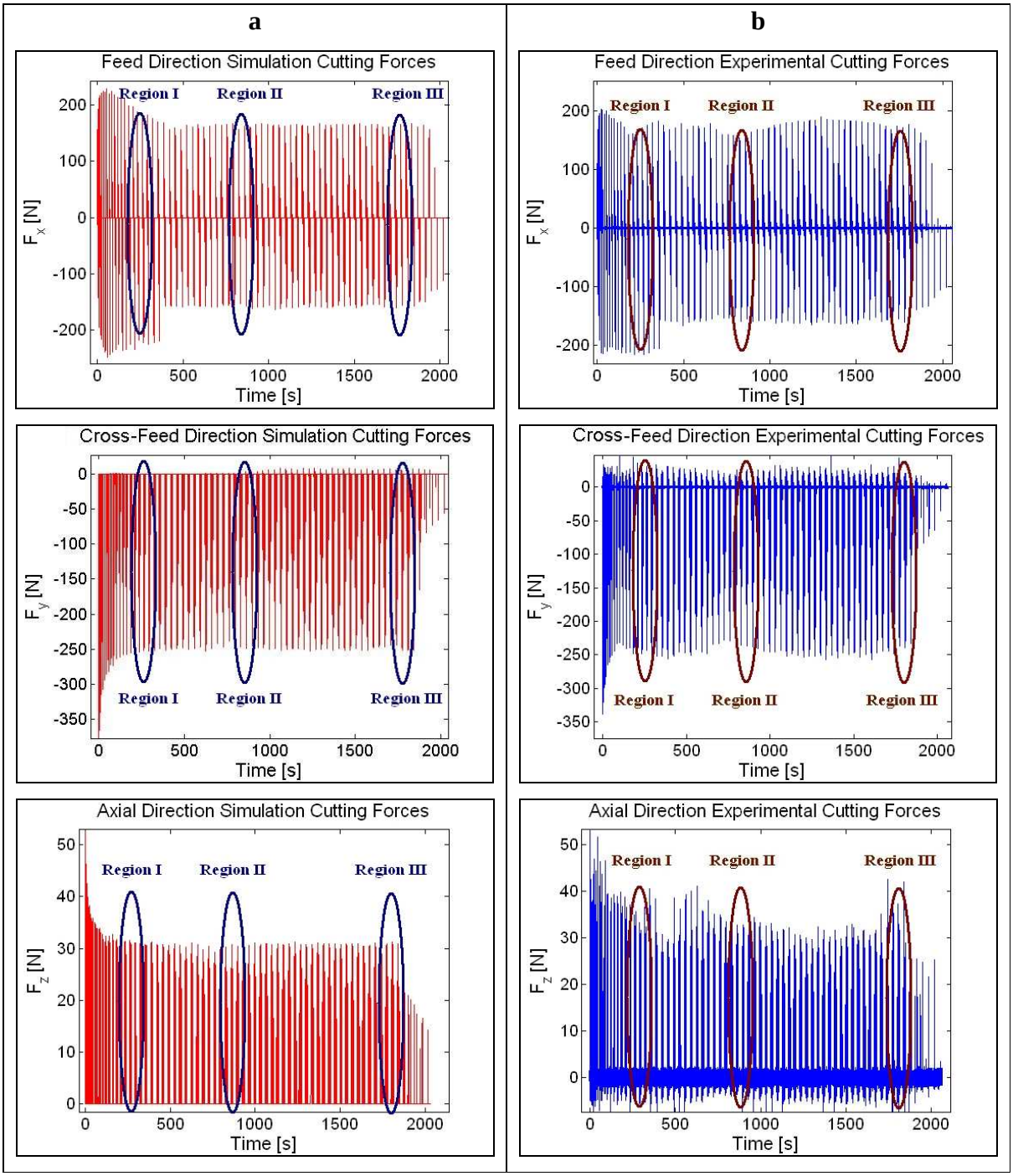

Figure 6.5: Comparison of the simulation and experimental cutting forces for full toolpath indicating the region I, II, III.

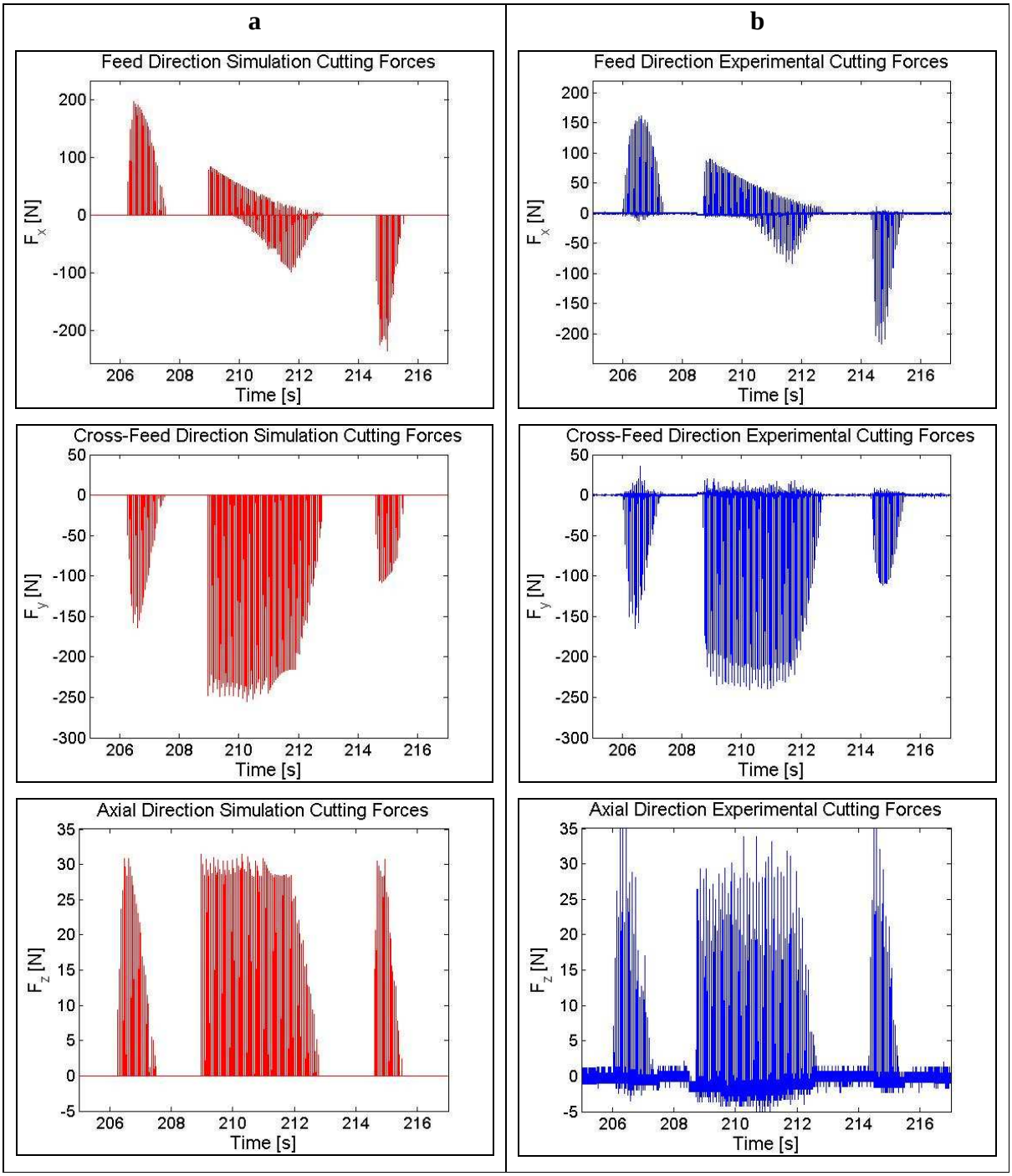

Figure 6.6: Comparison of the simulation and experimental cutting forces for one planetary in the region I.

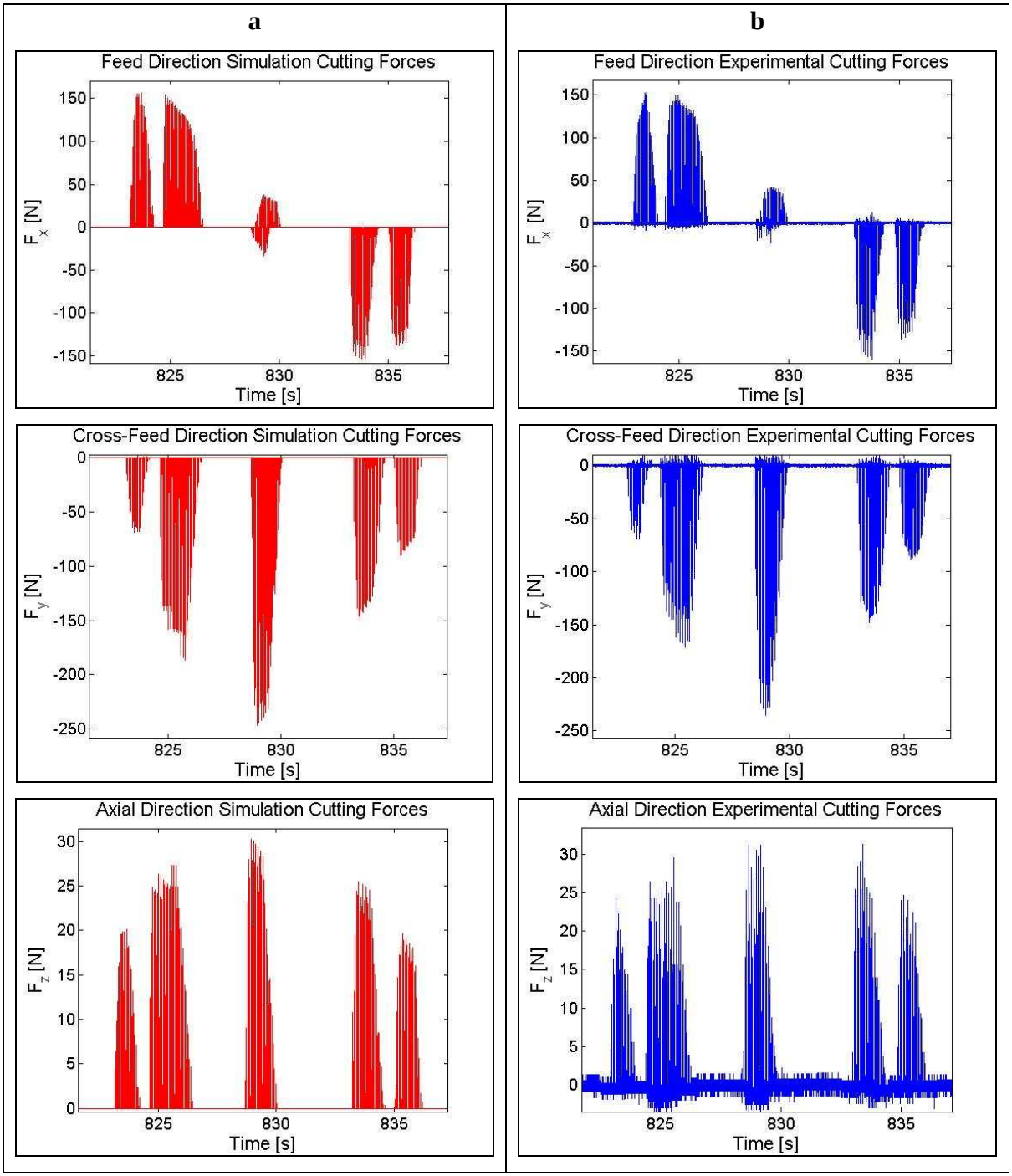

Figure 6.7: Comparison of the simulation and experimental cutting forces for one planetary in the region II.

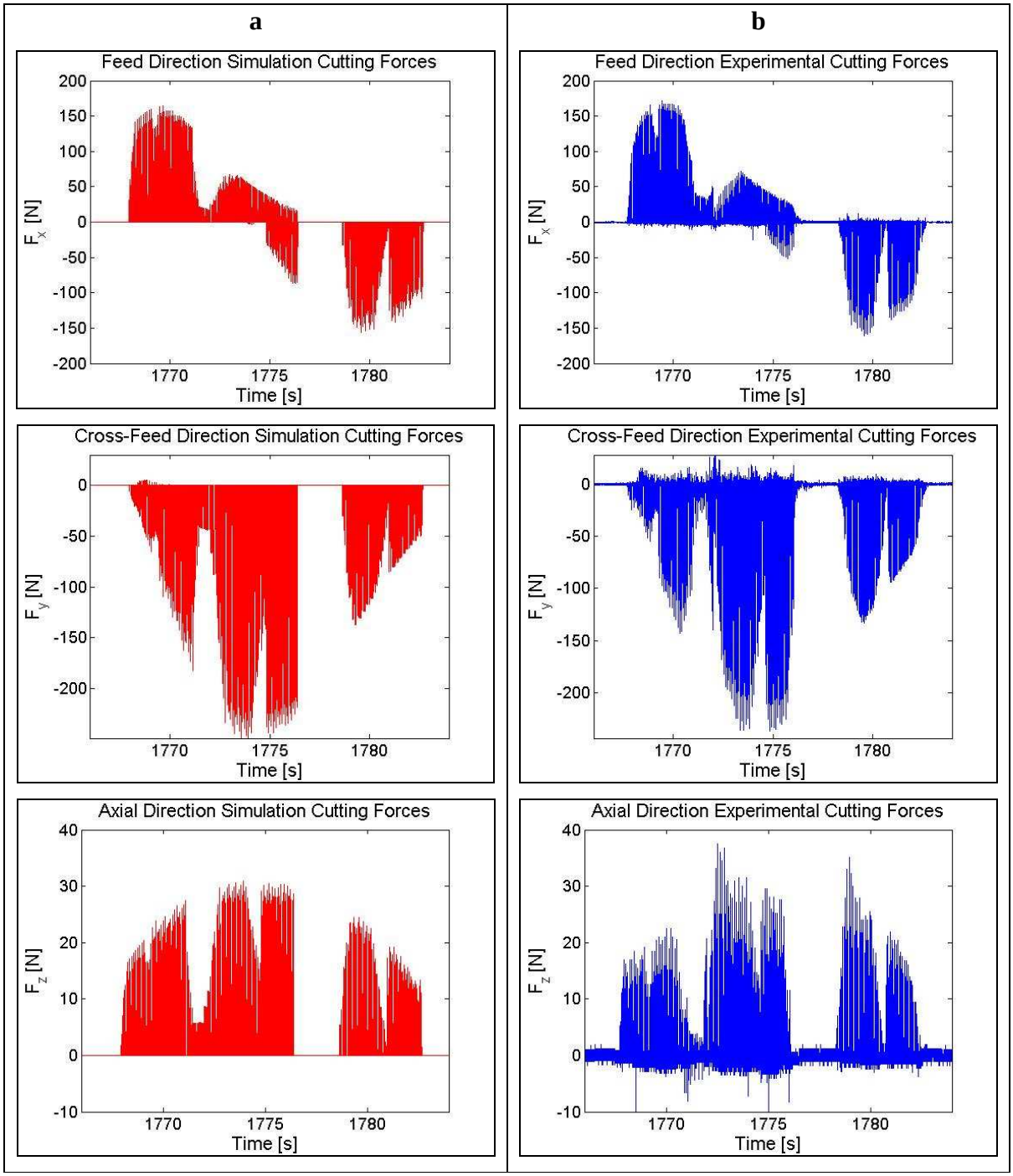

Figure 6.8: Comparison of the simulation and experimental cutting forces for one planetary in the region III.

6.4 Toolpath Modification Algorithms Validation Tests

Validation tests result out that due to the trochoidal toolpath of the cutter machining cycle time increases in a considerable amount depending on the radius of the planetary revolution and the stepover value between the planetary revolutions. Previous chapter introduced the toolpath modification algorithms for trochoidal milling operation for the maximization process of the machining efficiency. In order to emphasize the effects of toolpath modification algorithms, Al 7039 square prism blocks with dimensions 36 x 36 x 2 mm were trochoidal milled with Sandvik 12 mm end mill. The cutting parameters such as spindle speed and feedrate were kept constant with the previous tests. The axial depth of cut was 2 mm. The radius of the planetary revolution was 12 mm and the stepover between the planetary revolutions is 1 mm. Experimental measurements were carried out at 1000 Hz sampling frequency.

First of all a block was simple trochoidal milled. Figure 6.9 indicates the toolpath and the boundaries of the workpiece. In Figure 6.11 comparison of simulation and experimental cutting forces along the full toolpath is shown. The simulated and the measured forces are in good correspondence with each other. Experimentally collected time data from the DAQ setup states the total machining time is 908.6 s for trochoidal milling operation.

The first toolpath modification algorithm is trochoidal toolpath with straight linear motion at the back half of planetary revolution in feed direction. This toolpath not only shortens the machining time but also the generated forces during trochoidal milling are kept unchanged. Toolpath modification algorithm is employed during the interval that the cutter does not perform cutting. Figure 6.10 presents the modified toolpath algorithm for trochoidal milling. Figure 6.12 indicates comparison of the simulation and experimental cutting forces along the full toolpath. The generated forces are kept unchanged with the original trochoidal milling equation. Experimentally collected time data states the total machining time is 749.2 s for the modified trochoidal milling operation.

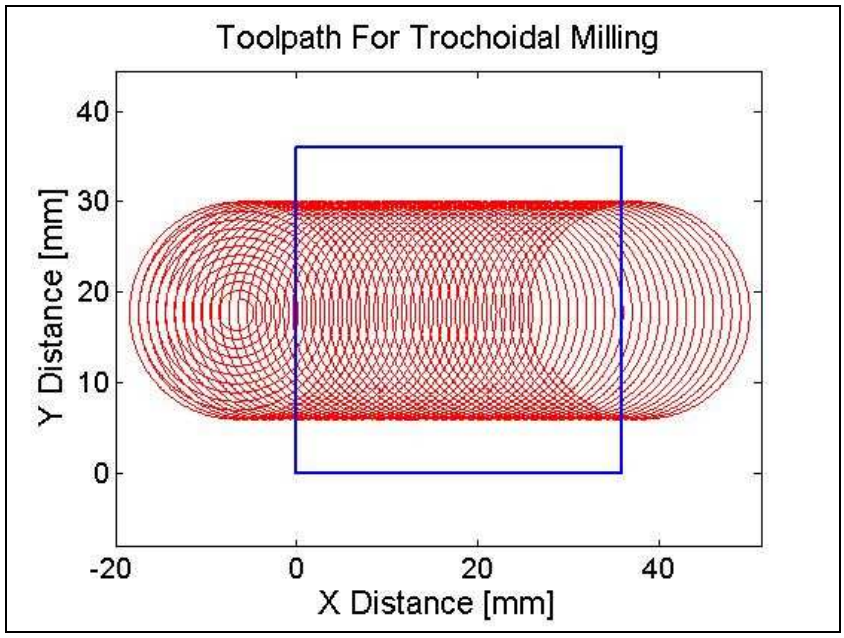

Figure 6.9: Toolpath for trochoidal milling of 36 x 36 x 2 aluminum block.

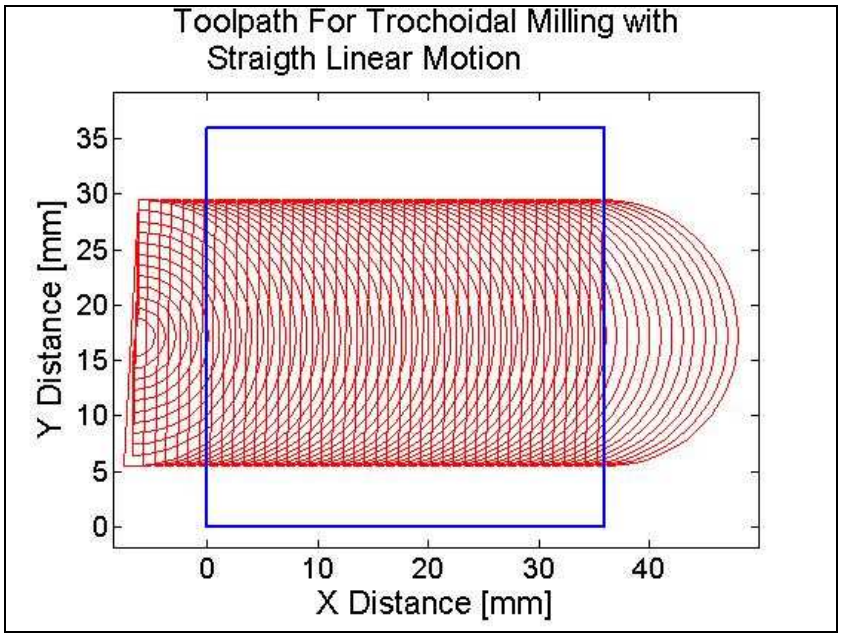

Figure 6.10: Toolpath for trochoidal milling with straight linear motion at the back half of planetary revolution in feed direction of 36 x 36 x 2 aluminum block.

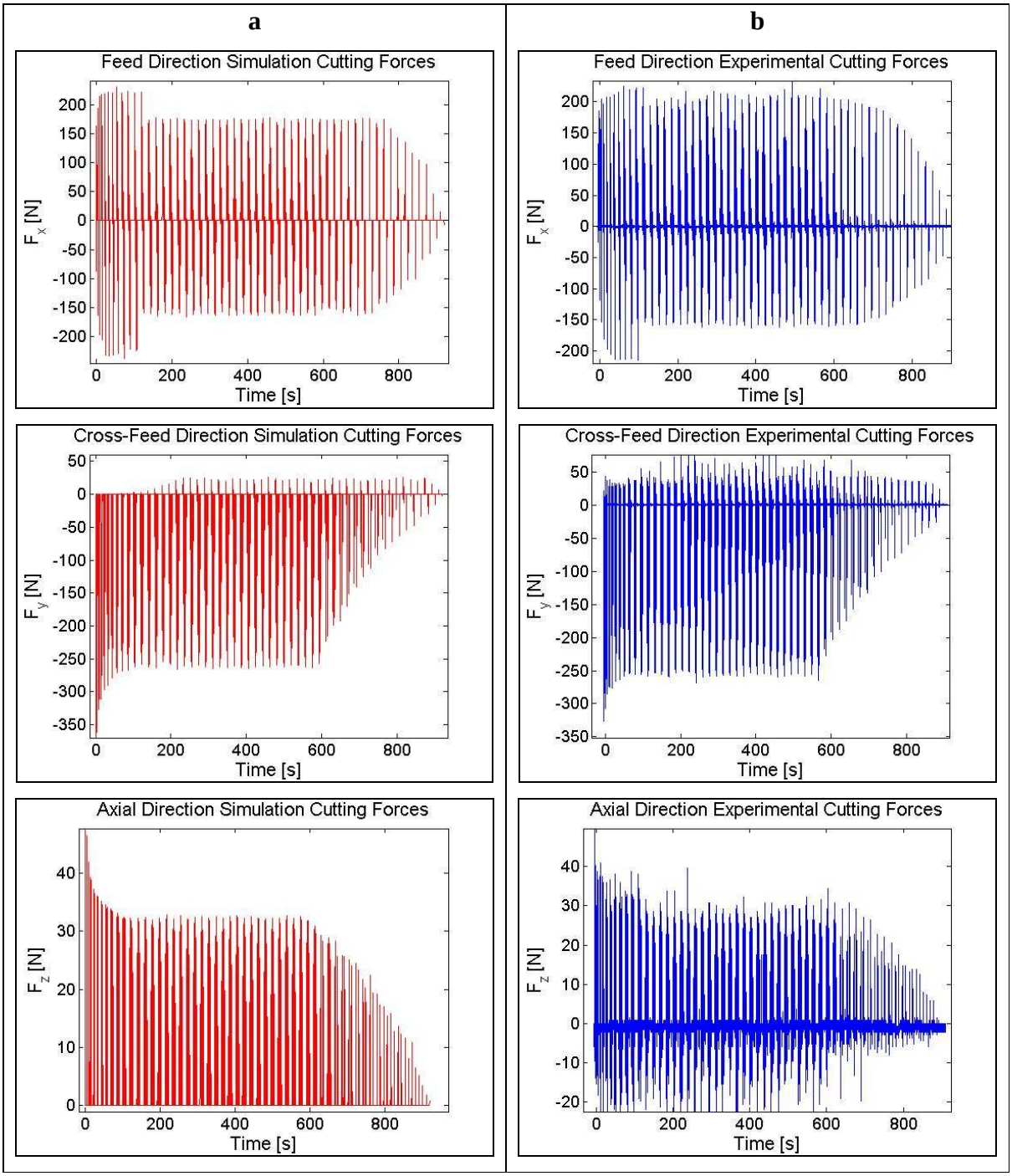

Figure 6.11: Comparison of the simulation and experimental cutting forces for trochoidal milling.

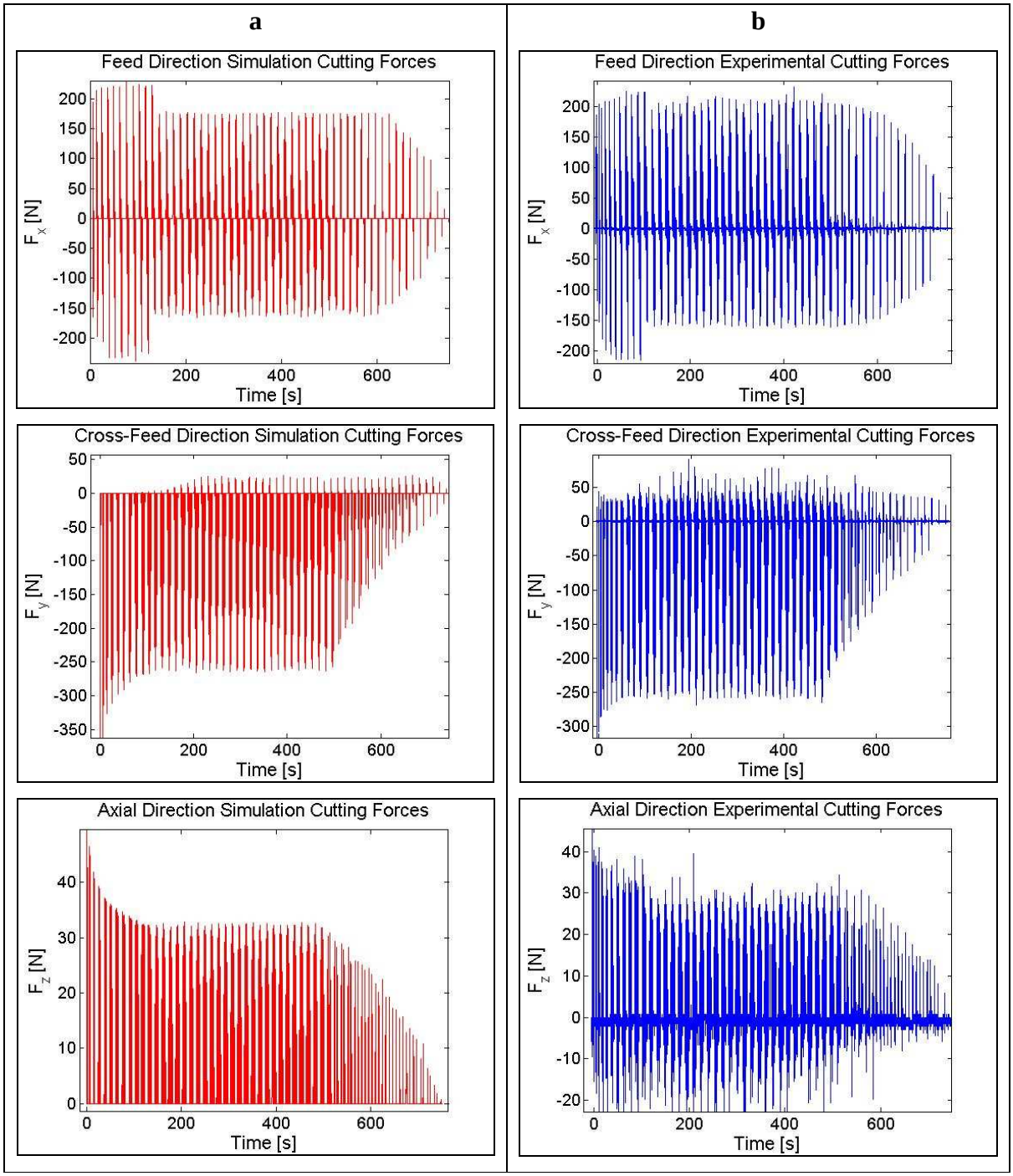

Figure 6.12: Comparison of the simulation and experimental cutting forces for trochoidal milling with straight linear motion at the back half of planetary revolution in feed direction.

The second toolpath modification algorithm is double trochoidal milling. The production cycle time of the trochoidal face milling operations is halved with this approach due to the fact that the cutter is always in contact with the workpiece performing cutting. Figure 6.13 indicates the toolpath for double trochoidal milling. Although double trochoidal milling shortens machining time, there is a drastic direction change at the end of each path.

In Figure 6.14 comparison of the simulation and experimental cutting force along the full toolpath is shown. The simulation results show good correspondence with the experimental results. Figure 6.15 presents the simulation and experimental cutting forces for two half planetary revolutions: one downwards and one upwards. Due to the reason that milling orientation changes within the downwards and upwards motions there is a slight increase in the maximum force magnitude at the experimental measurements. Experimentally collected time data states the total machining time is 451 s for the modified trochoidal milling operation.

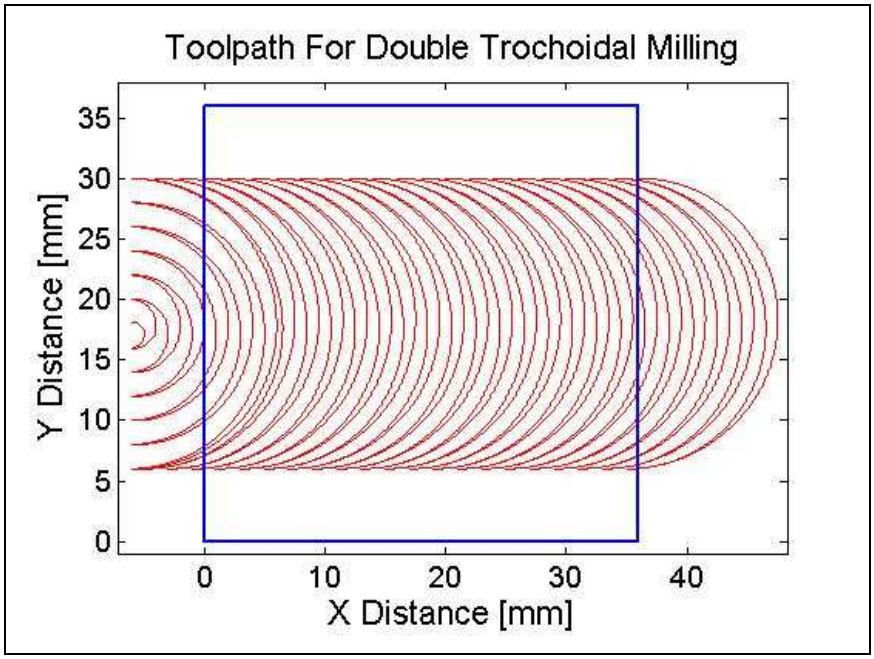

Figure 6.13: Toolpath for double trochoidal milling of 36 x 36 x 2 aluminum block.

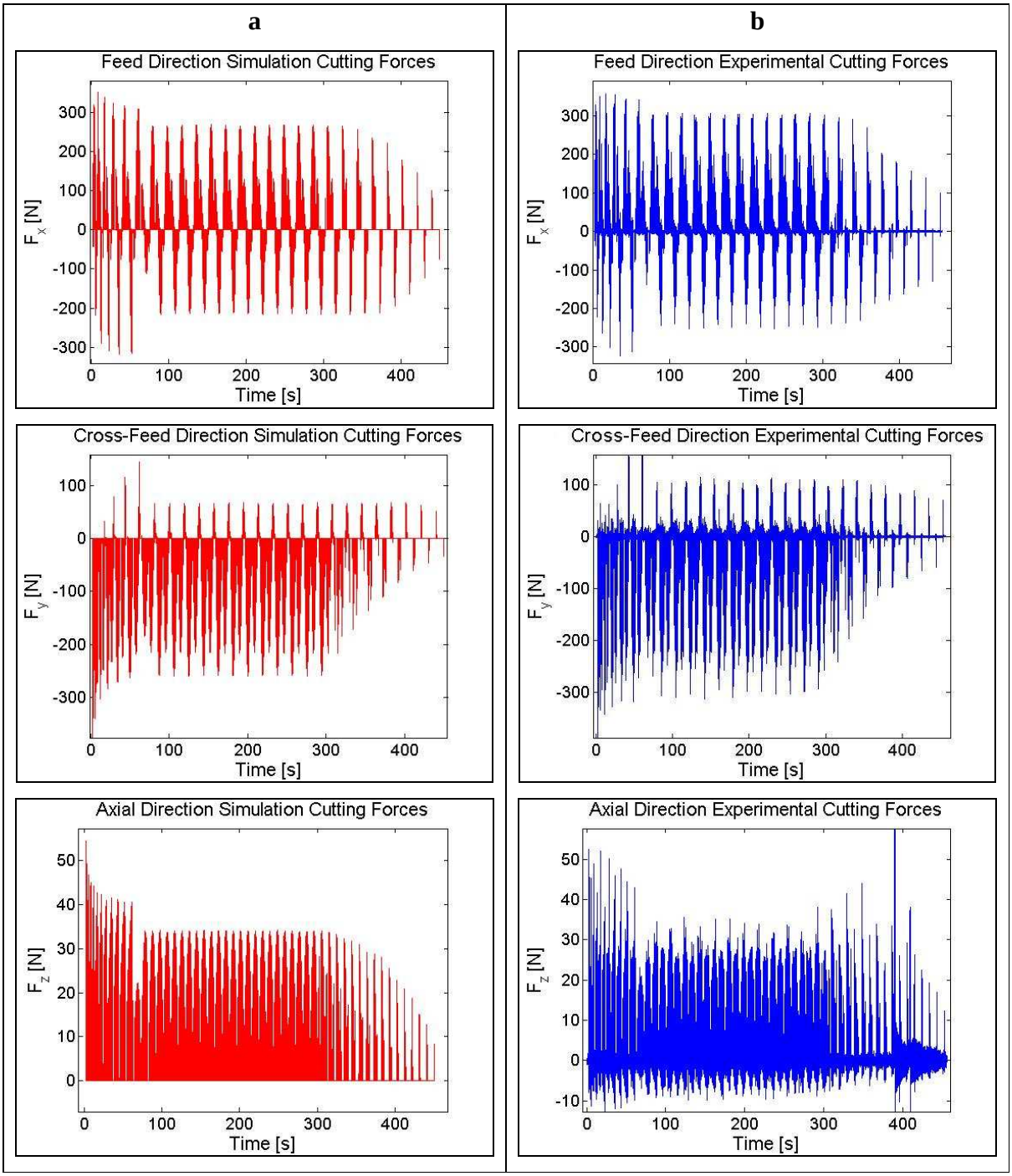

Figure 6.14: Comparison of the simulation and experimental cutting forces for double trochoidal milling along the full toolpath.

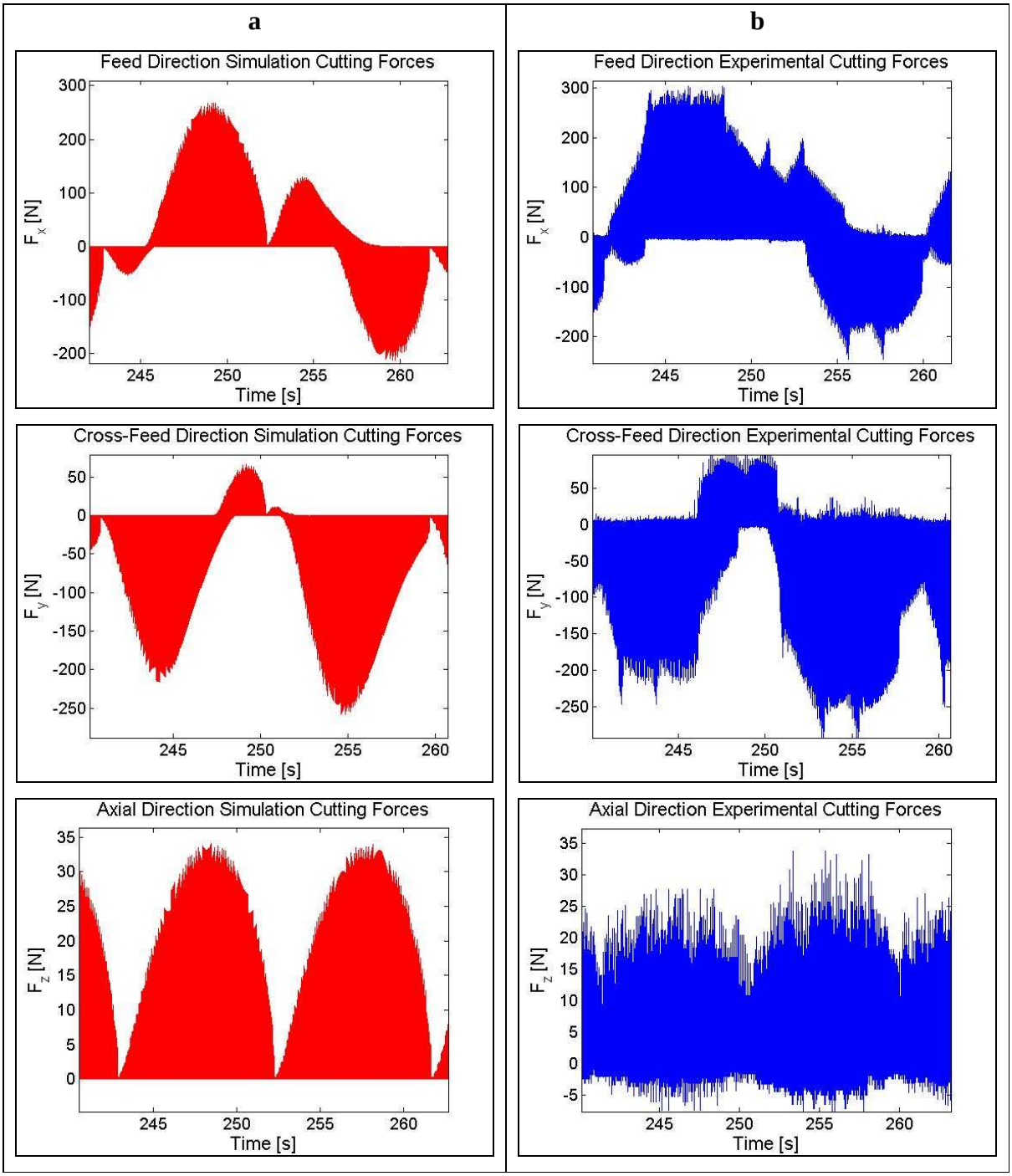

Figure 6.15: Comparison of the simulation and experimental cutting forces for double trochoidal milling for two half planetary revolutions.

Further optimization of the toolpath modification algorithms is carried out with force based feedrate scheduling. In order to validate the FFS algorithm experimental tests were performed with the same experimental setup on the double trochoidal milling operation. The resultant force in the original operation was about 275 N. The feedrate scheduling algorithm was employed in order to achieve a constant maximum force profile at a level of 275 N. The original feedrate value was 240 mm/min. For safety reasons the maximum feedrate value is restricted with 500 mm/min. Figure 6.16 indicates the comparison of the constant and scheduled feedrates and the first lines of the NURBS g-code sections. The experimental measurements and the simulation results for full force profile along the toolpath and two half planetary revolutions are given in Figure 6.17 and 6.18 respectively. The simulation results are in good agreement with the experimental measurements both quantitatively and qualitatively. Experimentally collected time data states the total machining time is 323 s for the double trochoidal milling operation.

a

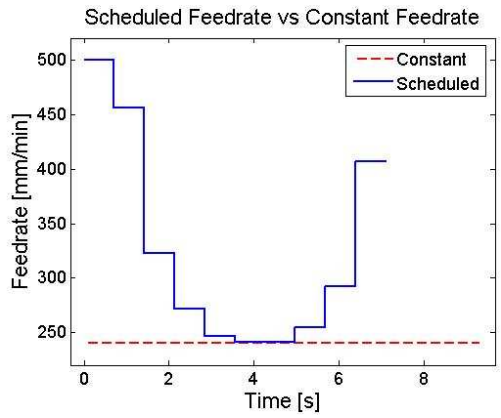

b

```
G6.2 P04 X11.000 Y 6.000 Z-2.0 K0.0 F500
G6.2 P04 X14.808 Y 6.587 Z-2.0 K0.0 F456
G6.2 P04 X18.253 Y 8.292 Z-2.0 K0.0 F323
G6.2 P04 X21.008 Y10.947 Z-2.0 K0.0 F272
G6.2 P04 X22.813 Y14.292 Z-2.0 K0.0 F247
G6.2 P04 X23.500 Y18.000 Z-2.0 K0.0 F241
G6.2 P04 X23.013 Y21.708 Z-2.0 K0.0 F241
G6.2 P04 X21.408 Y25.053 Z-2.0 K0.0 F255
G6.2 P04 X18.853 Y27.708 Z-2.0 K0.0 F292
G6.2 P04 X15.608 Y29.413 Z-2.0 K0.0 F407
G6.2 P04 X12.000 Y30.000 Z-2.0 K0.0 F500
```

Figure 6.16: a) Comparison of the scheduled and constant feedrate, b) A section of the FFS NURBS g-code file.

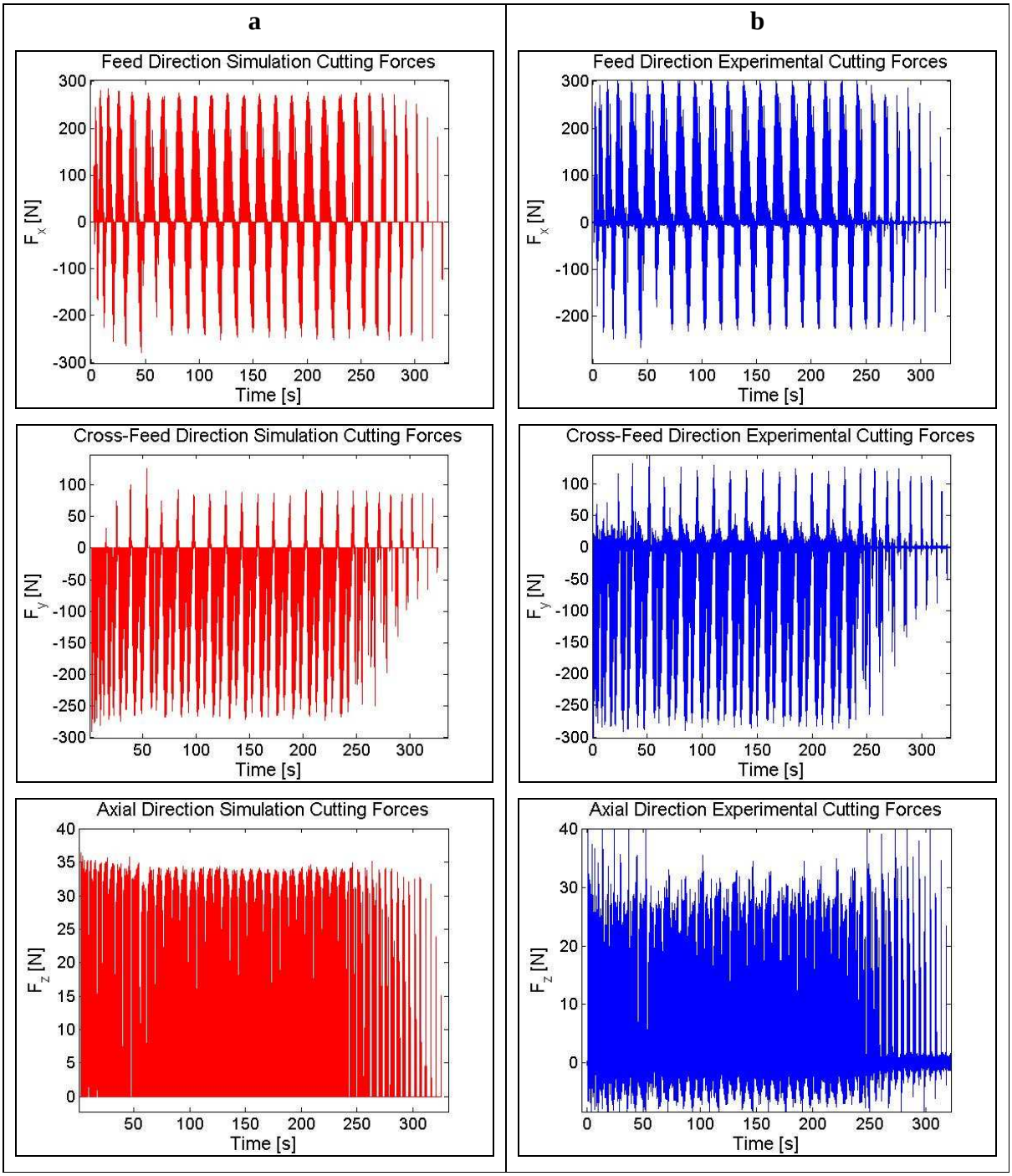

Figure 6.17: Comparison of the simulation and experimental cutting forces for FFS double trochoidal milling along the full toolpath.

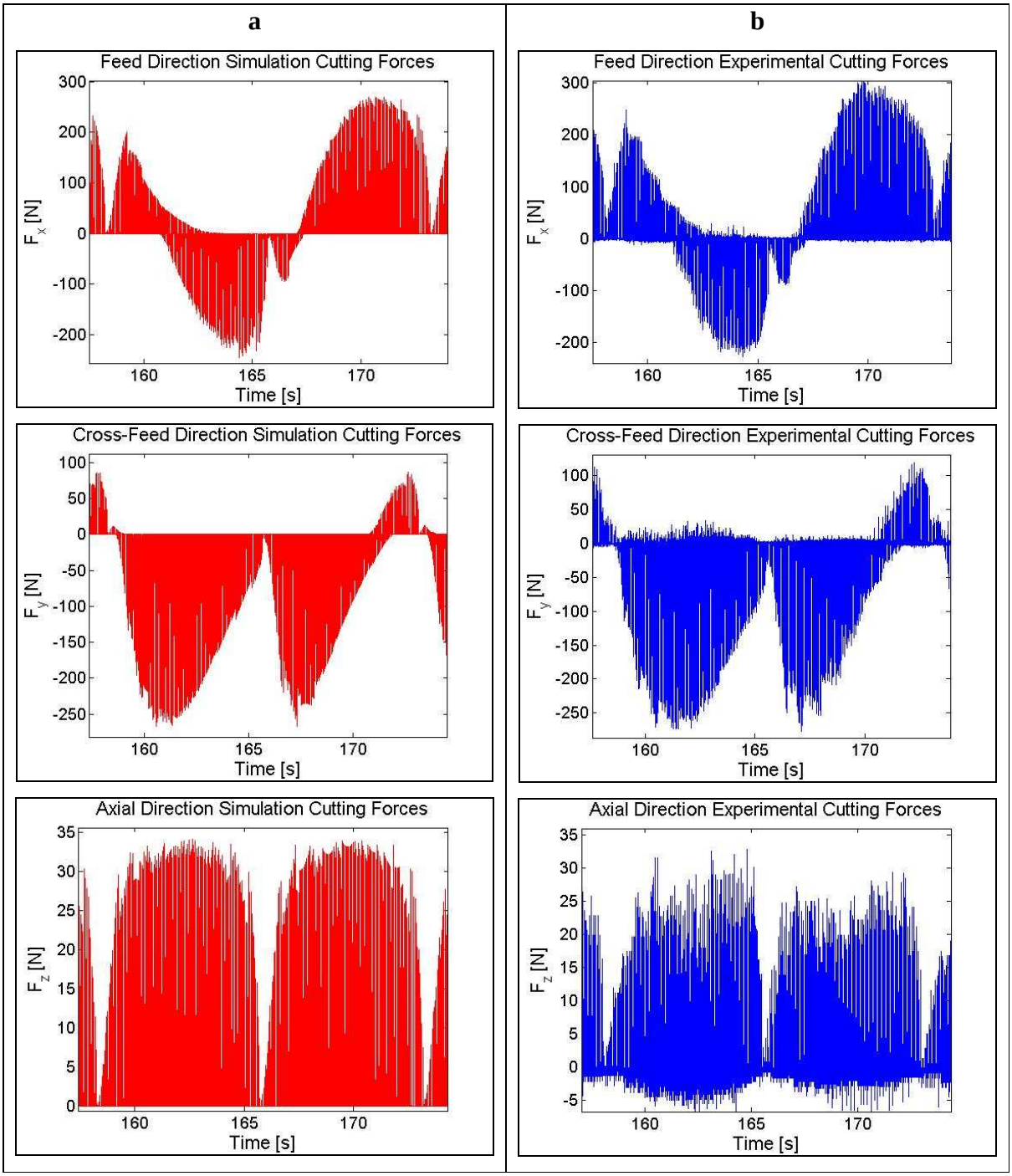

Figure 6.18: Comparison of the simulation and experimental cutting forces for FFS double trochoidal milling for two half planetary revolutions.

Figure 6.19 shows the resultant cutting forces for constant feedrate and FFS double trochoidal milling for a half planetary revolution period. It can be easily noticed that after implementation of FFS algorithm the resultant force profile has become smoother. The resultant cutting forces were kept around 275 N. The decrease at the ends of the revolutions is due to the feedrate limitation at the level 500 mm/min for safety reasons. Half planetary revolution takes 9.31 and 7.41 s for original double trochoidal milling and FFS double trochoidal milling respectively.

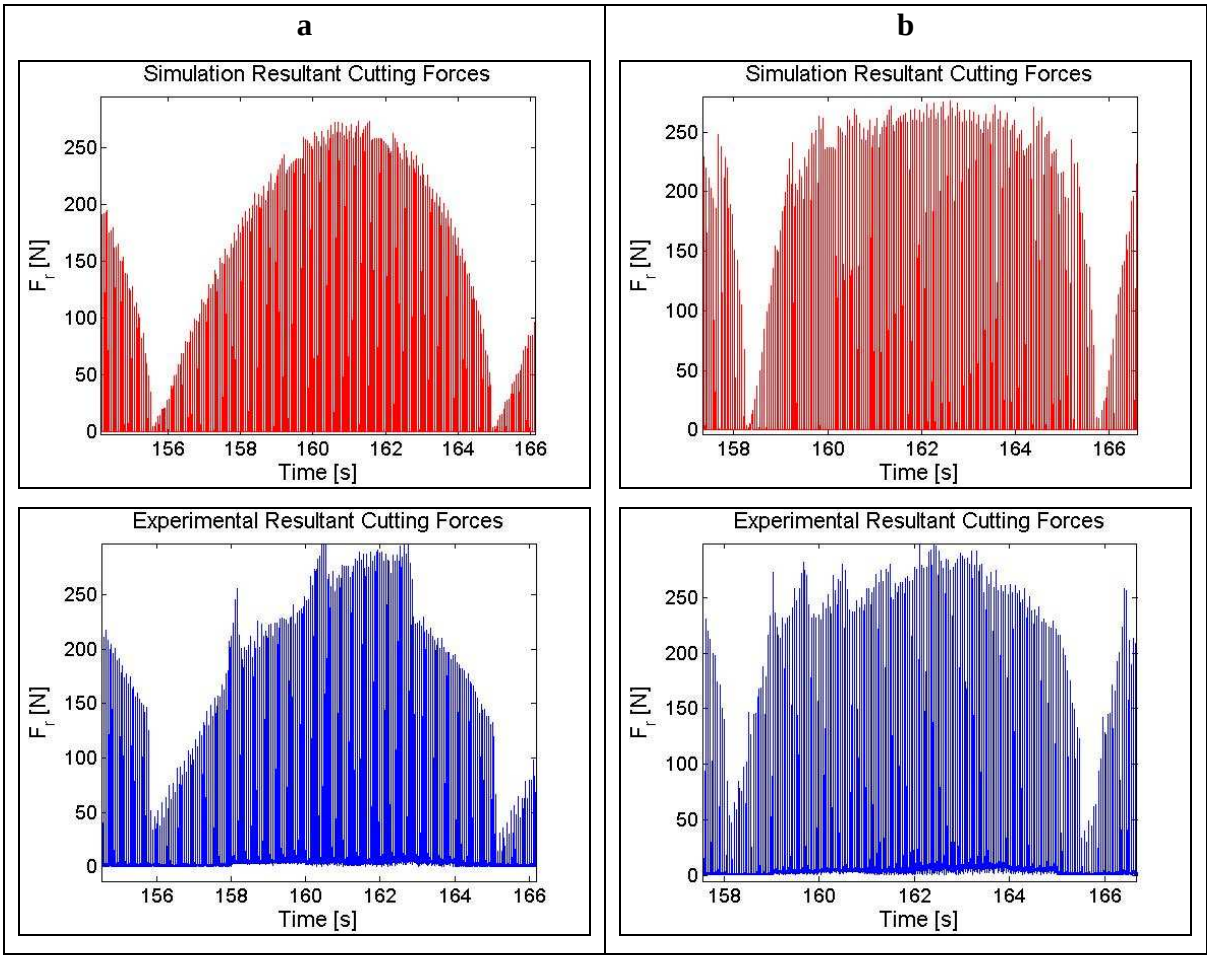

Figure 6.19: Half planetary revolution a) Simulation and experimental resultant cutting forces for double trochoidal milling b) FFS double trochoidal milling.

6.5 Conclusion

This chapter contains the experimental validation of the proposed engagement and force models. Various tests were performed for validation. First of all analytical engagement model was validated for simple trochoidal milling. Afterwards simulations of the numerical engagement model of trochoidal milling of the cover of a cylinder block of one-cylinder diesel engine were compared with experimental measurements.

The next section contains the validation tests of toolpath modification algorithms for trochoidal milling. The first toolpath modification algorithm was trochoidal milling with straight linear motion for back half planetary revolution. Afterward double trochoidal milling mechanism validation tests were carried out. Moreover, simulation of force based feedrate scheduling (FFS) algorithm applied over double trochoidal milling were validated with experimental tests. In all the phases of the study the predicted simulation and measured experimental cutting forces are in good agreement. Table 6.2 summarizes the improvements in cycle time within the toolpath modification algorithms. FFS double trochoidal milling algorithm enables 64.4 % reduction in cycle time compared with original trochoidal milling operation.

Table 6.2: Comparison of cycle time for various trochoidal milling algorithms.

Algorithm Used	**Cycle Time [s]**	**Reduction in Cycle Time**
Trochoidal Milling	908.6	0 %
Trochoidal Milling with Straight Linear Motion	753.6	17 %
Double Trochoidal Milling	451	50.4 %
FFS Double Trochoidal Milling	323	64.4 %

Chapter 7

COMPARING WEAR IN LINEAR AND TROCHOIDAL MILLING WITH SURFACE ROUGHNESS AND CUTTING FORCE ASPECTS

7.1 Introduction

As the competition in world marketing gets harder within product life cycles gets shorter. A product that had a life cycle of three years five to ten years ago might have a life cycle of just one year today [1]. Therefore the main motivation in die and mold industry is to increase productivity and reduce production costs and cycles. In order to increase productivity several strategies are used. One of them is applying different toolpaths in machining operations. Commercial CAM programs use different toolpath strategies such as zigzag, peripheral, circular and trochoidal paths. The previous chapters enclose the modeling of engagement domain for trochoidal milling force predictions.

The present chapter includes comparison of trochoidal and linear milling upon usage characteristics. The comparison issues consist of three subsections: wear characteristics comparison, cutting forces comparison and surface roughness comparison.

7.2 Tool Wear

Cutting tools are confronted to drastic conditions during machining processes. The extremely severe friction conditions due to large amplitude cutting forces and high temperatures causes tool wear. The gradual loss of tool material during cutting causes tool

wear. Cutting tools are useful as long as surface finish and dimensional accuracy are kept in the specified tolerances. Extreme tool wear results in tool reach its life limit, and tool change is unavoidable.

Tool wear mainly occurs not only at rake face due to the high contact stress between tool rake and chip face; but also at the clearance face due to the friction between the flank and machined surface. Excessive wear or mechanical and thermal overload may cause chipping or even tool breakage.

Tool wear phenomena relies on several mechanisms which can be listed as abrasion, adhesion, diffusion, chemical and fatigue wear [2]. Abrasion wear can be defined as tearing of small particles from a soft material with a harder material. On the other hand, softer material also removes particles from harder material with a slower rate. Adhesion wear occurs in the presence of sliding of two smooth surfaces over each other and fragments of softer material are pulled off and adhere to the harder one at localized contact areas. Adhesion wear results in built-up edge where the softer material of the chip adheres to the tool. At highly elevated temperatures, the atoms with higher concentration at one material (tool or chip) diffuse to the other one where the concentration is lower resulting in diffusion wear. Moreover, high temperature and the presence of air (O_2) cause the formation of new molecules at the tool chip contact face. Fatigue wear occurs during repeated stress that builds up and ebbs. Surface crack formation results in breakup of the surface.

Tool wear generally occurs at the contact surfaces between the tool, chip and the work material. There are two prevalent wear mechanisms: crater wear and flank wear. Crater wear forms at the contact face between the tool and chip (rake face of the tool). Due to the chip flowing across the rake face under heavy loads, severe friction conditions and high temperatures occurs. Under these circumstances a crater shape wear pattern is formed behind the cutting edge. The crater wear affects the cutting mechanism not only by increasing the rake angle thus lowering the cutting but also weakens the strength of the cutting edge enabling any probable breakage. Flank wear occurs on the clearance face of the tool in the

presence of the friction between this face and the machined workpiece surface. Abrasion and adhesion wear mechanism takes place either tool particles adhere to workpiece surface and sheared off or hard tool and workpiece particles tear off tool material. Nose and notch wear and edge chipping occur due to adhesion and weaken the cutting edge.

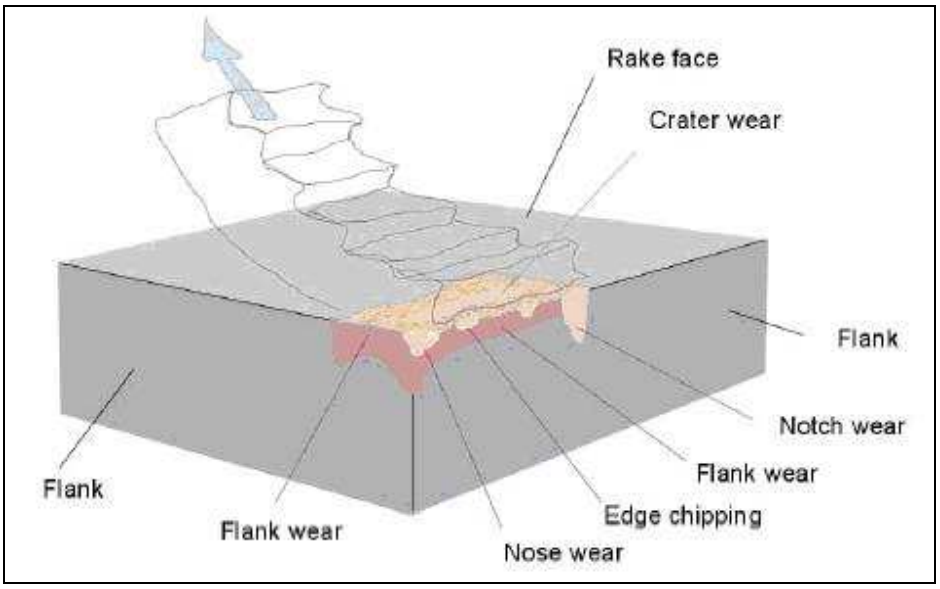

Figure 7.1: Tool wear types [35].

7.2.1 Tool Wear Measurement Setup

Tool wear on the rake and clearance faces of the cutting tools were observed using Nikon Eclipse LV100D microscope with 5x magnification. Capturing of the images were carried out with PixeLINK megapixel firewire digital camera (Model No: PL-A662) and "PixeLINK Capture SE" software. Two types of wear were observed on the investigated surfaces. These were chipping and flank wear on both clearance and flank surfaces. Maximum chipping and wear lengths perpendicular to the cutting edge were measured for linear and trochoidal milling situations.

Figure 7.2: Experimental setup for tool wear measurements [36].

7.3 Surface Roughness

The performance of the machining operation can be classified taking into consideration many parameters such as form and shape tolerances, surface roughness and residual stresses. Surface roughness is one of the most important requirements in machining operations since micro cavities on the surface assist further cracking and complete part failure. During end milling operation various parameters related with tool, workpiece and environment affect surface roughness. Related to tool geometry such as nose radius, flank width, runout and wear; to the workpiece material, hardness and machinebility and finally related to cutting conditions including feedrate, cutting speed, axial and radial depth of cut and cutting fluid determine the surface roughness.

7.3.1 Surface Roughness Measurement Parameters

This section gives the definitions (calculation methods) of the roughness parameters used along the section.

- *Arithmetic mean deviation of the profile, R_a*

R_a is the arithmetic mean of the absolute values of the profile deviations (Y_i) from the mean line.

$$R_a = \frac{1}{N}\sum_{i=1}^{N} Y_i \tag{7.1}$$

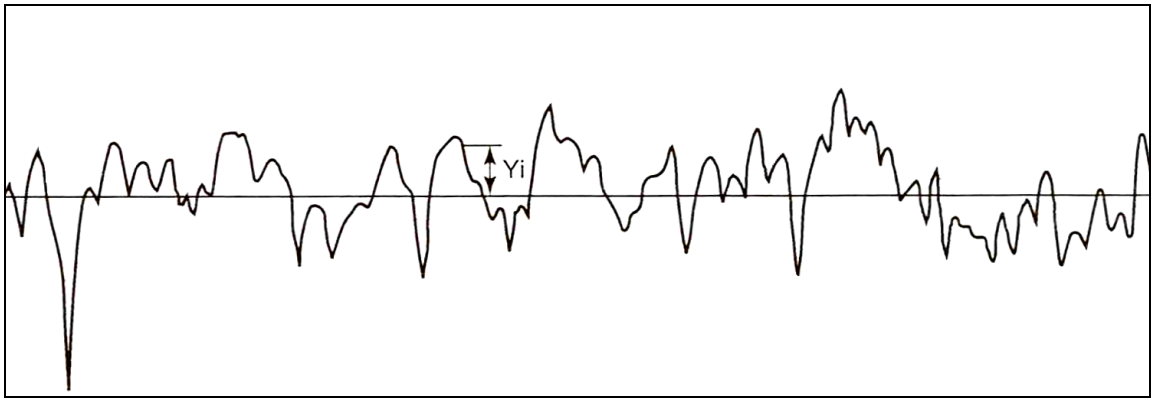

Figure 7.3: Surface roughness profile and mean value line [37].

- *Root-mean-square deviation of the profile, R_q*

R_q is the square root of the arithmetic mean of the squares of profile deviations (Y_i) from the mean line.

$$R_q = \left(\frac{1}{N}\sum_{i=1}^{N} Y_i^2\right)^{1/2} \tag{7.2}$$

- *Ten-point height of irregularities, R_z*

R_z is the sum of the mean height of the five highest profile peaks and the mean depth of five deepest profile valleys measured from the mean line.

$$R_z = \frac{1}{5}\sum_{i=1}^{5} Y_{pi} + \frac{1}{5}\sum_{i=1}^{5} Y_{vi} \tag{7.3}$$

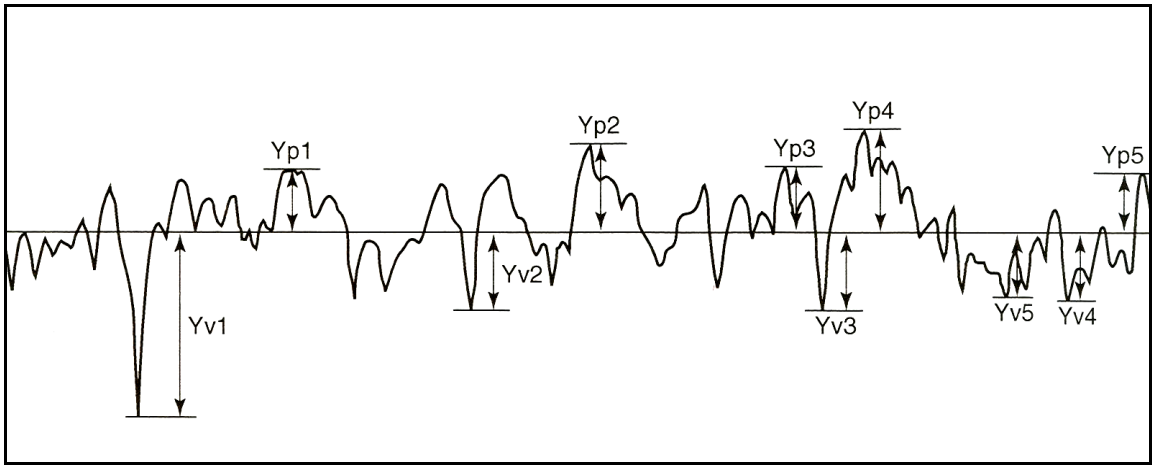

Figure 7.4: Surface roughness profile and mean value line for R_z method [37].

7.3.2 Surface Roughness Measurement Setup

Surface roughness measurements were carried on with a Mitutoyo SJ-301 surface roughness tester. The measurement probe was traveled an evaluation length of 2.5mm with 0.8 inch/second traverse speed. 6 measurements each in the feed and cross-feed directions were performed for each pass and the mean values were recorded.

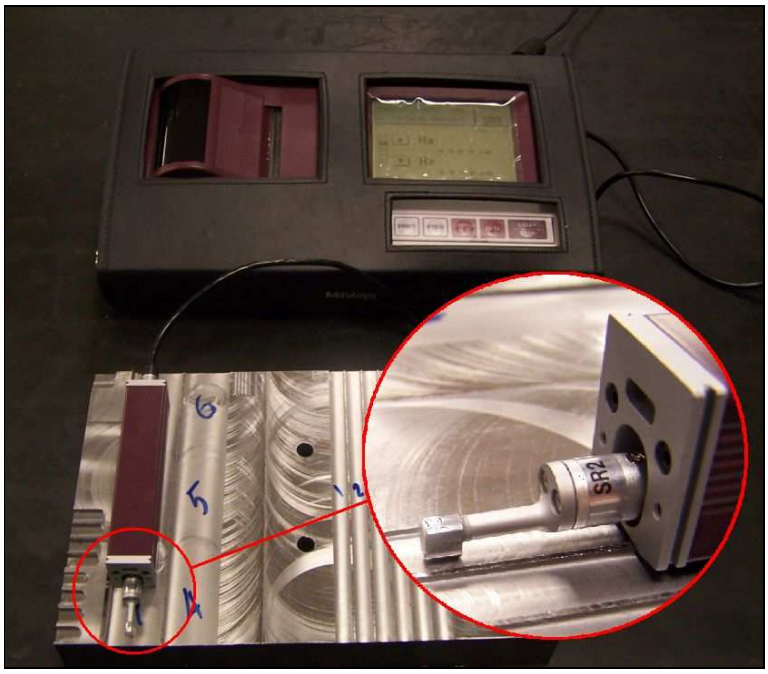

Figure 7.5: Experimental setup for roughness measurements.

7.4 Comparison of linear and trochoidal milling

In order to compare wear, surface roughness and cutting force aspects of linear and trochoidal milling, two set of experiments were performed with each milling type. Makina Takim Endustrisi (MTE) 9 mm HSS end mill cutters and AISI H 13 steel workpiece pair were used. Specifications and visualization of the cutter are given in Table 7.1 and Figure 7.6 respectively. Feed, cross-feed and axial directions cutting forces were measured for each pass. After the end of each pass, images of clearance and rake faces of the both cutters were captured and the amount of wear was measured. After completion of all the tests, surface roughness of the machined surfaces was measured.

Table 7.1: Cutter specifications.

Tool properties	**Parameters**
Model	DIN 844 BN B00276180900
Material	HSSE 8 % Co
Diameter	9 mm
Pens diameter	10 mm
Total length	69 mm
Flute length	19 mm
Projection length	30 mm
Helix angle	30 º
Rake angle	12 º
Clearance angle	8 º
Number of flutes	4

Table 7.2: Machining conditions

Machining conditions	**Parameters**
Spindle speed	1415 rpm
Cutting velocity	40 m/min
Feedrate	170 mm/min
Feed per tooth	0.03 mm/rev/tooth
Axial depth of cut	1 mm

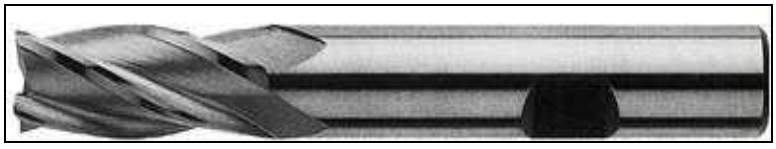

Figure 7.6: MTE 9 mm end mill.

7.4.1 Linear Toolpath

The linear toolpath tests consist of 6 passes. Within each pass a rectangular block with dimensions 162 x 9 x 1 mm was machined. The cut length was 162 mm and the full immersion slot cutting (9 mm cutter diameter) was performed at 1 mm axial depth of cut. The spindle speed and the feedrate were set as 1415 rpm and 170 mm/min respectively corresponding 40 mm/min cutting velocity and 0.03 mm feed per revolution per tooth value

(Table 7.2). The rake and clearance face images of the cutter teeth 1 to 4 are given in Figures 7.8-7.15. The results are summarized in Table 7.3 and Figure 7.7.

Table 7.3: Wear and chipping lengths on clearance and rake faces for linear milling.

		Tooth 1 (µm)		**Tooth 2** (µm)		**Tooth 3** (µm)		**Tooth 4** (µm)	
		Wear	**"Chipping"**	**Wear**	**"Chipping"**	**Wear**	**"Chipping"**	**Wear**	**"Chipping"**
Pass 1	**Clearance**	47	21	58	8	61	13	58	14
	Rake	117	10	239	14	109	13	66	13
Pass 2	**Clearance**	71	26	66	22	70	18	73	19
	Rake	241	20	242	23	177	18	93	21
Pass 3	**Clearance**	104	28	117	39	99	23	117	27
	Rake	256	31	256	58	188	34	117	24
Pass 4	**Clearance**	182	36	134	52	132	36	190	30
	Rake	270	40	263	83	223	52	146	30
Pass 5	**Clearance**	210	43	164	58	344	58	220	41
	Rake	278	60	267	93	242	58	154	42
Pass 6	**Clearance**	272	47	182	67	386	71	239	49
	Rake	303	89	281	103	256	67	162	47

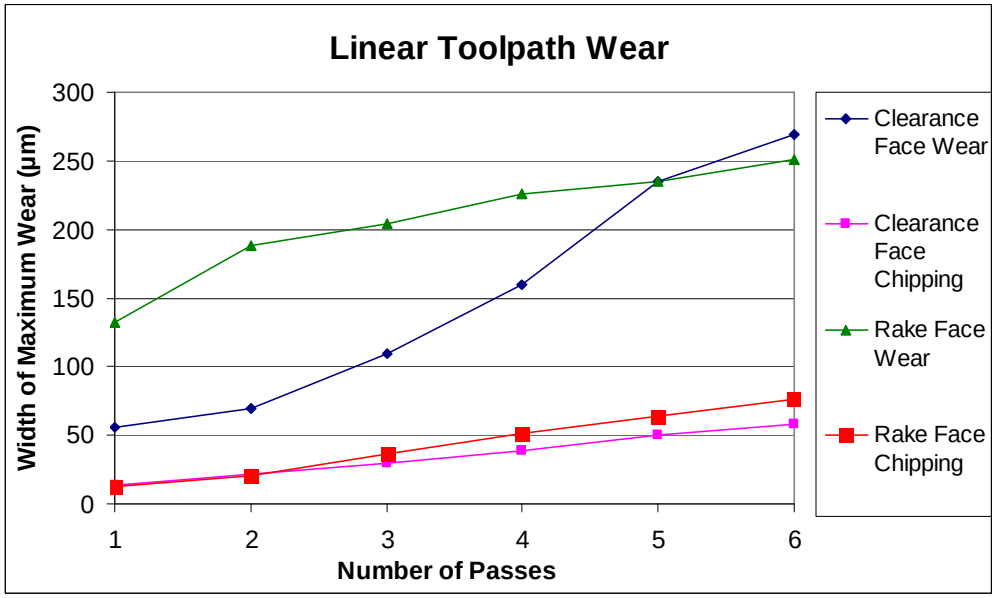

Figure 7.7: Linear toolpath average wear for all teeth at each pass corresponding to 162 mm length, 9 mm width, 1 mm depth.

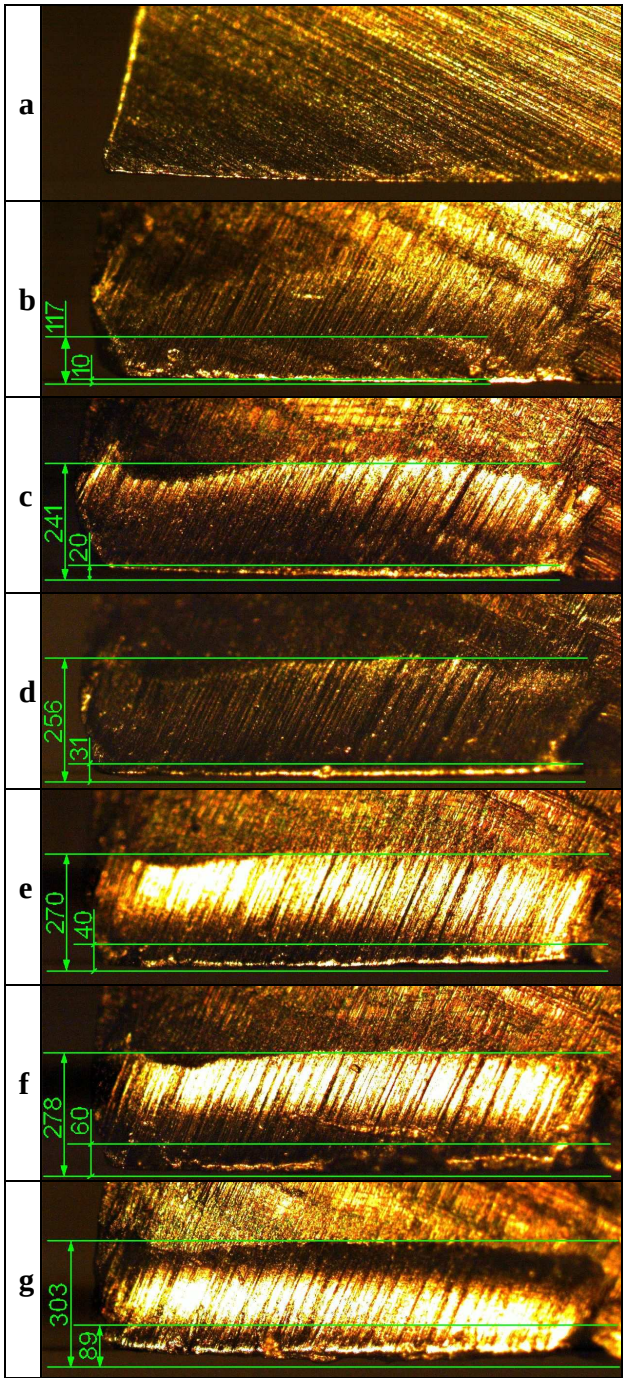

Figure 7.8: MTE 9mm end mill tooth # 1 linear toolpath rake face wear a) Fresh tool, b-g) After pass 1-6 (each 162 mm length, 9 mm width, 1 mm depth).

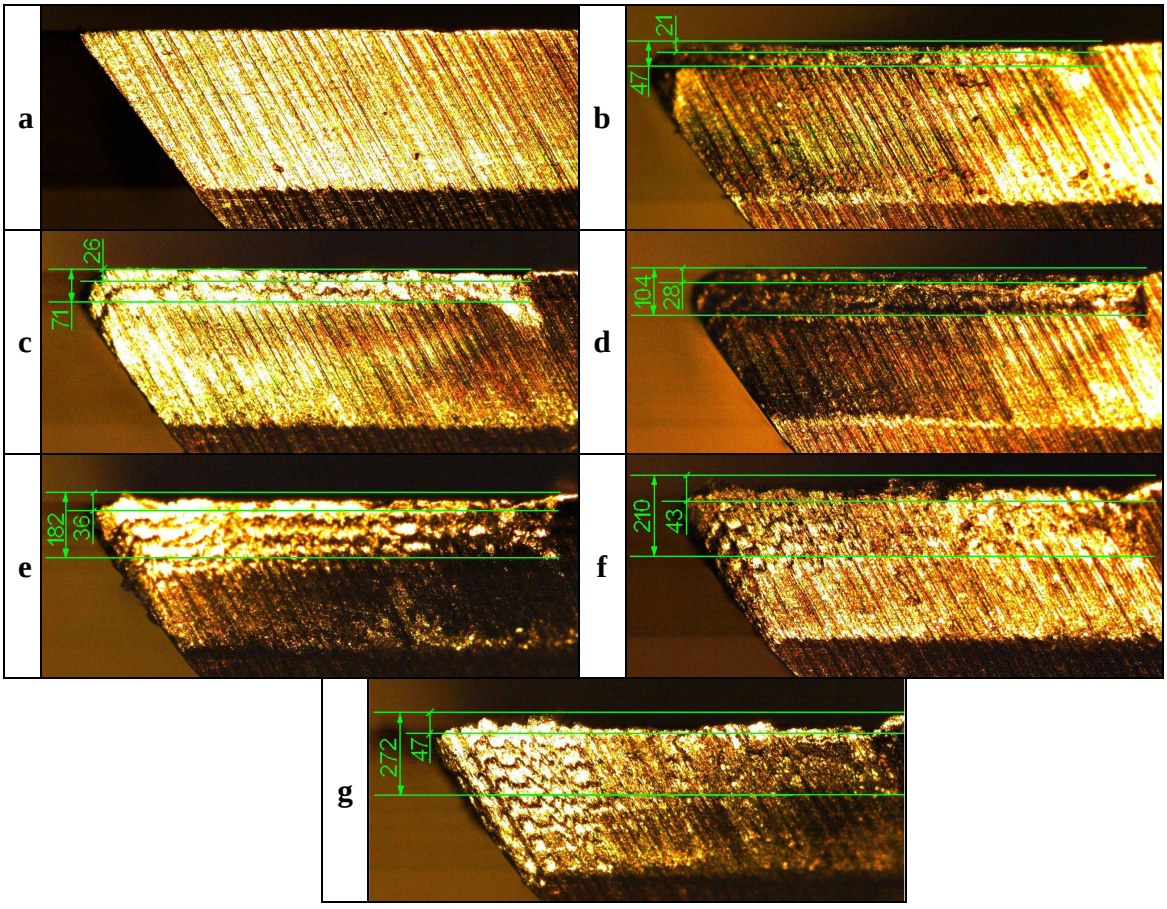

Figure 7.9: MTE 9mm end mill tooth # 1 linear toolpath clearance face wear a) Fresh tool, b-g) After pass 1-6 (each 162 mm length, 9 mm width, 1 mm depth).

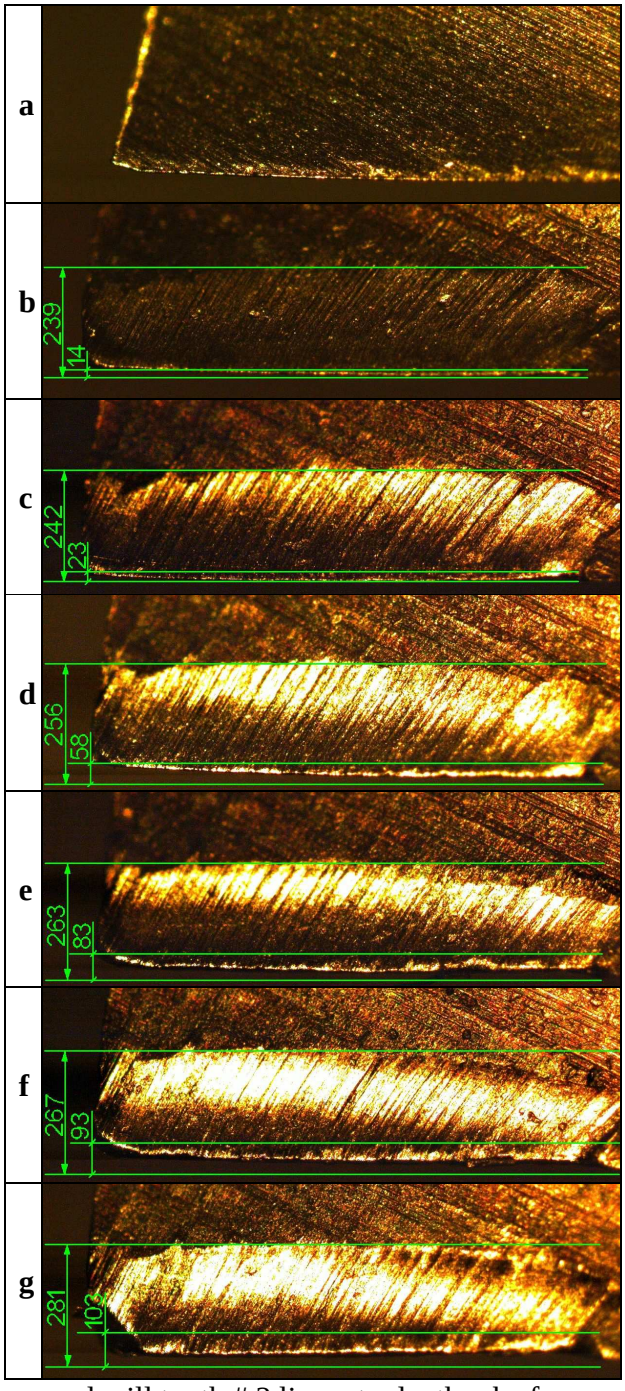

Figure 7.10: MTE 9mm end mill tooth # 2 linear toolpath rake face wear a) Fresh tool, b-g) After pass 1-6 (each 162 mm length, 9 mm width, 1 mm depth).

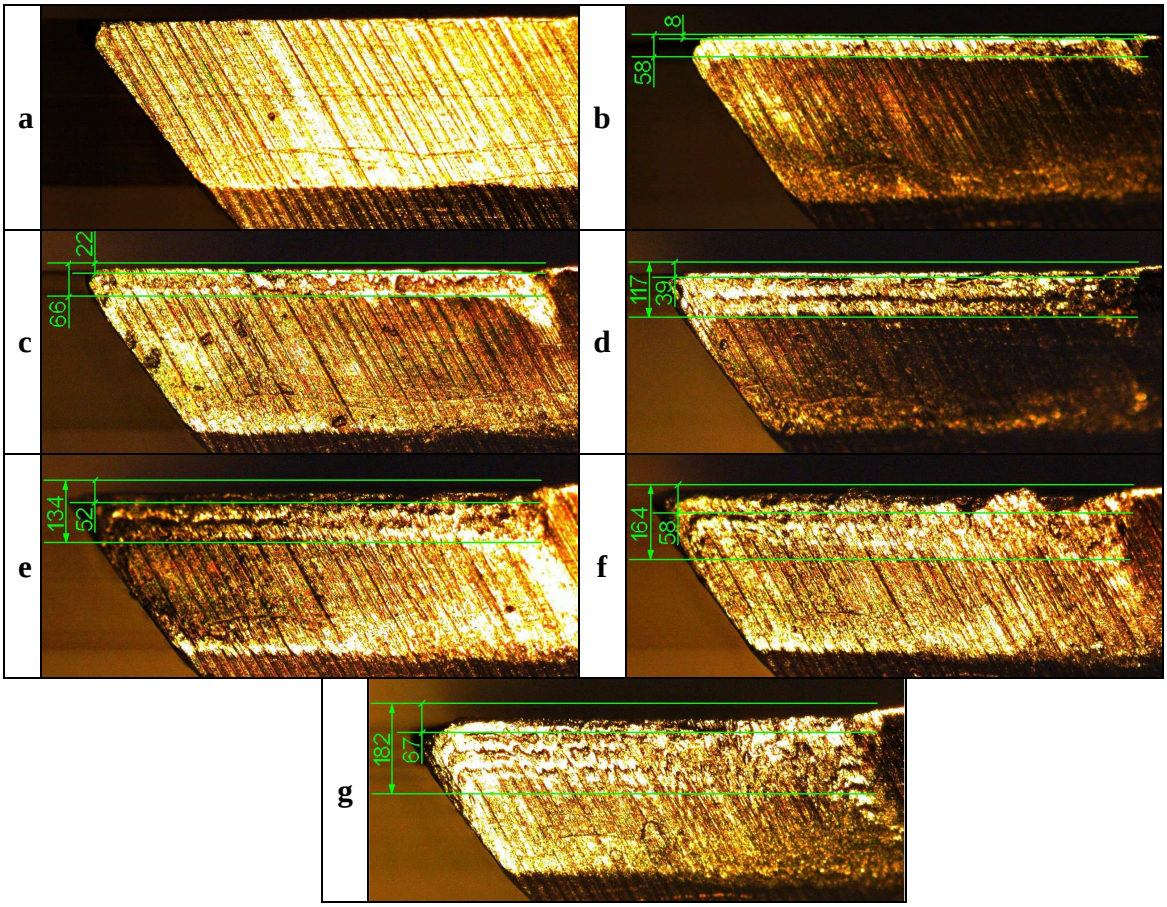

Figure 7.11: MTE 9mm end mill tooth # 2 linear toolpath clearance face wear a) Fresh tool, b-g) After pass 1-6 (each 162 mm length, 9 mm width, 1 mm depth).

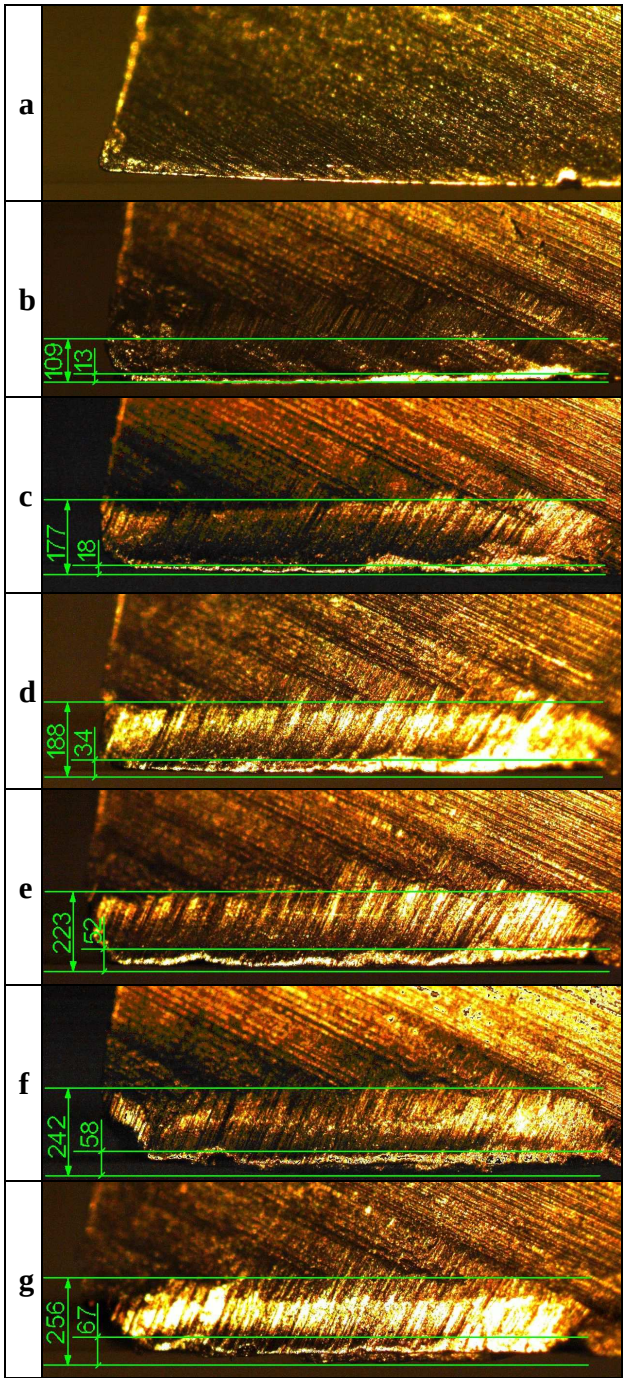

Figure 7.12: MTE 9mm end mill tooth # 3 linear toolpath rake face wear a) Fresh tool, b-g) After pass 1-6 (each 162 mm length, 9 mm width, 1 mm depth).

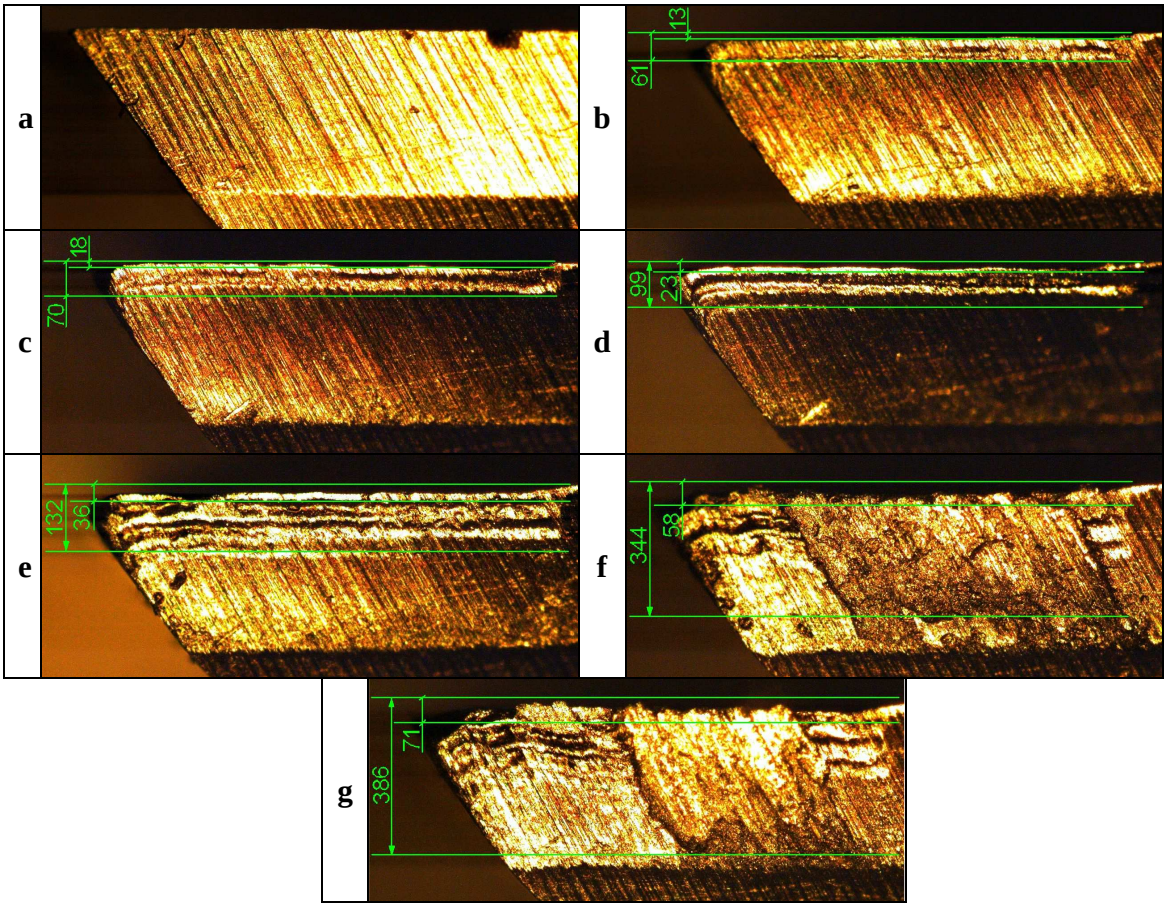

Figure 7.13: MTE 9mm end mill tooth # 3 linear toolpath clearance face wear a) Fresh tool, b-g) After pass 1-6 (each 162 mm length, 9 mm width, 1 mm depth).

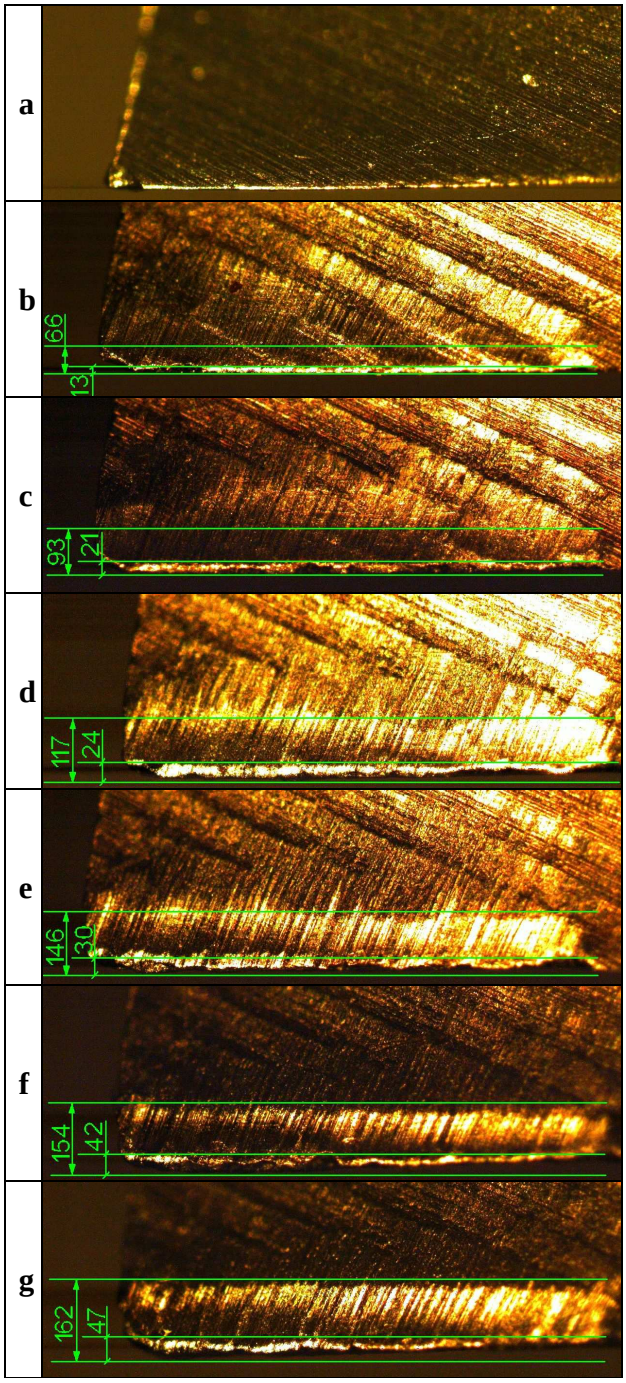

Figure 7.14: MTE 9mm end mill tooth # 4 linear toolpath rake face wear a) Fresh tool, b-g) After pass 1-6 (each 162 mm length, 9 mm width, 1 mm depth).

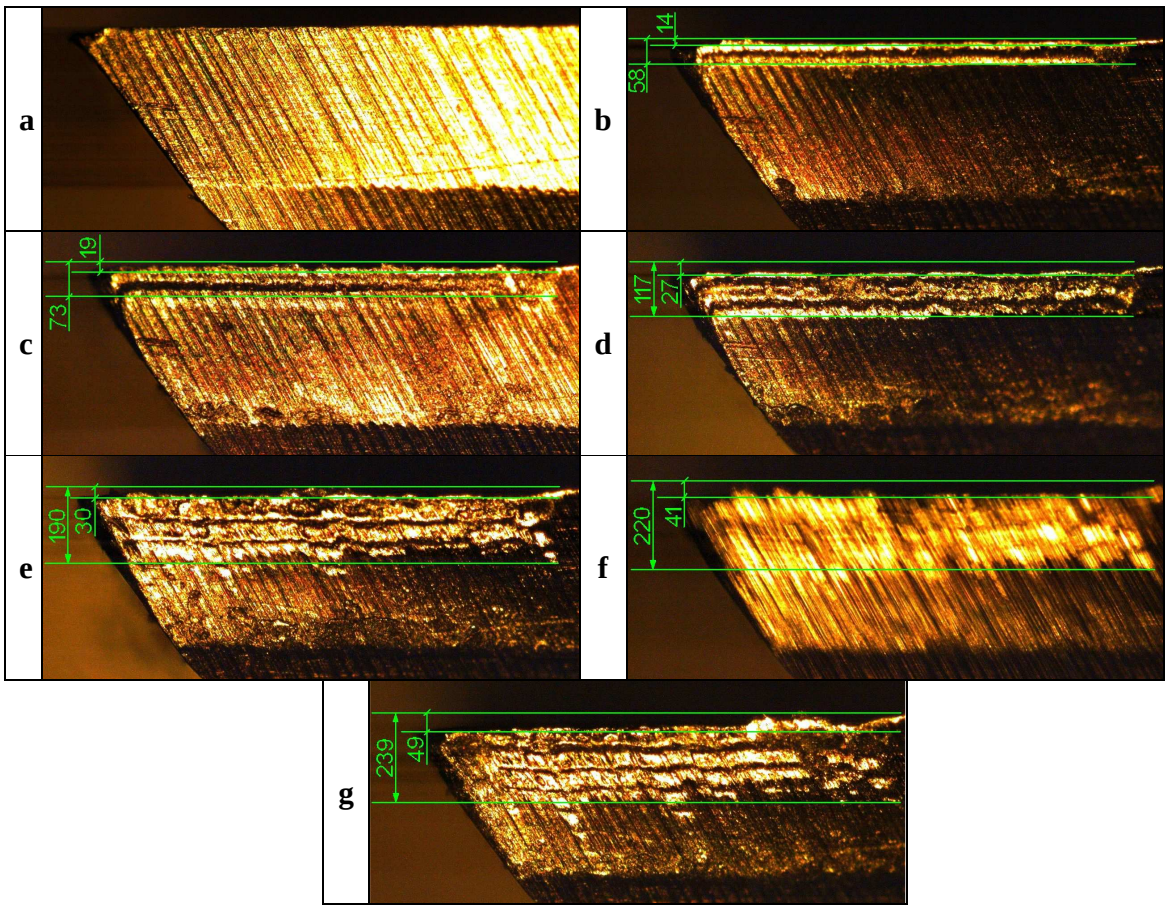

Figure 7.15: MTE 9mm end mill tooth # 4 linear toolpath clearance face wear a) Fresh tool, b-g) After pass 1-6 (each 162 mm length, 9 mm width, 1 mm depth).

In Table 7.4 and Figure 7.16 mean absolute cutting forces were summarized. Experimentally collected time data states the total machining time is 62.5 s for the linear milling operation.

Table 7.4: Mean absolute cutting forces for linear toolpath.

	F_x (N)	F_y (N)	F_R (N)
Pass 1	77.1	137.7	162.9
Pass 2	72.3	138.4	160.9
Pass 3	80.1	137.3	164.1
Pass 4	96.9	140	174.7
Pass 5	99.3	148.6	183.9
Pass 6	93.8	147.4	179.7

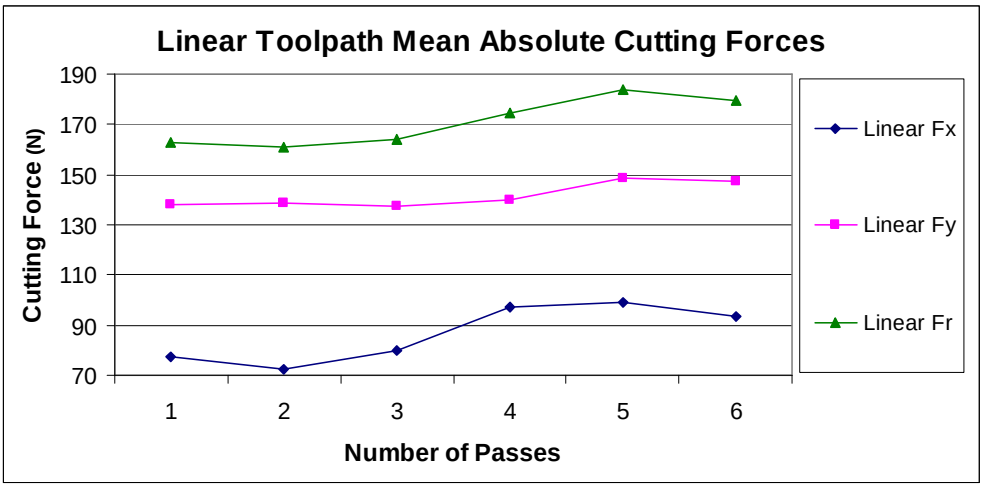

Figure 7.16: Linear toolpath mean absolute cutting forces at each pass corresponding to 162 mm length, 9 mm width, 1 mm depth.

Measured feed and cross-feed directions surface roughness values were given in Tables 7.5, 7.6 and visualization of average surface roughness was given in Figure 7.17. The measured surface profile for the nearest sample to the average of all the measurements at each pass was given in Figures 7.18, 7.19 for feed and cross-feed directions respectively.

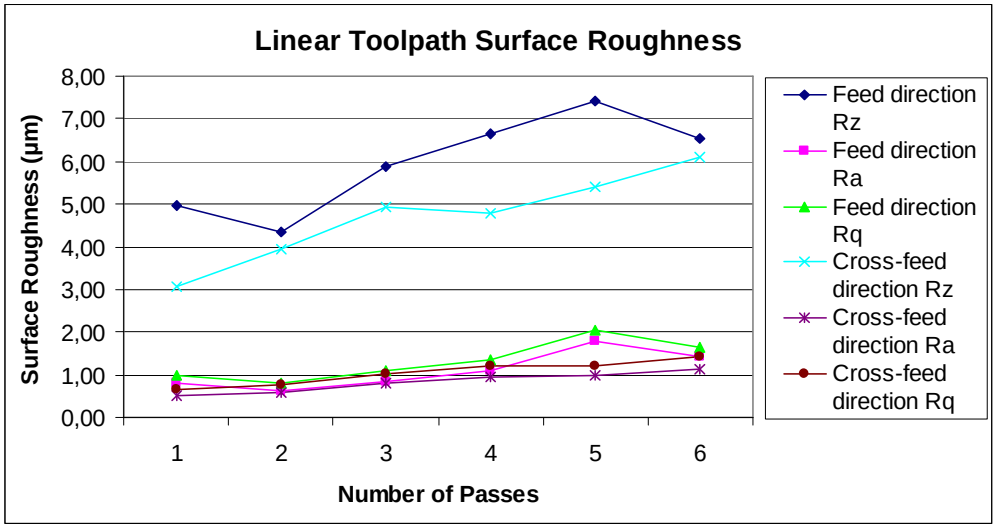

Figure 7.17: Linear toolpath surface roughness at each pass corresponding to 162 mm length, 9 mm width, 1 mm depth.

Table 7.5: Feed direction surface roughness measurements for linear toolpath.

		Sample 1	Sample 2	Sample 3	Sample 4	Sample 5	Sample 6	Mean
Pass 1	**R_a** (µm)	0.61	1.06	1.23	0.64	0.62	0.56	0.79
	R_z (µm)	4.31	5.73	6.13	5.32	4.13	4.15	4.96
	R_q (µm)	0.81	1.30	1.49	0.83	0.79	0.72	0.99
Pass 2	**R_a** (µm)	0.60	0.60	0.41	0.64	0.70	0.71	0.61
	R_z (µm)	4.46	4.40	3.59	4.43	4.61	4.61	4.35
	R_q (µm)	0.77	0.77	0.56	0.87	0.94	0.94	0.81
Pass 3	**R_a** (µm)	0.75	0.85	1.03	1.00	0.65	0.73	0.84
	R_z (µm)	5.12	6.17	6.64	8.02	4.35	5.03	5.89
	R_q (µm)	0.95	1.15	1.30	1.36	0.81	0.95	1.09
Pass 4	**R_a** (µm)	0.82	1.05	0.89	1.18	1.21	1.32	1.08
	R_z (µm)	5.96	6.87	6.22	7.08	6.57	7.22	6.65
	R_q (µm)	1.04	1.38	1.16	1.50	1.48	1.58	1.36
Pass 5	**R_a** (µm)	1.63	1.81	1.73	1.84	1.89	1.89	1.80
	R_z (µm)	7.01	7.90	7.06	7.28	7.80	7.38	7.41
	R_q (µm)	1.89	2.09	1.99	2.08	2.16	2.12	2.06
Pass 6	**R_a** (µm)	1.37	1.39	1.78	2.06	1.03	0.94	1.43
	R_z (µm)	6.52	6.42	7.53	8.22	5.55	4.96	6.53
	R_q (µm)	1.61	1.60	2.03	2.28	1.24	1.11	1.65

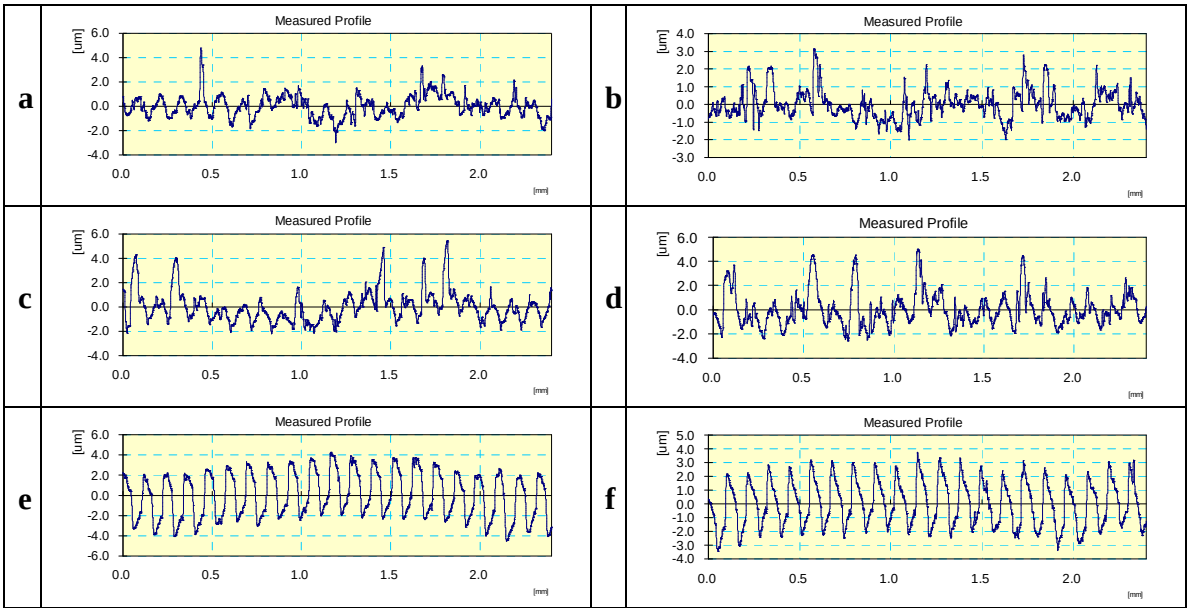

Figure 7.18: MTE 9mm end mill linear toolpath feed direction measured profiles for surface roughness that are closest to the mean value after pass 1-6 (each 162 mm length, 9 mm width, 1 mm depth).

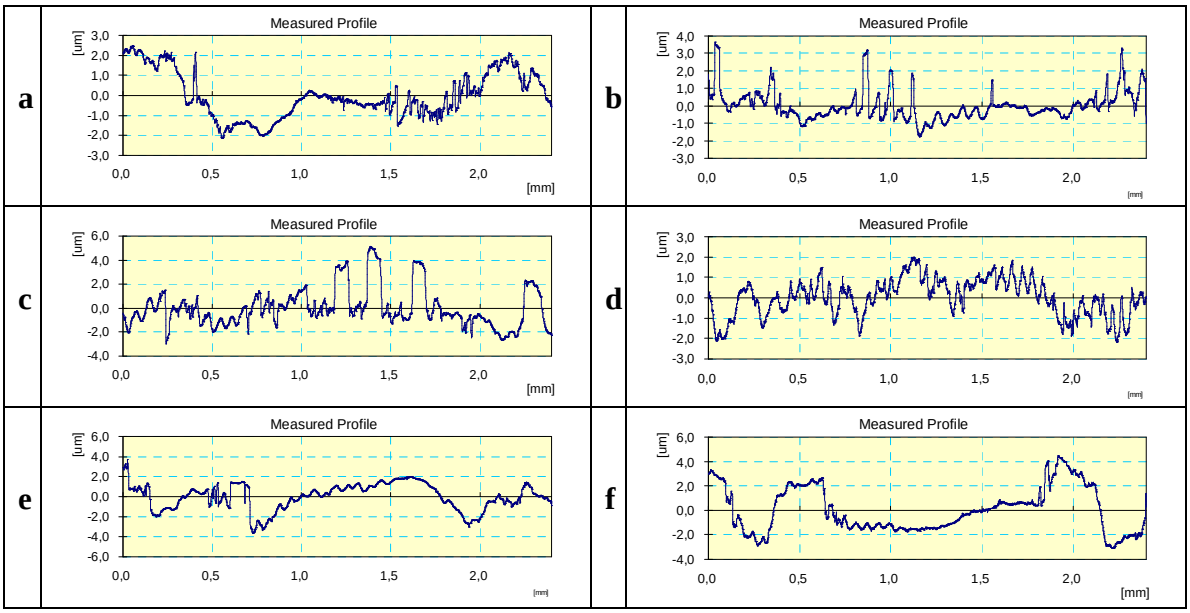

Figure 7.19: MTE 9mm end mill linear toolpath feed direction measured profiles for surface roughness that are closest to the mean value after pass 1-6 (each 162 mm length, 9 mm width, 1 mm depth).

Table 7.6: Cross-feed direction surface roughness measurements for linear toolpath.

		Sample 1	Sample 2	Sample 3	Sample 4	Sample 5	Sample 6	Mean
Pass 1	R_a (µm)	0,63	0,52	0,42	0,49	0,58	0,46	0,52
	R_z (µm)	3,21	3,02	2,21	2,85	4,29	2,9	3,08
	R_q (µm)	0,84	0,63	0,52	0,61	0,78	0,58	0,66
Pass 2	R_a (µm)	0,41	0,65	0,42	0,63	0,51	0,79	0,57
	R_z (µm)	2,05	4,3	4,13	4,09	4,4	4,79	3,96
	R_q (µm)	0,51	0,81	0,6	0,85	0,71	1,05	0,76
Pass 3	R_a (µm)	0,67	0,61	1,07	0,63	1,07	0,67	0,79
	R_z (µm)	4,43	4,69	6,3	3,21	6,54	4,43	4,93
	R_q (µm)	0,83	0,8	1,35	0,84	1,44	0,83	1,02
Pass 4	R_a (µm)	1,24	0,98	0,88	1,03	1,01	0,63	0,96
	R_z (µm)	5,78	4,98	4,20	4,93	5,27	3,53	4,78
	R_q (µm)	1,56	1,17	1,06	1,27	1,29	0,78	1,19
Pass 5	R_a (µm)	0,8	0,85	1,27	0,82	1,19	0,88	0,97
	R_z (µm)	4,53	5,75	7,17	4,13	6,46	4,44	5,41
	R_q (µm)	1	1,12	1,53	1	1,46	1,05	1,19
Pass 6	R_a (µm)	1,29	1,15	1,28	0,84	1,28	1,04	1,15
	R_z (µm)	7,28	5,44	6,10	3,98	8,21	5,57	6,10
	R_q (µm)	1,53	1,36	1,51	1,08	1,71	1,27	1,41

7.4.2 Trochoidal Toolpath

The trochoidal toolpath tests consist of 6 passes, 54 x 27 x 1 mm. The spindle speed and the feedrate were set as 1415 rpm and 170 mm/min respectively corresponding 40 mm/min cutting velocity and 0.03 mm feed per revolution per tooth value. The radius of the planetary revolution was 9 mm and the stepover between the revolutions were 1 mm. The rake and clearance face images of the cutter teeth 1 to 4 are given in Figures 7.20-7.27. The results are summarized in Table 7.7 and Figure 7.28.

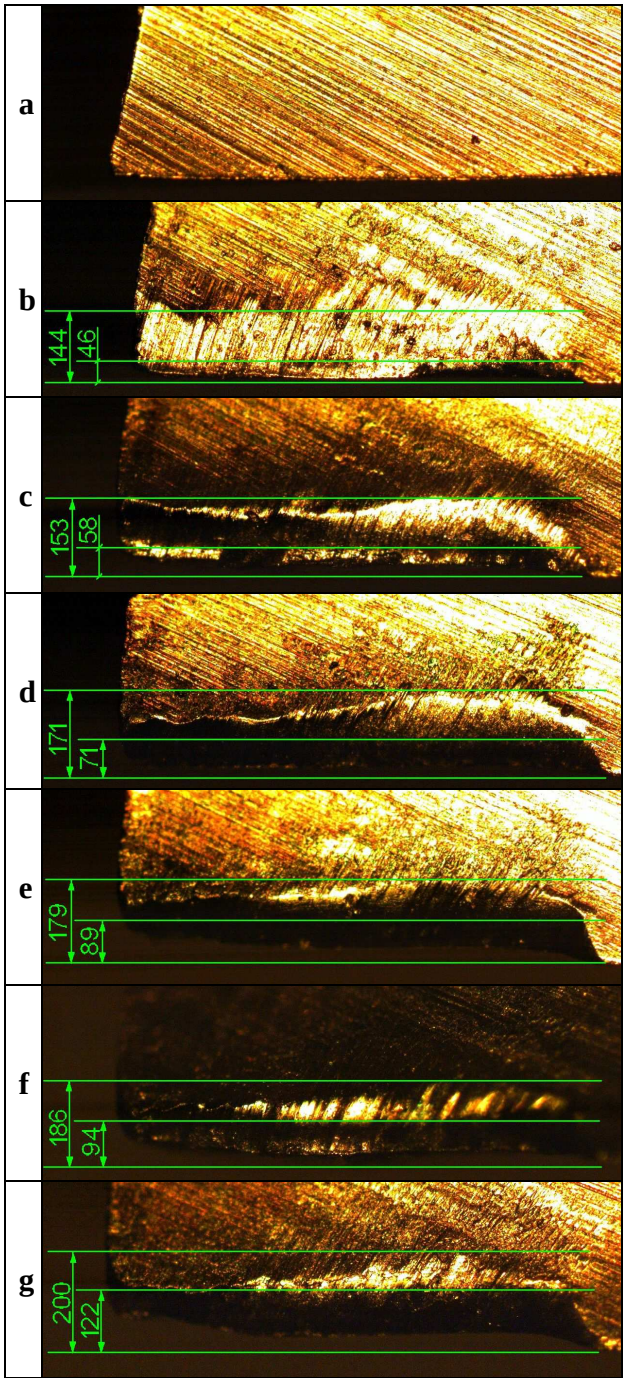

Figure 7.20: MTE 9mm end mill tooth # 1 trochoidal toolpath rake face wear a) Fresh tool, b-g) After pass 1-6 (each 54 mm length, 27 mm width, 1 mm depth).

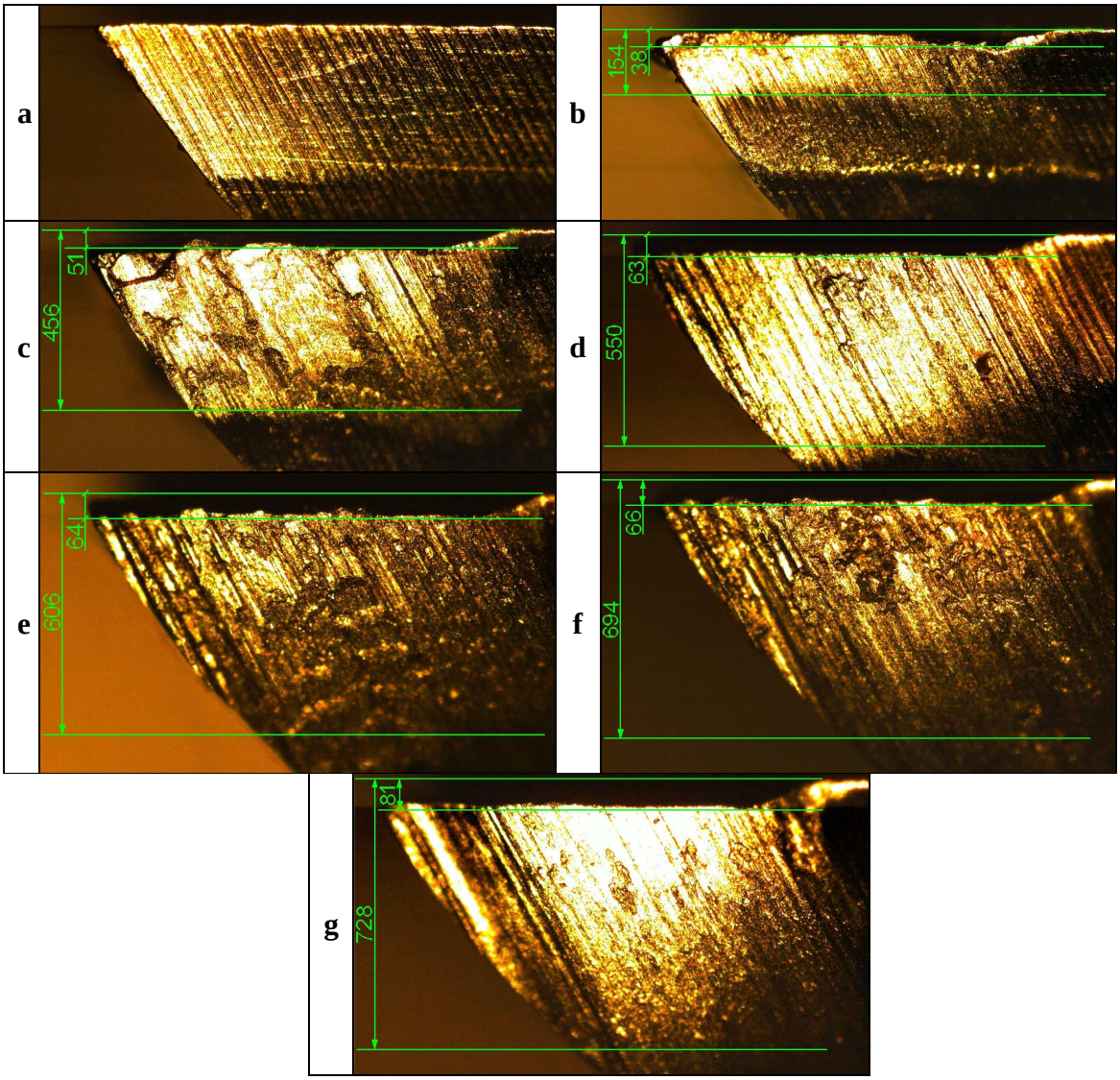

Figure 7.21: MTE 9mm end mill tooth # 1 trochoidal toolpath clearance face wear a) Fresh tool, b-g) After pass 1-6 (each 54 mm length, 27 mm width, 1 mm depth).

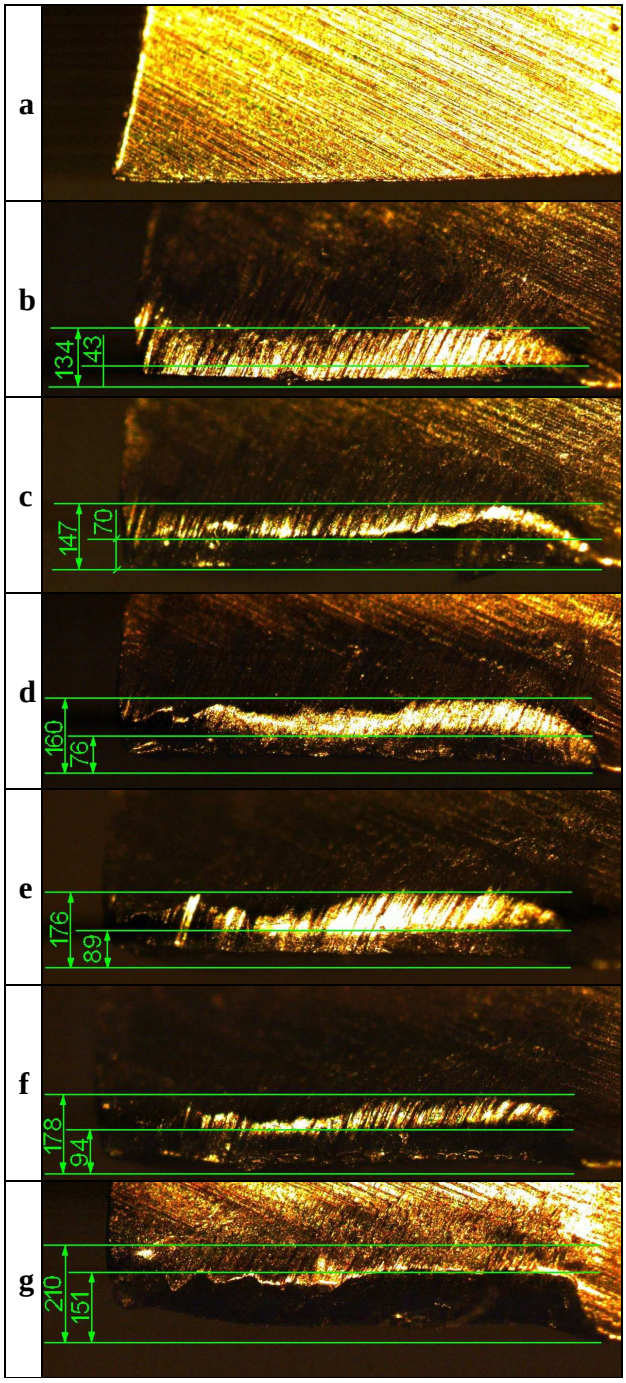

Figure 7.22: MTE 9mm end mill tooth # 2 trochoidal toolpath rake face wear a) Fresh tool, b-g) After pass 1-6 (each 54 mm length, 27 mm width, 1 mm depth).

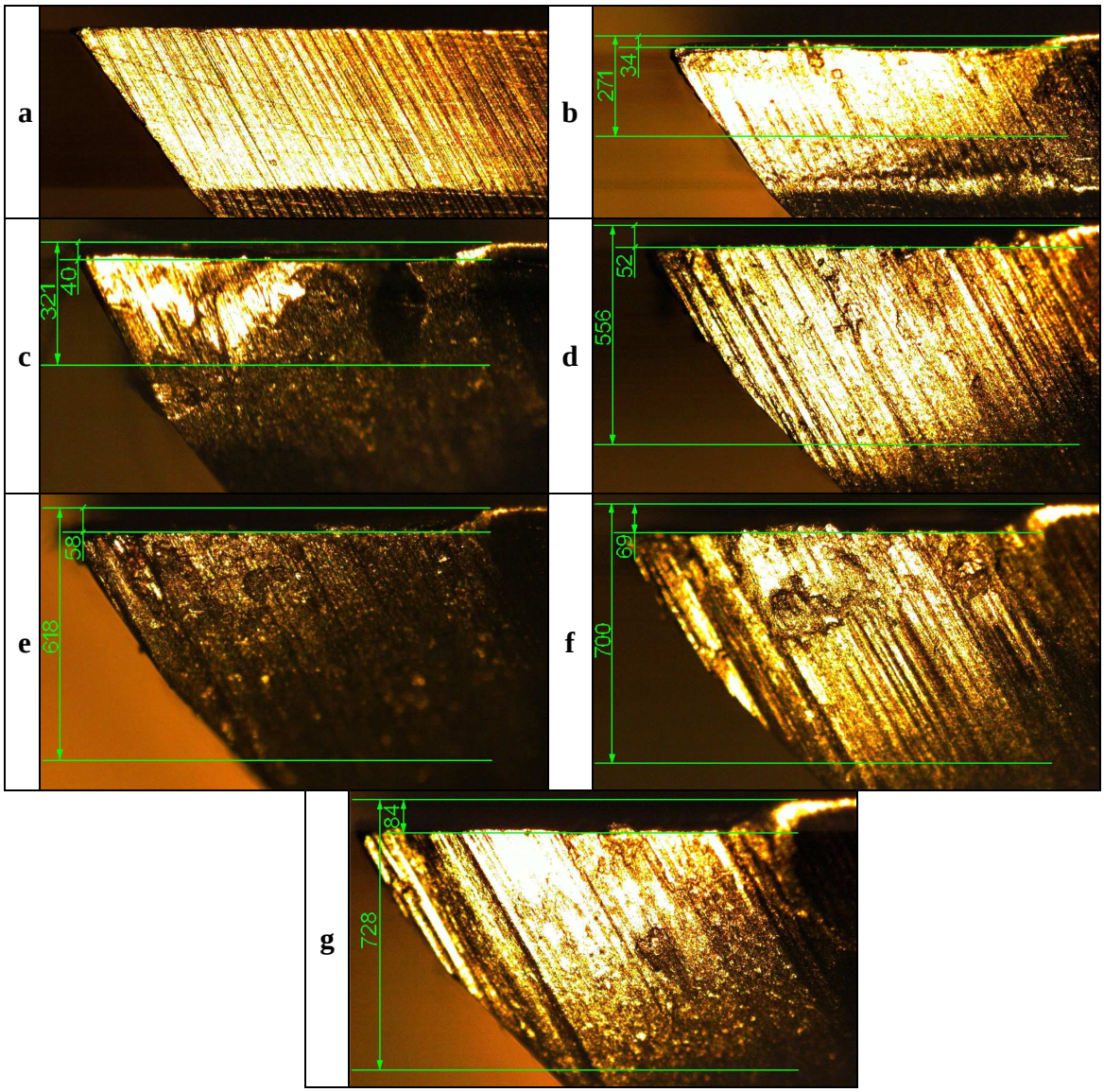

Figure 7.23: MTE 9mm end mill tooth # 2 trochoidal toolpath clearance face wear a) Fresh tool, b-g) After pass 1-6 (each 54 mm length, 27 mm width, 1 mm depth).

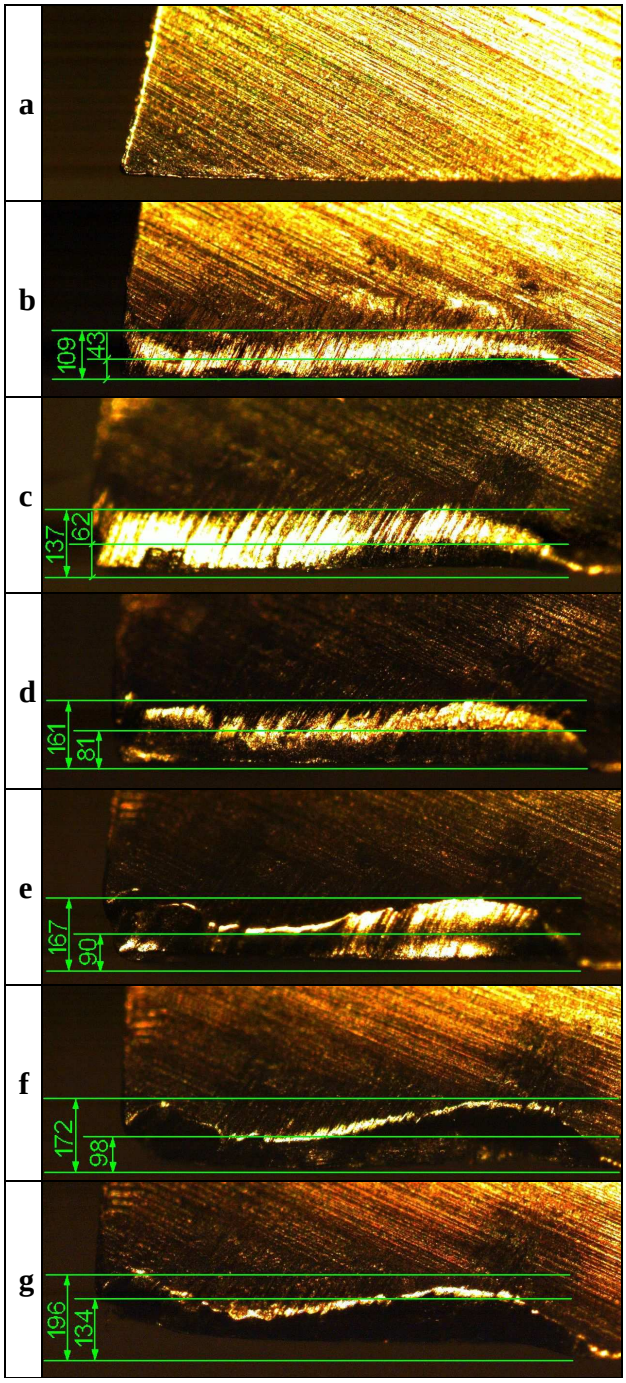

Figure 7.24: MTE 9mm end mill tooth # 3 trochoidal toolpath rake face wear a) Fresh tool, b-g) After pass 1-6 (each 54 mm length, 27 mm width, 1 mm depth).

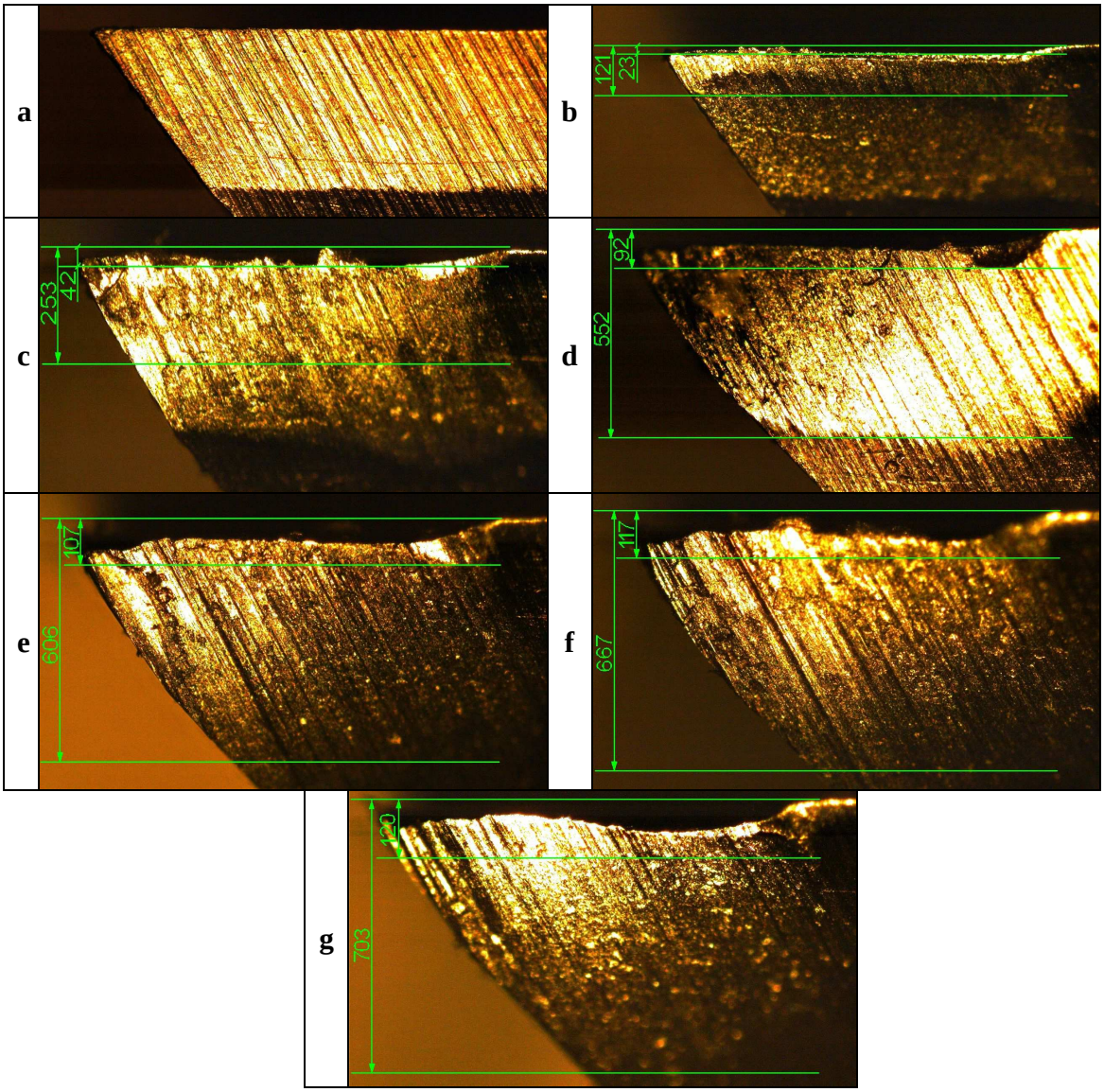

Figure 7.25: MTE 9mm end mill tooth # 3 trochoidal toolpath clearance face wear a) Fresh tool, b-g) After pass 1-6 (each 54 mm length, 27 mm width, 1 mm depth).

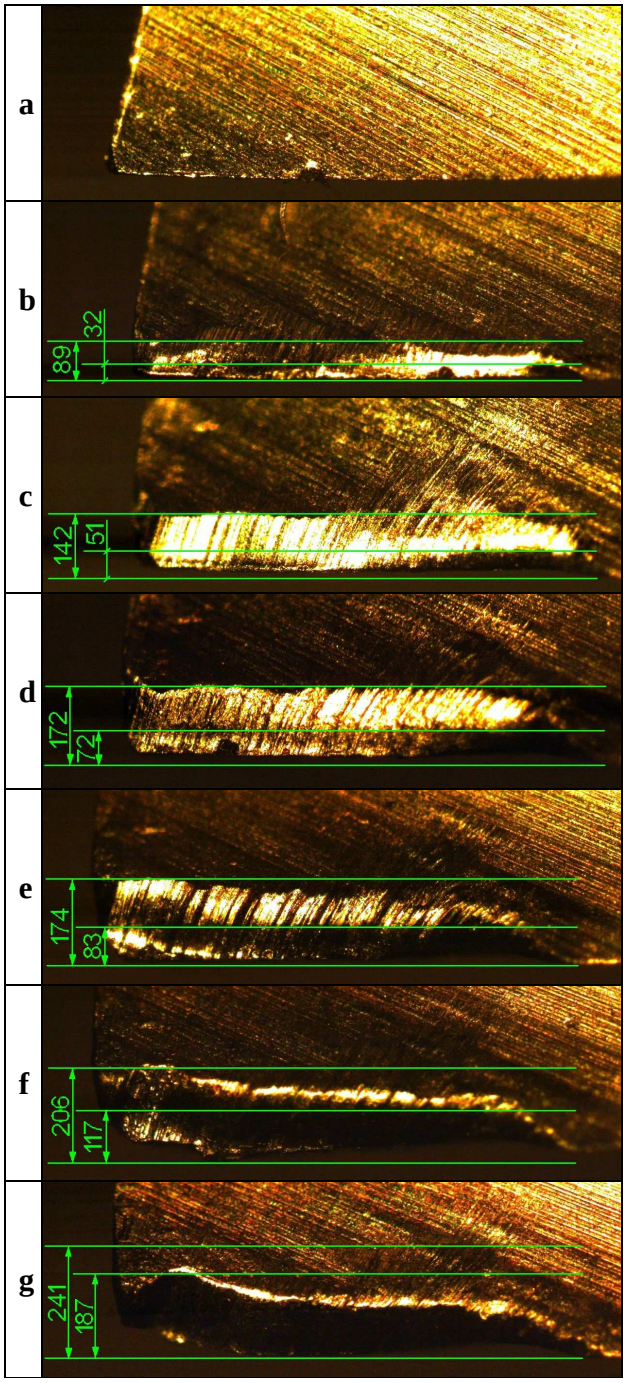

Figure 7.26: MTE 9mm end mill tooth # 4 trochoidal toolpath rake face wear a) Fresh tool, b-g) After pass 1-6 (each 54 mm length, 27 mm width, 1 mm depth).

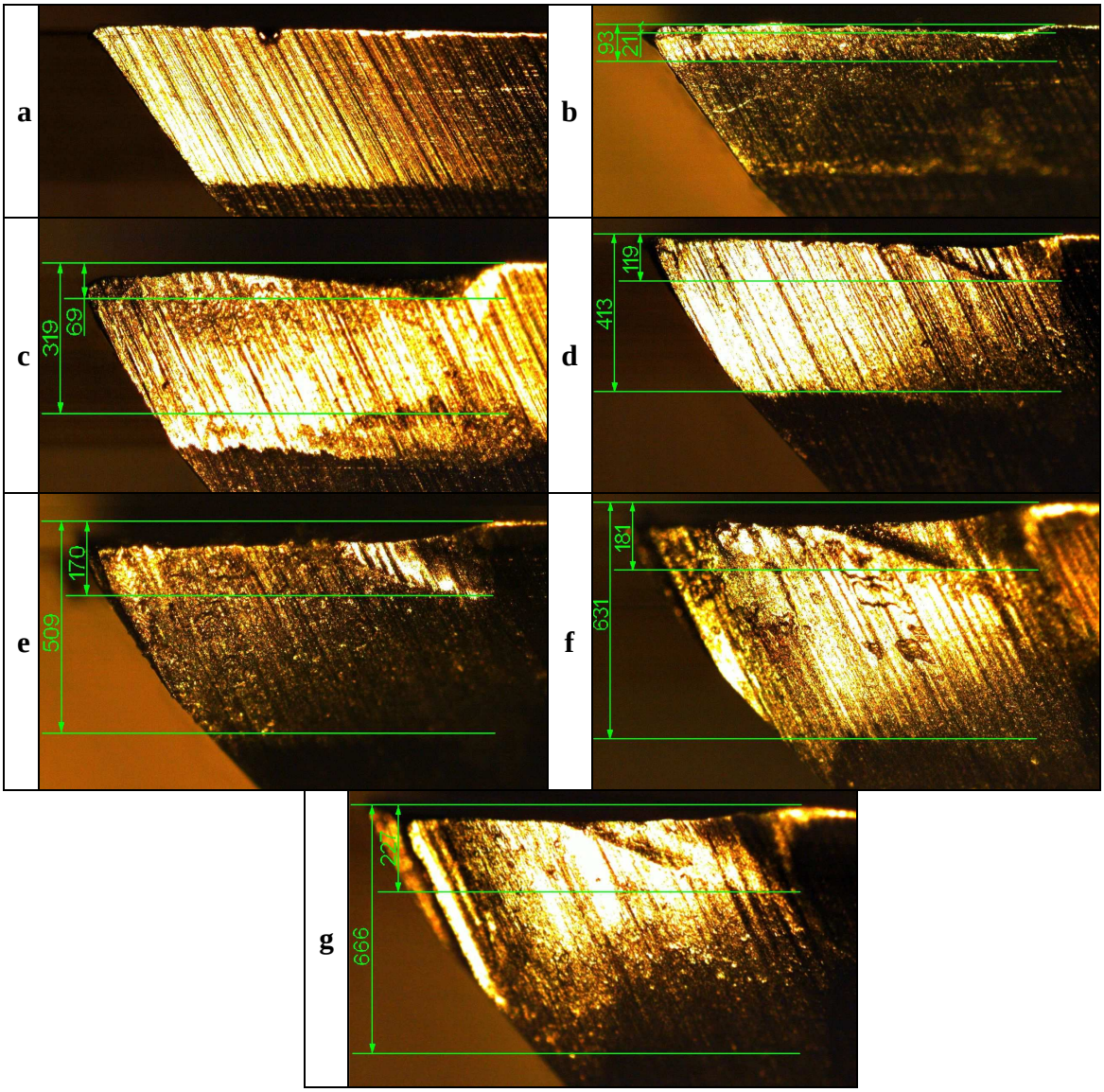

Figure 7.27: MTE 9mm end mill tooth # 4 trochoidal toolpath clearance face wear a) Fresh tool, b-g) After pass 1-6 (each 54 mm length, 27 mm width, 1 mm depth).

Table 7.7: Wear and chipping lengths on clearance and rake faces for trochoidal milling.

		Tooth 1 (µm)		**Tooth 2** (µm)		**Tooth 3** (µm)		**Tooth 4** (µm)	
		Wear	**"Chipping"**	**Wear**	**"Chipping"**	**Wear**	**"Chipping"**	**Wear**	**"Chipping"**
Pass 1	**Clearance**	154	38	271	34	121	23	93	21
	Rake	144	46	134	43	109	43	89	32
Pass 2	**Clearance**	456	51	321	40	253	42	319	69
	Rake	153	58	147	70	137	62	142	51
Pass 3	**Clearance**	550	63	556	52	552	96	413	119
	Rake	171	71	160	76	161	81	172	72
Pass 4	**Clearance**	606	64	618	58	606	107	509	178
	Rake	178	89	176	89	167	90	174	83
Pass 5	**Clearance**	694	66	700	69	667	117	631	181
	Rake	186	94	178	98	172	98	206	117
Pass 6	**Clearance**	739	81	728	84	703	120	666	227
	Rake	200	122	210	151	196	134	241	187

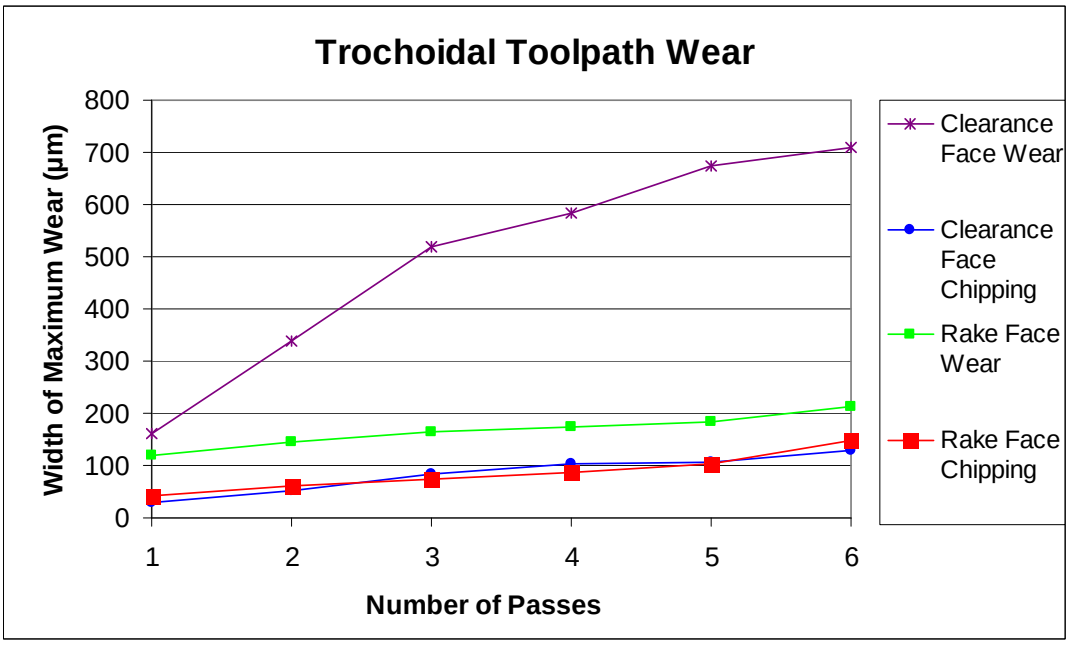

Figure 7.28: Trochoidal toolpath average wear for all teeth at each pass corresponding to 162 mm length, 9 mm width, 1 mm depth.

In Table 7.8 and Figure 7.29 mean absolute cutting forces were summarized. Experimentally collected time data states the total machining time is 1257 s for the trochoidal milling operation. Measured feed and cross-feed directions surface roughness values were given in Tables 7.9, 7.10 and visualization of average surface roughness was given in Figure 7.30. The measured surface profile for the nearest sample to the average of all the measurements at each pass was given in Figures 7.31, 7.32 for feed and cross-feed directions respectively.

Table 7.8: Mean absolute cutting forces for trochoidal toolpath

	F_x (N)	F_y (N)	F_R (N)
Pass 1	11.5	17	22.6
Pass 2	17.8	24.4	33.3
Pass 3	23.3	31.7	43.4
Pass 4	24.3	33	45.2
Pass 5	29.2	36.5	51.8
Pass 6	34.8	40	59

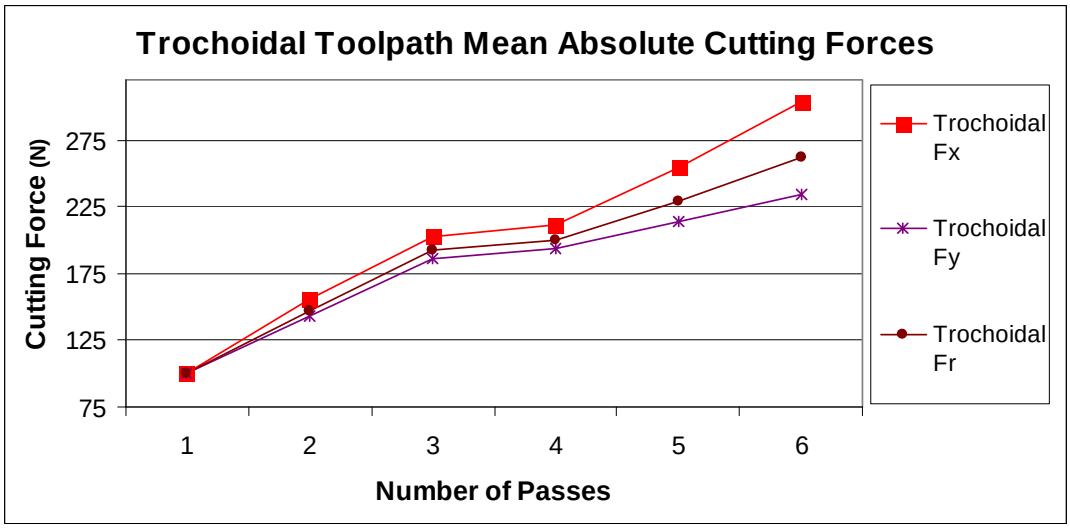

Figure 7.29: Linear toolpath mean absolute cutting forces at each pass corresponding to 162 mm length, 9 mm width, 1 mm depth.

Table 7.9: Feed direction surface roughness measurements for trochoidal toolpath

		Sample 1	Sample 2	Sample 3	Sample 4	Sample 5	Sample 6	Mean
Pass 1	R_a (µm)	1.41	1.30	1.26	0.84	1.16	1.10	1.41
	R_z (µm)	7.33	6.51	5.57	5.70	6.73	6.51	7.33
	R_q (µm)	1.73	1.56	1.45	1.06	1.50	1.36	1.73
Pass 2	R_a (µm)	0.99	0.97	1.60	1.18	0.99	1.11	0.99
	R_z (µm)	6.03	5.76	6.87	5.51	6.05	5.63	6.03
	R_q (µm)	1.23	1.24	1.82	1.37	1.22	1.34	1.23
Pass 3	R_a (µm)	1.72	1.79	1.42	1.68	1.87	1.56	1.72
	R_z (µm)	7.70	7.57	6.11	7.51	8.40	7.27	7.70
	R_q (µm)	2.02	2.05	1.65	1.93	2.14	1.84	2.02
Pass 4	R_a (µm)	1.39	1.26	1.50	1.44	1.27	1.39	1.39
	R_z (µm)	6.51	6.98	7.24	7.07	6.57	6.51	6.51
	R_q (µm)	1.68	1.51	1.76	1.73	1.50	1.68	1.68
Pass 5	R_a (µm)	1.30	0.80	0.99	1.25	1.07	1.06	1.30
	R_z (µm)	7.10	5.54	5.76	6.91	6.28	6.57	7.10
	R_q (µm)	1.55	1.03	1.21	1.52	1.31	1.34	1.55
Pass 6	R_a (µm)	1.00	1.39	1.21	1.33	1.11	1.31	1.00
	R_z (µm)	6.34	6.73	6.02	7.18	6.67	6.90	6.34
	R_q (µm)	1.26	1.60	1.41	1.57	1.37	1.55	1.26

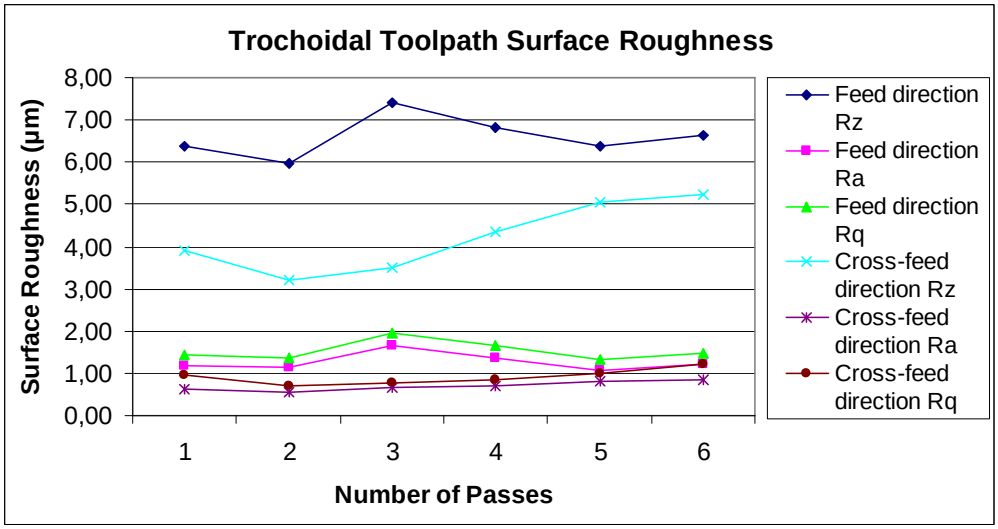

Figure 7.30: Trochoidal toolpath surface roughness at each pass corresponding to 162 mm length, 9 mm width, 1 mm depth.

Table 7.10: Cross-feed direction surface roughness measurements for trochoidal toolpath

		Sample 1	Sample 2	Sample 3	Sample 4	Sample 5	Sample 6	Mean
Pass 1	**R_a** (µm)	0,45	0,51	0,97	0,62	0,36	0,87	0,63
	R_z (µm)	2,68	3,16	6,30	3,33	2,7	5,36	3,92
	R_q (µm)	1,55	0,64	1,27	0,78	0,46	1,1	0,97
Pass 2	**R_a** (µm)	0,63	0,32	0,9	0,5	0,51	0,51	0,56
	R_z (µm)	3,03	2,64	4,8	2,7	3,16	2,84	3,20
	R_q (µm)	0,74	0,41	1,12	0,6	0,64	0,6	0,69
Pass 3	**R_a** (µm)	0,75	0,32	0,66	0,81	0,42	0,93	0,65
	R_z (µm)	3,9	2,41	3,96	3,72	2,72	4,21	3,49
	R_q (µm)	0,95	0,4	0,81	0,96	0,52	1,09	0,79
Pass 4	**R_a** (µm)	0,83	0,60	0,79	0,68	0,58	0,65	0,69
	R_z (µm)	4,70	3,97	4,69	3,94	4,45	4,36	4,35
	R_q (µm)	0,99	0,76	1,00	0,83	0,76	0,83	0,86
Pass 5	**R_a** (µm)	0,74	0,62	0,98	0,81	0,91	0,80	0,81
	R_z (µm)	4,56	3,56	6,17	5,14	5,32	5,46	5,04
	R_q (µm)	0,90	0,76	1,26	1,02	1,09	1,02	1,01
Pass 6	**R_a** (µm)	1,02	0,74	0,81	0,8	0,9	0,84	0,85
	R_z (µm)	5,57	4,75	4,86	4,91	5,84	5,56	5,25
	R_q (µm)	1,26	0,93	1,01	1,91	1,13	1,04	1,21

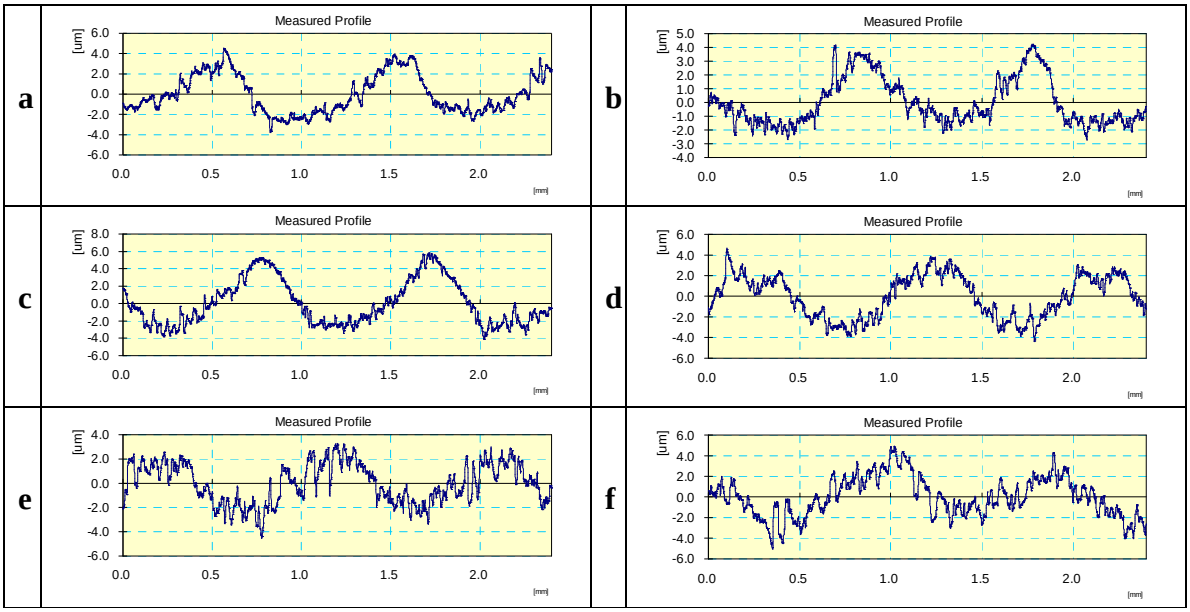

Figure 7.31: MTE 9mm end mill trochoidal toolpath feed direction measured profiles for surface roughness that are closest to the mean value after pass 1-6 (each 54 mm length, 27 mm width, 1 mm depth).

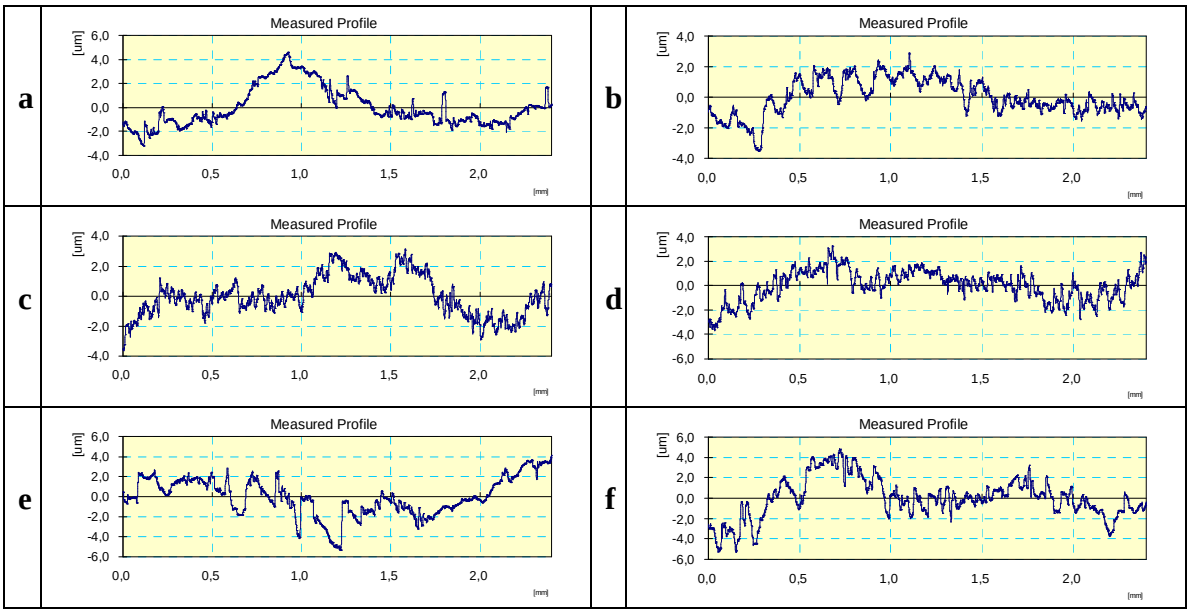

Figure 7.32: MTE 9mm end mill trochoidal toolpath cross-feed direction measured profiles for surface roughness that are closest to the mean value after pass 1-6 (each 54 mm length, 27 mm width, 1 mm depth).

7.4.3 Comparison of Wear, Surface Roughness and Force Aspects

First of all the machining time for trochoidal milling operation (1257 s) is approximately 20 times of the one for linear milling operation (62.5). This significant disadvantage was expected to be defeated considering the wear aspects as the engagement conditions are lighter in trochoidal toolpath. Experimental studies figured out the fact that in the investigated cutting conditions trochoidal toolpath showed worse wear characteristics than linear probably due to the longer cutting cycles in the toolpath. In Figures 7.33, 7.34 average feed and cross-feed directions surface roughness values for trochoidal and linear toolpath are shown. The average surface roughness values are higher for trochoidal toolpath rather than linear toolpath. Figure 7.35 presents the mean absolute cutting forces for each pass normalized over the first pass. The increase of the cutting forces with respect to the passes in trochoidal milling is two to three times greater than linear one. Finally Figure 7.36 illustrates the average tool wear after each pass. Rake and clearance face chipping and wear values are higher for trochoidal milling.

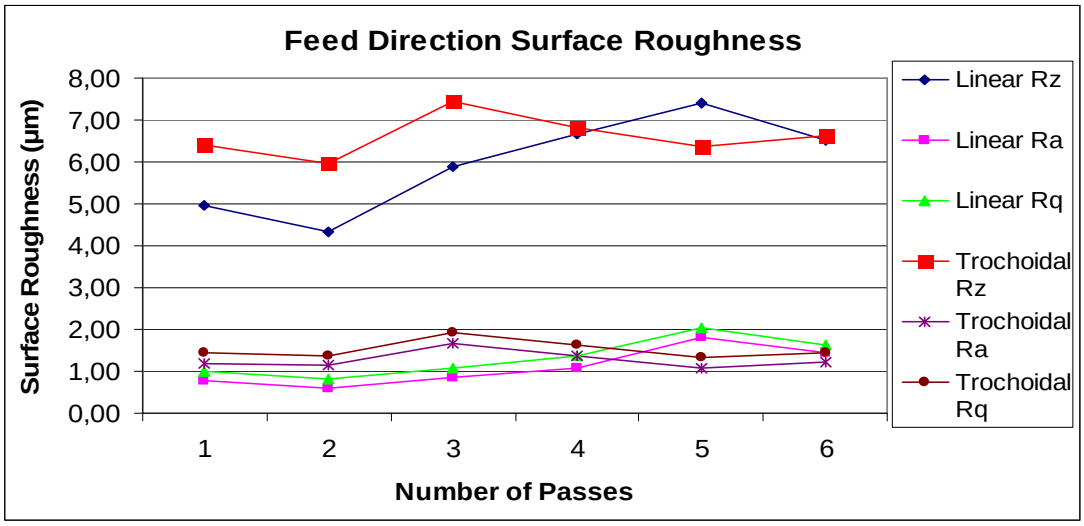

Figure 7.33: Trochoidal and linear toolpaths feed direction surface roughness comparison at each pass corresponding to 162 mm length, 9 mm width, 1 mm depth for linear toolpath and 54 mm length, 27 mm width, 1 mm depth for trochoidal toolpath.

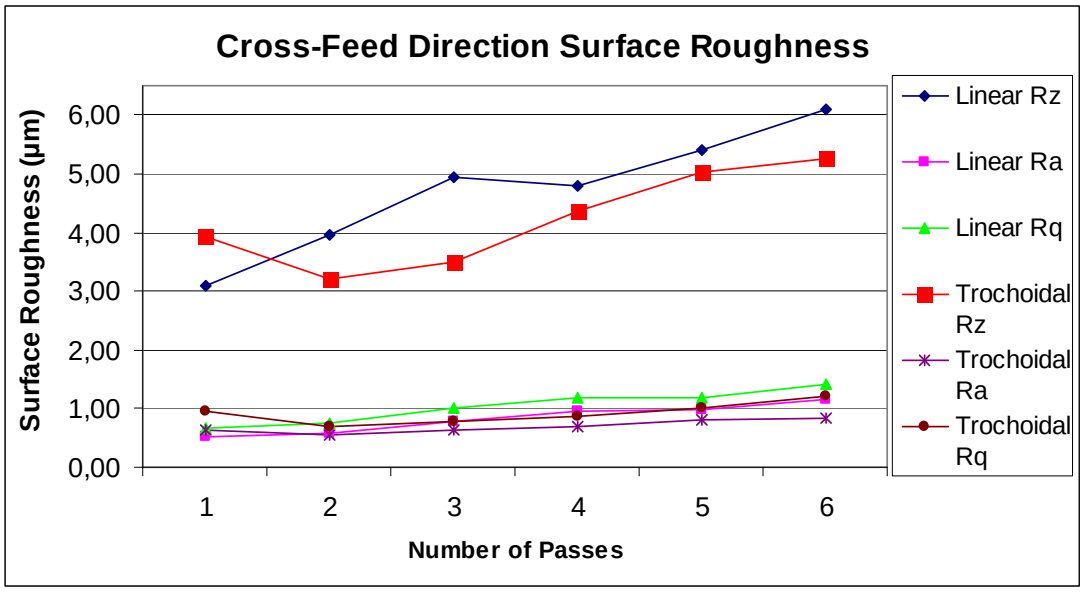

Figure 7.34: Trochoidal and linear toolpaths cross-feed direction surface roughness comparison at each pass corresponding to 162 mm length, 9 mm width, 1 mm depth for linear toolpath and 54 mm length, 27 mm width, 1 mm depth for trochoidal toolpath.

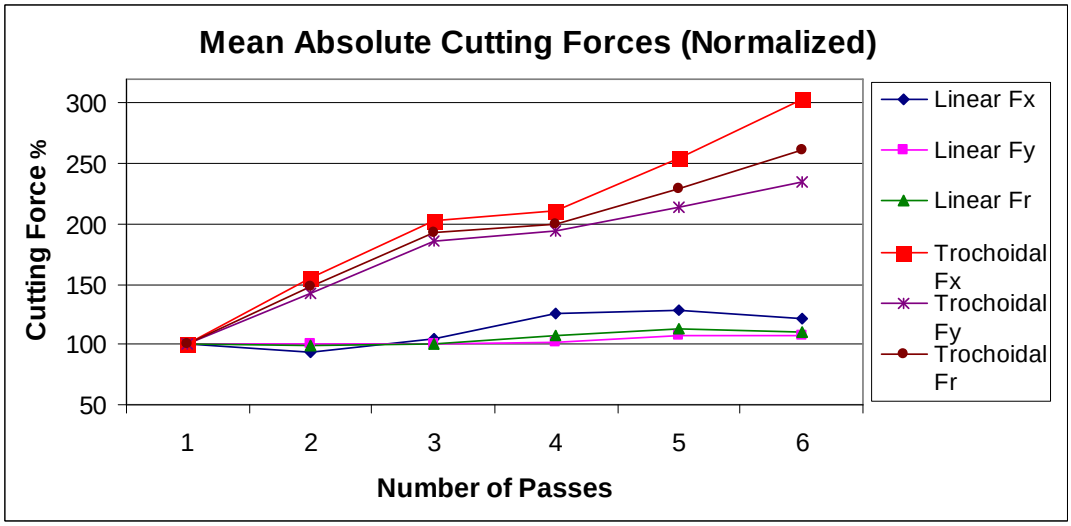

Figure 7.35: Comparison of trochoidal and linear toolpaths cutting forces normalized over the first pass at each pass corresponding to 162 mm length, 9 mm width, 1 mm depth for linear toolpath and 54 mm length, 27 mm width, 1 mm depth for trochoidal toolpath.

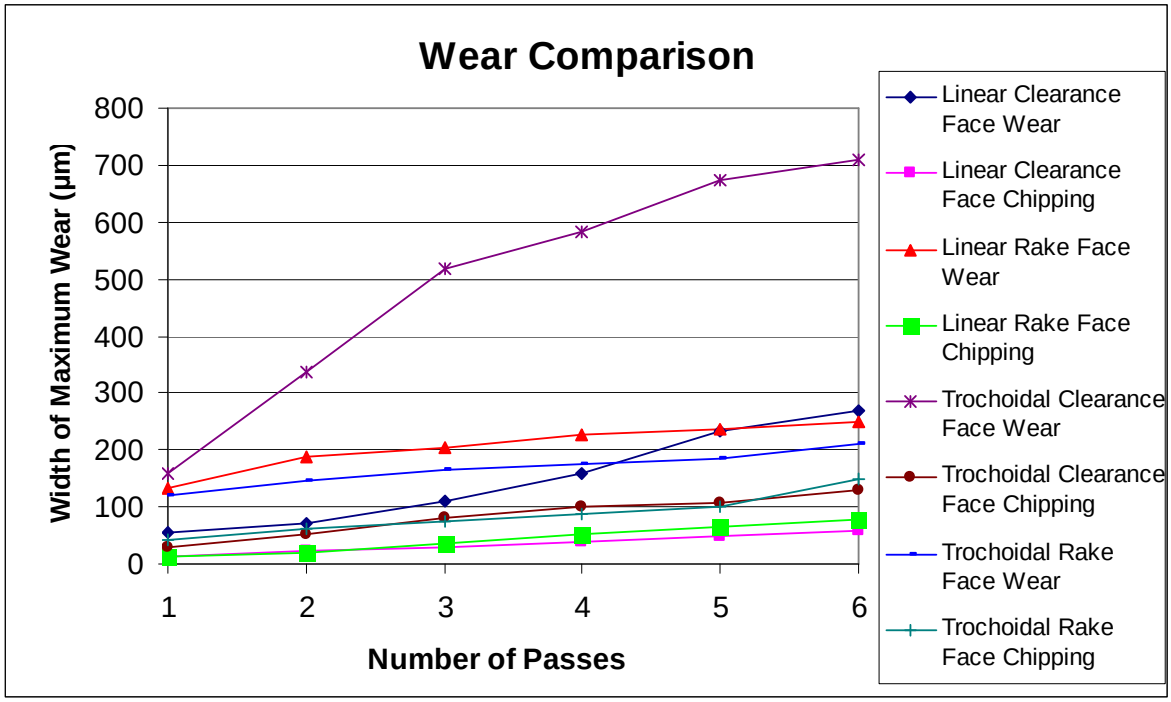

Figure 7.36: Trochoidal and linear toolpaths wear comparison at each pass corresponding to 162 mm length, 9 mm width, 1 mm depth for linear toolpath and 54 mm length, 27 mm width, 1 mm depth for trochoidal toolpath.

7.4.4 Temperature Simulations of the Investigated Toolpaths

Metal machining process is associated with high temperatures due to the fact that the thermal aspects of the metal machining seriously affect the accuracy of the machining process. The high cutting temperatures have serious consequences on both tool and the workpiece such as tool wear, tool life and form and accuracy errors and residual stresses on the workpiece. Therefore determination of the cutting temperatures is very critical in machining in order not to reach the fatal temperature of the cutting tool and coating since then there is a rapid deterioration of the cutting edge, which increases force and temperature of the tool and part.

Radial depth of cut determines the temperatures reached because it settles on how long the teeth stay in cutting and cooling. Since radial depth of cut in trochoidal toolpath is lower rather than linear one the cutting temperatures are also expected to be lower.

The model used in predicting the cutting temperatures needs orthogonal cutting test in order to obtain parameters for the cutter workpiece pair such as shear stress, friction and shear angle. Schematic representation of orthogonal cutting process is shown in Figure 7.37. In orthogonal cutting process, a cutting tool with a straight cutting edge perpendicular to the cutting velocity shears away chip with a width of (b) and depth of cut (h) which is the uncut chip thickness. There is a two dimensional plain strain deformation generating tangential (F_t) and feed forces (F_f) in the direction of velocity and uncut chip thickness respectively.

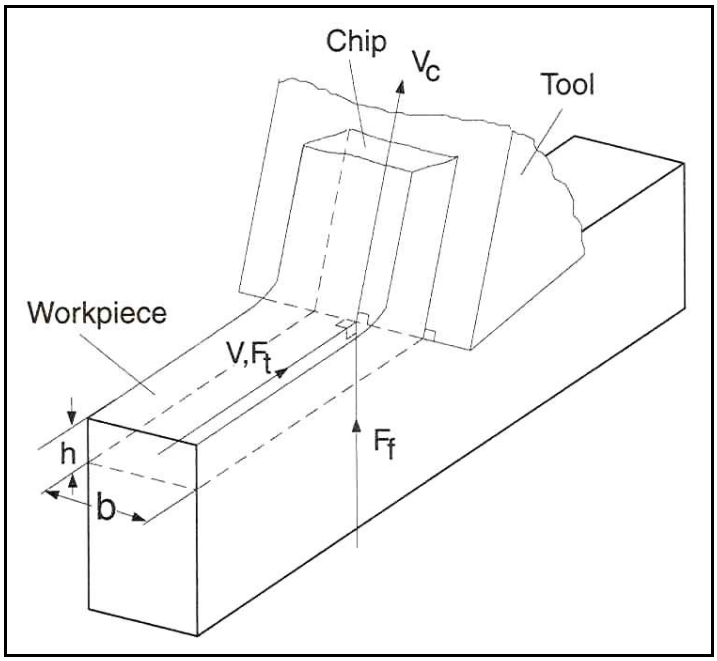

Figure 7.37: Geometry of orthogonal cutting process [2].

The experimental setup for orthogonal cutting test is shown in Figure 7.39. The same data acquisition system used for the milling experiments was used. In order to determine

shear angle, friction angle and shear flow stress; orthogonal cutting tests were carried out in a Mazak Nexus 150 CNC turning center. The material was an AISI H13 steel workpiece with the outer diameter of 40 mm and an inner diameter of 36 mm, a wall thickness of 2 mm. The dynamometer was connected to the turret of the turning center via a special made adapter. The cutter with 25 x 25 mm dimensions was mounted on the dynamometer using another special made adapter. The MTE 9 mm end mill has 12 º rake angle (α_r) and 8 º clearance angle (Cl_p). In order to simulate the same cutting conditions a MTE cutter insert with 8 x 8 mm dimensions was grinded to achieve the same angles as shown in Figure 7.38. The rake and clearance angles were measured with CMM Dia Status 7.5.5 with a probe diameter of 1 mm as 12.5º and 10º respectively.

Figure 7.38: Visualization of the cutter and the insert.

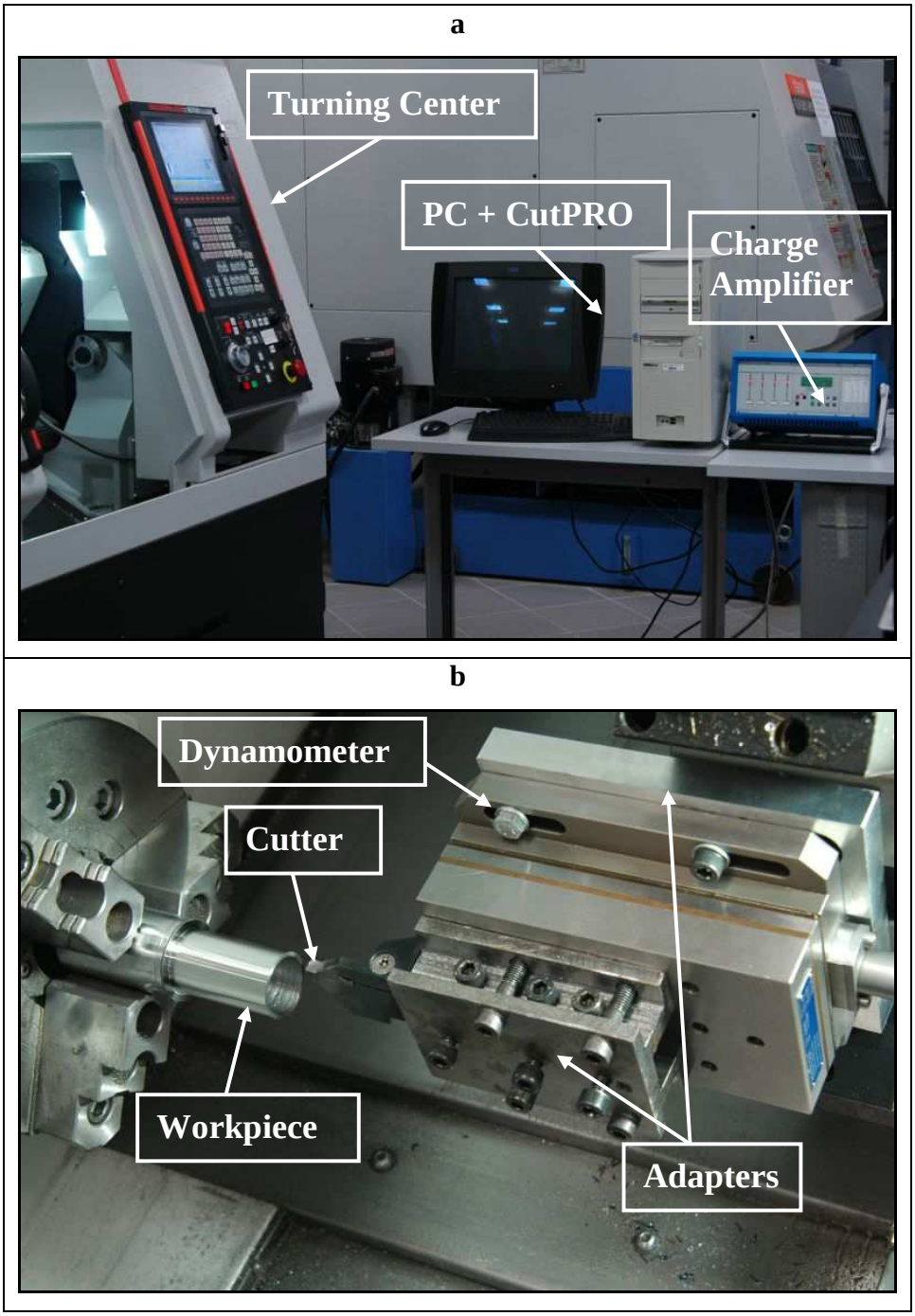

Figure 7.39: Experimental setup for orthogonal cutting process via turning.

The original linear and trochoidal milling tests were carried out 1415 rpm spindle speed and 170 mm/min feedrate corresponding 0.030 mm/rev feed per tooth value and 40 mm/min cutting velocity. The orthogonal cutting tests were also performed at same cutting velocity and between 0.015~0.060 mm uncut chip thickness interval with 0.015 mm increments enclosing the chip thickness value for the milling tests. Due to the shearing mechanism chip thickness changes after cutting. At this moment the chip compression ratio (r_c) is identified as:

$$r_c = \frac{h}{h_c} \tag{7.4}$$

where h is uncut chip thickness and h_c is the cut chip thickness. The cut chip thickness was measured 0.065 mm with Nikon Eclipse LV100D microscope. The shear angle is a function of chip compression ratio and rake angle of the tool (α_r) and the friction angle is a function of the tangential and radial cutting forces and rake angle as follows:

$$\varphi_c = \tan^{-1} \frac{r_c \cos \alpha_r}{1 - r_c \sin \alpha_r} \tag{7.5}$$

$$\beta_a = \alpha_r + \tan^{-1} \frac{F_f}{F_t} \tag{7.6}$$

The shearing stress is:

$$\tau_s = \frac{F_s}{A_s} \tag{7.7}$$

where F_s is the shearing force which can be determined from the resultant cutting force and the rake, shear and friction angles, and A_s is shear plane area as follows:

$$F_s = F\cos(\varphi_c + \beta_a - \alpha_r) \tag{7.8}$$

$$A_s = b\frac{h}{\sin\varphi_c} \tag{7.9}$$

The measured cutting forces with respect to the uncut chip thickness are shown in Figure7.40. Table 7.11 indicates the necessary parameters for the temperature simulation code.

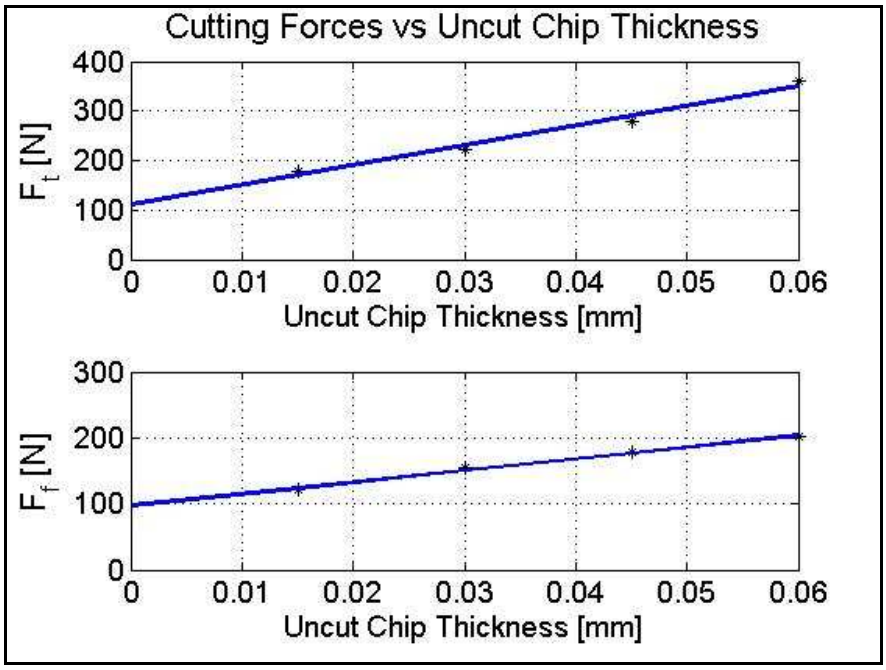

Figure 7.40: Experimental setup for orthogonal cutting process via turning.

Table 7.11: Necessary parameters for temperature simulation

	Linear Milling	**Trochoidal Milling**
Feedrate (mm/tooth)	0.03	
Spindle speed (rpm)	1415	
Entrance angle	0º	
Exit angle	180º	46.22º (max)
Tool diameter (mm)	9	
Rake angle	12 º	
Clearance angle	8 º	
Shear angle	26.53 º	
Friction angle	41.32º	
Shear stress	1134 MPa	
	Workpiece (AISI H13)	**Tool** (MTE 9 mm End Mill)
Density	7.6 kg/dm^3	7.9 kg/dm^3
Specific heat capacity	520 J/(kg.K)	460 J/(kg.K)
Conductivity	26 W/(m.K)	19 W/(m.K)

The engagement conditions always vary for trochoidal milling and the maximum engagement angle is approximately 46º for the investigated toolpath. The milling temperature code can predict the temperatures of the tool and chip only for constant engagement conditions. Therefore the maximum engagement angle 46º is used for the temperature prediction with trochoidal toolpath. Taking into consideration the lower engagement angles, the real cutting temperatures are expected to the lower than the predictions. On the other hand, the temperature code works only for up milling so the temperature predictions for linear toolpath are performed with the engagement domain 0-90º. However the cutting temperatures are expected to be greater than the predictions for linear milling. Figure 7.41 and 7.42 presents the variation of the maximum tool temperature with respect to rotation angle for linear and trochoidal milling respectively. The maximum tool temperature for linear milling is 372 º C and 307 º C for trochoidal milling. In Figures 7.43 and 7.44 the variation of the tool rake face temperature is presented for linear and trochoidal milling. Figures 7.45, 7.46, 7.49 and 7.50 shows the contour and Figures 7.47, 7.48, 7.51 and 7.52 shows the distribution of the tool and chip temperature both for linear and trochoidal milling.

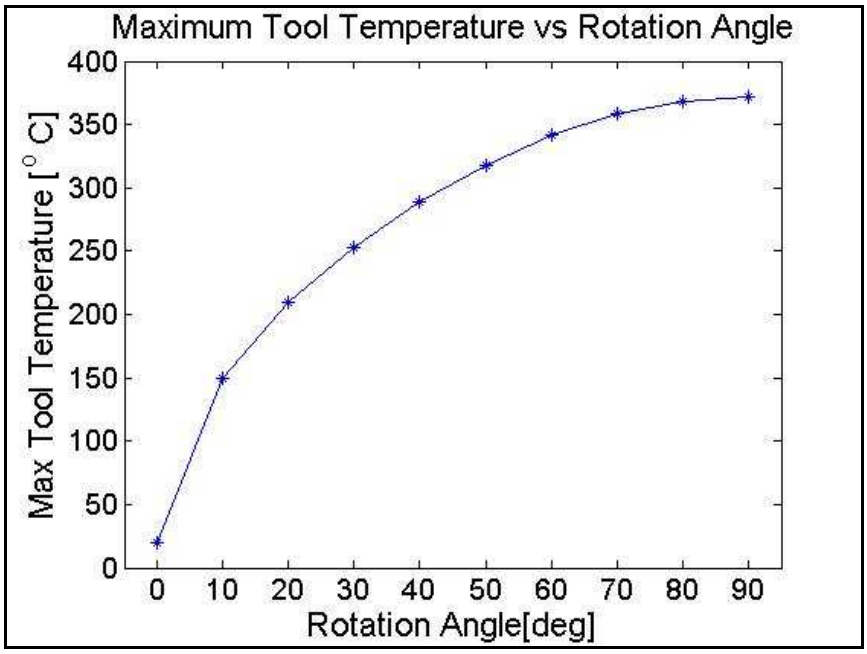

Figure 7.41: Variation of maximum tool temperature with rotation angle for linear milling.

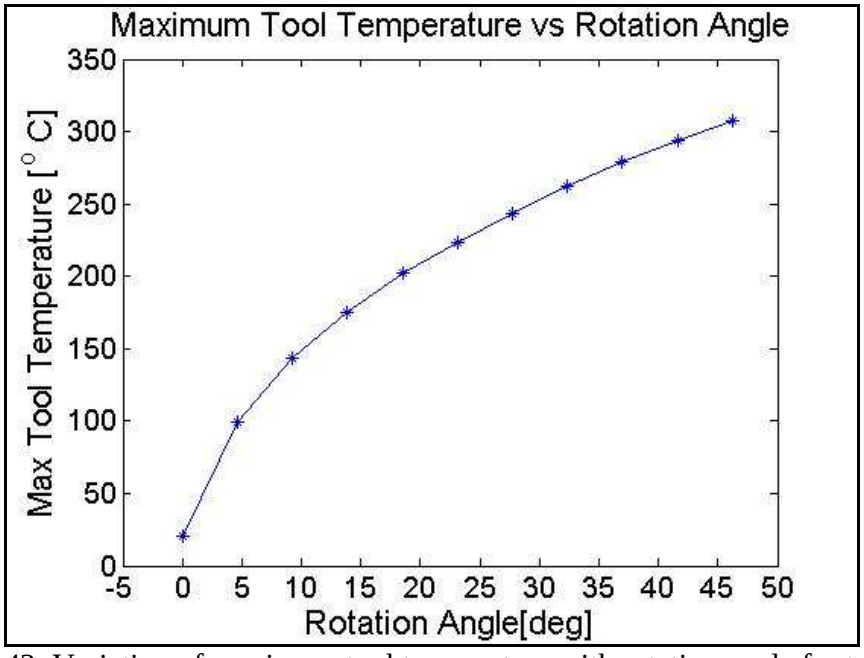

Figure 7.42: Variation of maximum tool temperature with rotation angle for trochoidal milling.

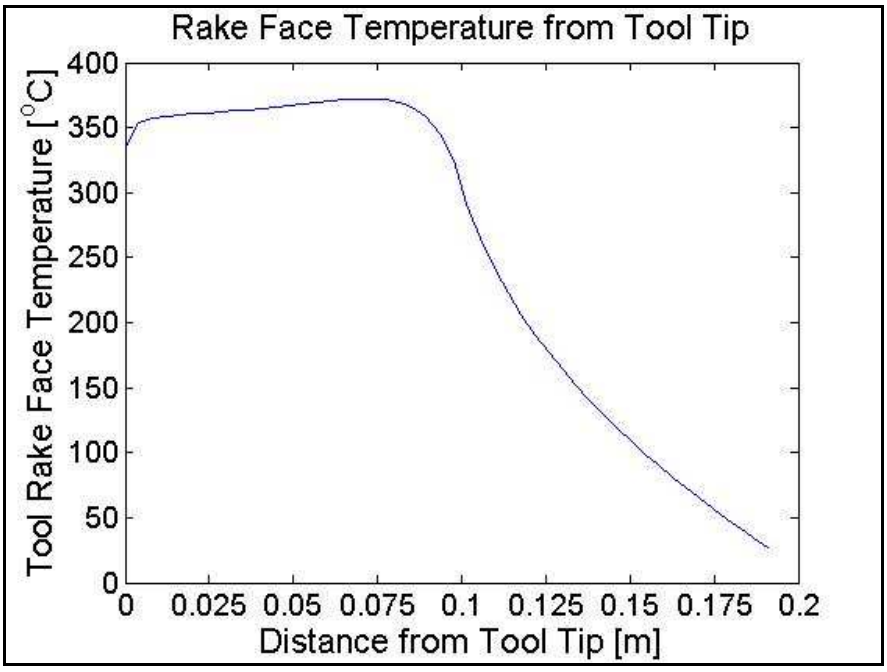

Figure 7.43: Rake face temperature from tool tip for linear milling.

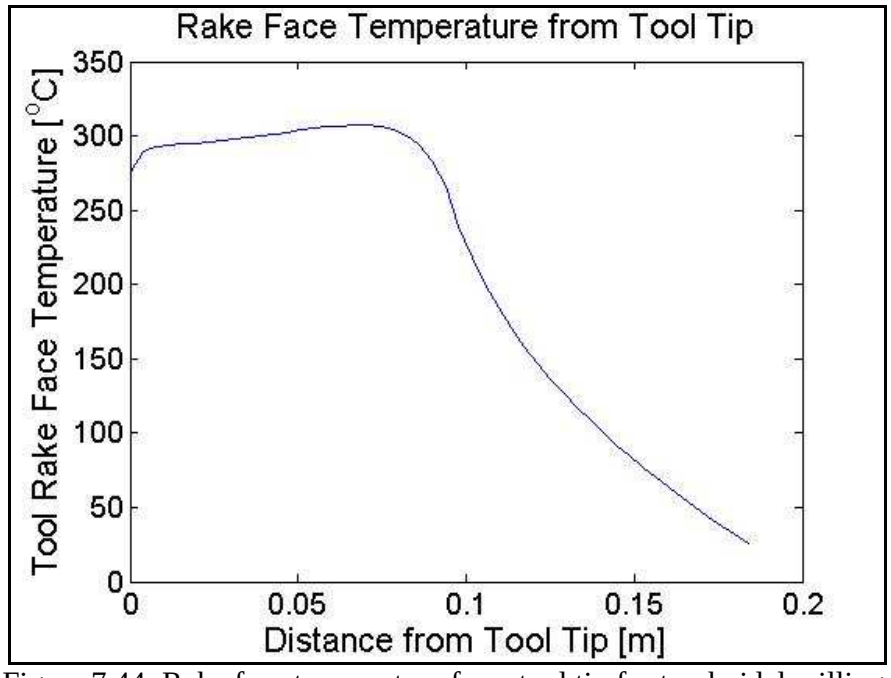

Figure 7.44: Rake face temperature from tool tip for trochoidal milling.

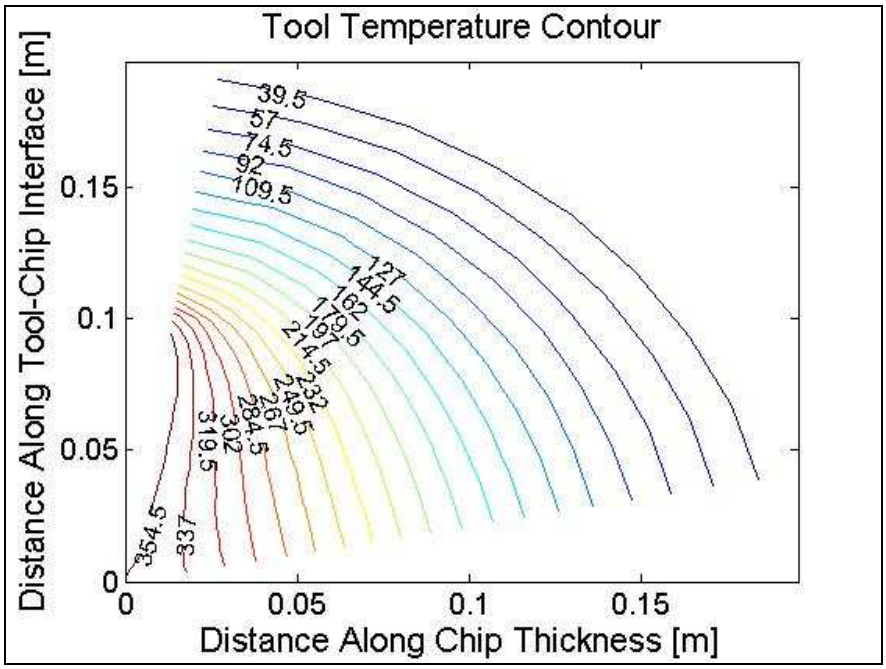

Figure 7.45: Tool temperature contour for linear milling [º C].

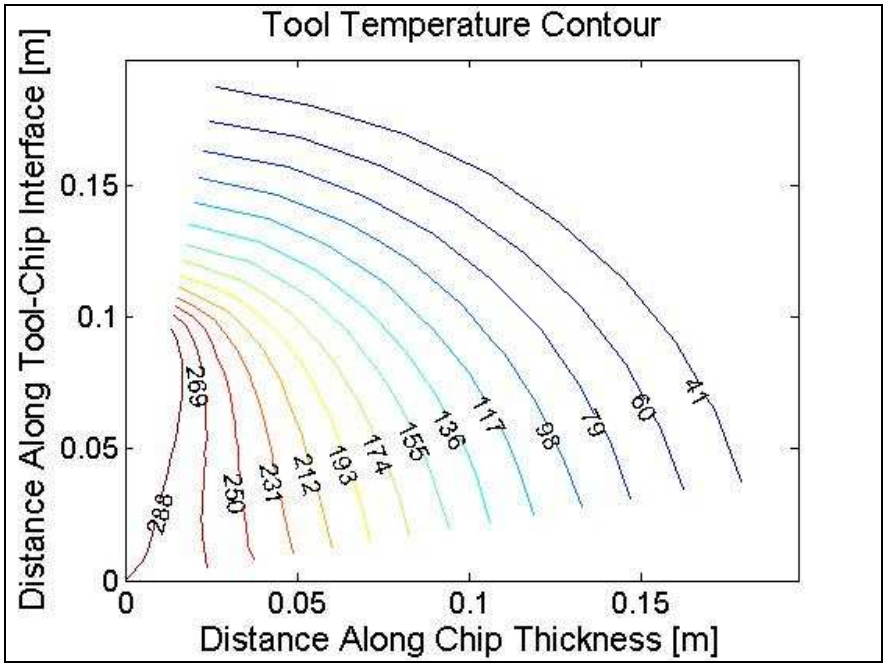

Figure 7.46: Tool temperature contour for trochoidal milling [º C].

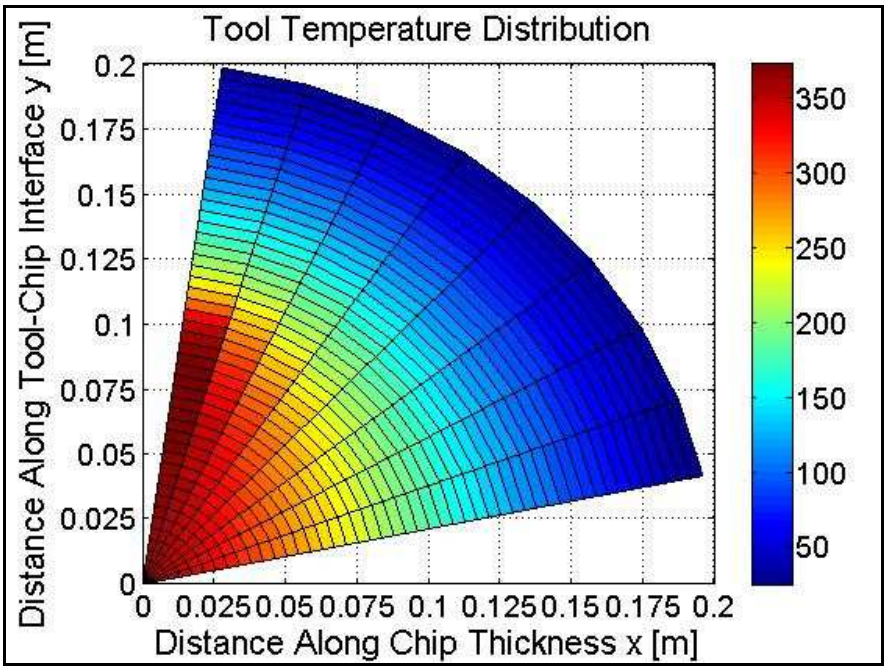

Figure 7.47: Tool temperature distribution for linear milling [º C].

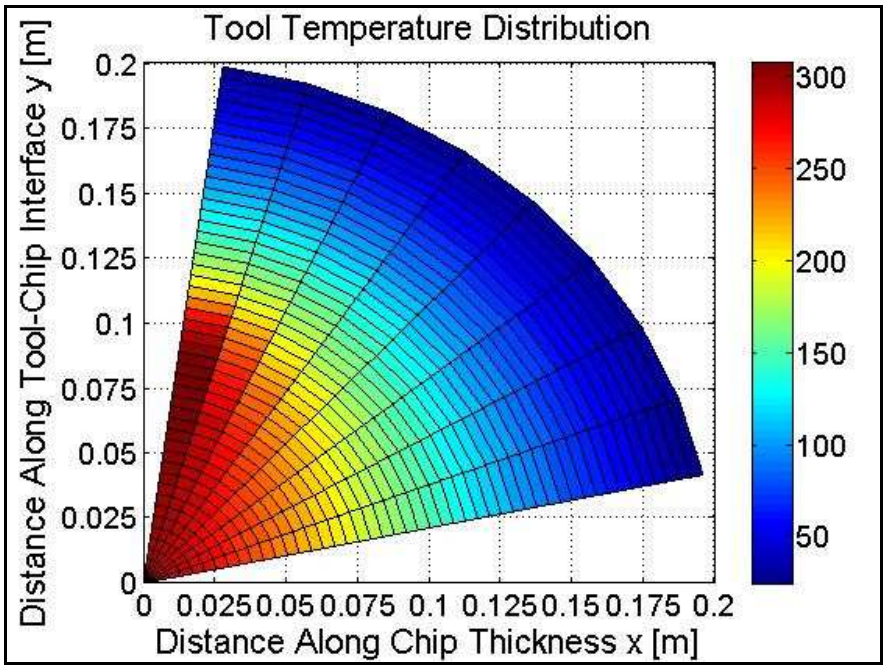

Figure 7.48: Tool temperature distribution for trochoidal milling [º C].

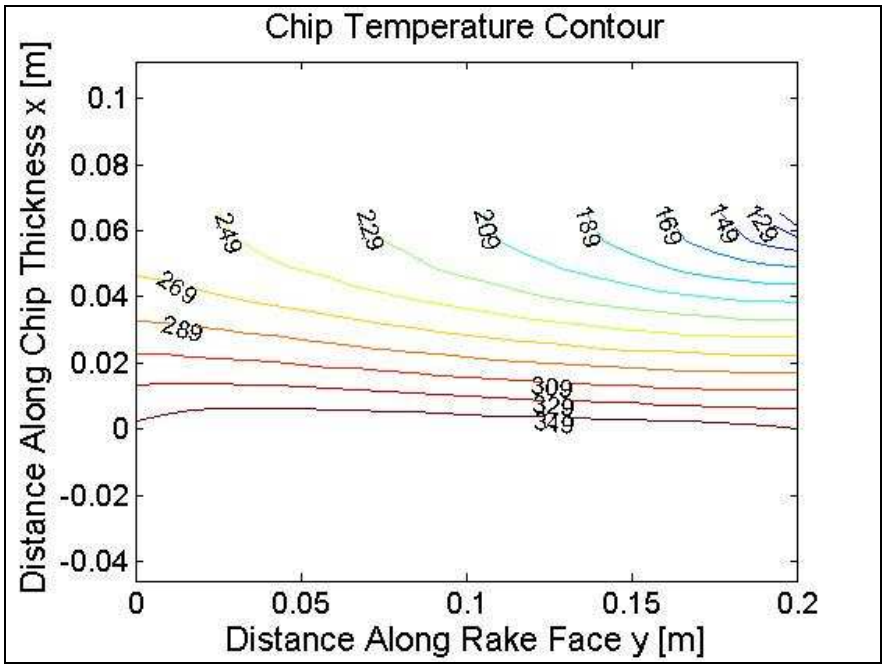

Figure 7.49: Chip temperature contour for linear milling [º C].

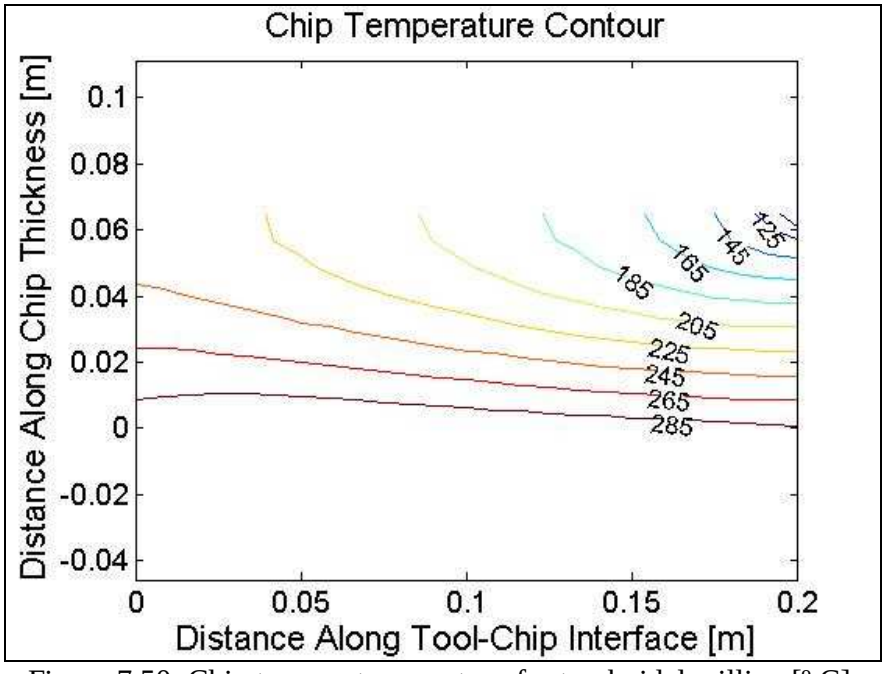

Figure 7.50: Chip temperature contour for trochoidal milling [º C].

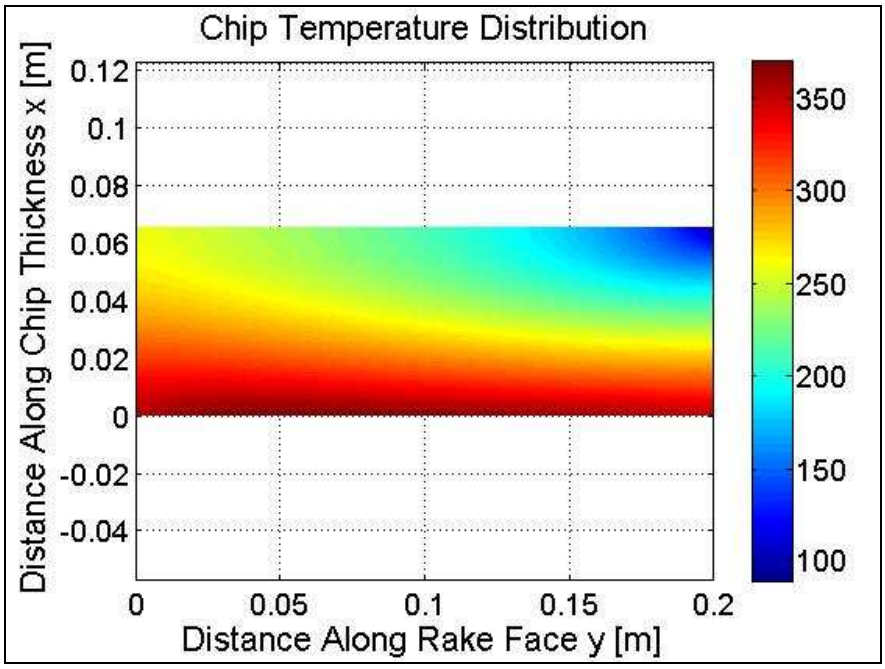

Figure 7.51: Chip temperature distribution for linear milling [° C].

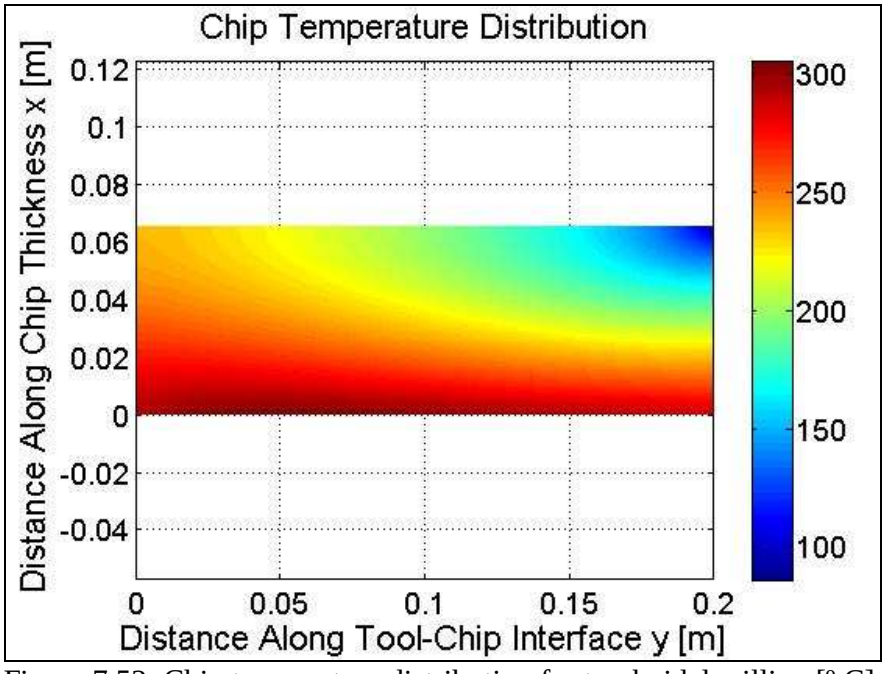

Figure 7.52: Chip temperature distribution for trochoidal milling [° C].

Chapter 8

CONCLUSIONS

Commercial CAM programs use different toolpath strategies in order to increase efficiency and machinebility. Toolpaths such as circular and trochoidal are extremely used to lighten the engagement conditions especially for hard part machining with High Speed Machining (HSM) strategies. Although mechanics of circular toolpath has been investigated [20], there is not any available study for trochoidal milling with the author's best knowledge. The objective of the thesis has been to develop a reliable quantitative and qualitative force prediction algorithm for trochoidal milling process and further optimize the process [38].

The force prediction algorithm consists of engagement and force models. The engagement defining procedure has significant importance in the force prediction algorithms as it supplies the boundary conditions for the integration process of the cutting forces. Two novel engagement models were developed for trochoidal milling in this thesis. The first one is analytical engagement model which defines the engagement angles for simple trochoidal milling operation with filled surface. However, most of the mechanical parts being machined have complex geometries. Thus a second approach, a numerical engagement model capable of defining the engagement for complex surface containing holes or bosses in it, has been developed.

Due to the nature of trochoidal toolpath machining cycle times increase in a considerable amount. Modification of the process is carried on with introducing two different toolpath: Trochoidal toolpath with straight linear motion at the back half of planetary revolution in feed direction and double trochoidal milling mechanism. Force based feedrate scheduling algorithm was applied over double trochoidal toolpath in order to further optimize

the process and 64.4 % reduction in cycle time compared with original trochoidal milling operation was achieved.

In all the phases of the thesis validations of the simulations were performed with experimental studies. The proposed toolpaths were generated with Unigraphics software and applied using Mazak 3 axis vertical machining center. The generated cutting forces were collected and digitized via Kistler dynamometer and charge amplifier and National Instruments I/O box and DAQ card. The simulated cutting forces showed good correspondence with the experiments in all the proposed algorithms.

The last chapter of this thesis includes comparison of trochoidal and linear toolpath upon usage characteristics such as wear characteristics comparison, cutting forces comparison and surface roughness comparison. The experimental study performed with hard materials figures out that trochoidal toolpath is not an optimized algorithm within the investigated cutting conditions because not only cycle time is 20 times of the one for linear toolpath but also the cutter edge wears out more with trochoidal toolpath lowering the lifetime of the cutter. Moreover, the surface roughness of the machined workpiece is worse for the trochoidal toolpath.

BIBLIOGRAPHY

[1] Sandvik Coromat Article, A Global Productivity Partner in Die and Mold Making, available at http://www.coromant.sandvik.com/

[2] Y. Altintas, Manufacturing Automation: Metal Cutting Mechanics, Machine Tool Vibrations, and CNC Design, Cambridge University Press, (2000).

[3] M.E. Martelotti, An Analysis of the Milling Process, Transactions of the ASME, Vol. 63 (1941), pp 677-700.

[4] M.E. Martelotti, An Analysis of the Milling Process, Part II – Down Milling, Transactions of the ASME, Vol. 67 (1945), pp 233-251.

[5] F. Koenigsberger and A.J.P. Sabberwal, An Investigation into the Cutting Force Pulsations During Milling Operations, International Journal of Machine Tool Design and Research, Vol. 1 (1961), pp 15-33.

[6] J. Tlusty and P. MacNeil, Dynamics of Cutting Forces in End Milling, Annals of the CIRP, Vol. 24 (1975), pp 21-25.

[7] P.E. Gygax, Dynamics of Single Tooth Milling, Annals of CIRP, Vol. 28, (1979), pp 65-70.

[8] P.E. Gygax, Experimental Full Cut Milling Dynamics, Annals of CIRP, Vol. 29 (1980), pp 61-66.

[9] W.A. Kline, R.E. DeVor, and I.A. Shareef, The prediction of Surface Accuracy in End Milling, ASME Transactions: Journal of Engineering for Industry, Vol. 104 (1982) , pp 272-278.

[10]W.A. Kline, The Prediction of Cutting Forces and Surface Accuracy For The End Milling Process, Ph. D. Thesis, University of Illinois at Urbana-Champaign (1982)

[11] W.A. Kline, R.E. DeVor, and I.A. Lindberg, J.R., The prediction of Cutting Forces in End Milling with Application to Cornering Cut, International Journal of Machine Tools Design and Research, Vol. 22 (1982), pp 7-22.

[12] J.W. Sutherland and R.E. DeVor, An Improved Method for Cutting Force and Surface Error Prediction in Flexible End Milling Systems, ASME Journal of Engineering for Industry, Vol. 108 (1986), pp 269-279

[13] D. Montgomery and Y. Altintas, Mechanism of Cutting Force and Surface Generation in Dynamic Milling, ASME Journal of Engineering for Industry, Vol. 13 (1991), pp l60-168.

[14] E.J.A. Armarego and N.P. Deshpande, Force Prediction Models and CAD/CAM Software for Helical Tooth Milling Processes, I, Basic approach and Cutting Analyses, International Journal of Production Research Vol. 31 (1993), pp 1991-2009.

[15] E.J.A. Armarego and R.C. Whitfield, Computerized End-Milling Force Predictions with Cutting Models Allowing Eccentricity and Cutter Deflections, Annals of the CIRP, Vol. 40 (1991), pp 25-29.

[16] E. Budak, Y. Altintas and E.J.A Armarego, Prediction of Milling Force Coefficients From Orthogonal Cutting Data, Transactions of the ASME Journal of Manufacturing Science and Engineering, Vol. 118 (1996), pp 216-224.

[17] E. M. Lim.C. H. Meng, Integrated planning for precision machining of complex surfaces. Part 1: Cutting path and feedrate optimization, International Journal of Machine Tools Manufacturing, Vol. 37 (1997), pp 61-75.

[18] H. Erdim, Improving Productivity in Free-form Surface Machining, MSc Thesis, Koc University (2005)

[19] D. Mickelson, Hard milling & high speed machining: tools of change, Hanser Gardner Publications (2005)

[20] N. Kardes, Y. Altintas, Prediction of cutting forces in circular milling, 3rd International Conference and Exhibition on Design and Production of Dies and Molds (2004), pp 1-5.

[21] G. Elber, E. Cohen, S. Drake, MATHSM: medial axis transform toward high speed machining of pockets, Computer Aided Design, Vol. 37 (2005), pp 241-250.

[22] Available from http://www.mmsonline.com/

[23] Y. Tang, Optimization strategy in end milling process for high speed machining of hardened die/mold steel**,** Journal of University of Science and Technology Beijing, Vol. 13 (2006) Num. 3, pp 240-243.

[24] Q. Zhang, R. B. Greenway, Development and implementation of a NURBS curve motion interpolator, Robotics and Computer-Integrated Manufacturing, Vol. 14 (1997), pp 27-36.

[25] M.Y. Cheng, M.C. Tsai, J.C. Kuo, Real-time NURBS command generators for CNC servo controller, International Journal of Machine Tools and Manufacture, Vol. 42 (2002), pp 801-813.

[26] M.C. Tsai, C.W. Cheng, M.Y. Cheng, A real-time NURBS surface interpolator for precision three-axis CNC machining, International Journal of Machine Tools and Manufacture, Vol. 43 (2003), pp. 1217-1227.

[27] X. Liu, F. Ahmad, K. Yamazaki, M. Mori., Adaptive interpolation scheme for NURBS curves with the integration of machining dynamics, International Journal of Machine Tools and Manufacture, Vol. 45 (2005), pp. 433-444.

[28] K.K. Wang, Solid Modeling for Optimizing Metal Removal of Three-Dimensional NC End Milling, Journal of Manufacturing Systems, Vol. 7 (1988), pp 57–65.

[29] R.W.L. Ip, H.C.W. Lau, F.T.S. Chan, An Economical Sculptured Surface Machining Approach Using Fuzzy Models and Ball-nosed Cutters, Journal of Materials Processing Technology, Vol. 138 (2003), pp 579–585.

[30] Z.Z. Li, M. Zheng, L. Zheng, Z.J. Wu, D.C. Liu, A solid model-based milling process simulation and optimization system integrated with CAD/CAM, Journal of Materials Processing Technology, Vol. 138 (2003), pp 513–517.

[31] T.J. Ko, H.S. Kim, S.H. Park, Machinebility in NURBS Interpolator Considering Constant Material Removal Rate, International Journal of Machine Tools & Manufacture, Vol. 45 (2005), pp 665-671.

[32] B.U. Guzel, I. Lazoglu, Increasing Productivity in Sculpture Surface Machining via Off-line Piecewise Variable Feedrate Scheduling Based On the Force System Model, International Journal of Machine Tools Manufacture, Vol. 44 (2004), pp 21–28.

[33] H. Erdim, I. Lazoglu, B. Ozturk, Feedrate Scheduling Strategies For Free-form Surfaces, International Journal of Machine Tools Manufacture, Vol. 46 (2006), pp 747-757.

[34] B. Guzel, Sculpture Surface Machining, MSc Thesis, Koc University (2003)

[35] S. Hogmark, M. Olsson, Wear mechanisms of HSS cutting tools

[36] http://www.nikoncoolscope.net/template.php?cat=5&grp=27&productNr=LV100D

[37] Mitutoyo SJ-301 Surface Roughness Tester Operating Manual series No: 178

[38] M. Otkur, I. Lazoglu, Trochoidal milling, International Journal of Machine Tools & Manufacture, In press corrected proof, (2006).

VITA

Murat Ötkür completed Kadıköy Anatolian High School, İstanbul, in 2000. He received his B.Sc. Degree in Mechanical Engineering from İstanbul Technical University (İTU), İstanbul, in 2004. Since 2004, he is in the M.Sc program in Mechanical Engineering at Koc University as a teaching/research assistant. For the completion of the program he has taken part in a mechanical engineering thesis study with the title ‘Trochoidal Milling’. Upon completing the M.Sc program, he will perform doctoral study in Manufacturing Systems and Robotics program at EPFL.